SYNTHESIS AND SPINTRONIC APPLICATIONS OF CHIRAL PEROVSKITE NANOMATERIALS

REN HUI

PhD

The Hong Kong Polytechnic University

2025

The Hong Kong Polytechnic University

Department of Applied Physics

Synthesis and Spintronic Applications of Chiral Perovskite Nanomaterials

Ren Hui

A thesis submitted in partial fulfillment of the requirements for the degree of Doctor of Philosophy

August 2024

CERTIFICATE OF ORIGINALITY

I hereby declare that this thesis is my own work and that, to the best of my knowledge and belief, it reproduces no material previously published or written, nor material that has been accepted for the award of any other degree or diploma, except where due acknowledgement has been made in the text.

_____(Signed)

Ren Hui (Name of student)

Abstract

Organic-inorganic perovskite materials have garnered significant research interest owing to their unique properties, such as long diffusion length, tunable bandgaps, and high absorption coefficients, which are advantageous in optoelectronics and photovoltaics. Concomitantly, the synthesis of various perovskite nanomaterials (i.e. <100 nm) including nanocrystals, nanoplates, nanosheets, nanowires, etc., has expanded the compositional diversity of the perovskites. The quantum confinement effect in these perovskite nanomaterials allows for tunable optical and electrical properties, enhancing their potential in optoelectronics applications.

Recently, the introduction of chirality into perovskite structures, combined with their diverse optoelectronic properties, has extended their potential applications to chiral optoelectronics, ferroelectricity, spintronics, etc. Additionally, the finding of the spin-orbit coupling (SOC), Rashba splitting and long spin lifetimes in perovskites has opened new avenues for spintronic applications, which are crucial for advancing information technology and quantum computing constructs.

Achieving long-lived spin orientation at room temperature without a magnetic field is highly desirable for spintronics applications. The chirality-induced spin selectivity (CISS) effect offers a promising approach for efficient spin generation and manipulation. This dissertation first investigates the spin generation, dynamics, and transport properties of newly developed colloidal chiral $CsPbBr_3$ nanocrystal platelets (NPLs) with varying well thicknesses. These chiral NPLs exhibit an extended spin depolarization lifetime of approximately 210 ps, around one order of magnitude longer than their nanocrystal counterparts. Notably, they also demonstrate high circularly polarized emission (5.0%), spin current polarization up to approximately 43%, and a spin diffusion length reaching 33 nm. Theoretical calculations indicate that the introduction of chiral ligands induces asymmetry in $CsPbBr_3$ NPLs, creating an additional barrier to spin flipping due to the distinct momentum troughs associated with different spin states. These findings provide valuable insights into the underlying mechanisms and highlight a novel class of materials with significant potential for future spintronic applications.

Moreover, lead-free perovskite materials are promising alternatives to conventional lead-based perovskites due to their reduced toxicity and increased environmental

stability. Despite the current focus on chiral perovskite thin films and single crystals, research on the chiral properties of lead-free double perovskite nanocrystals is limited. We successfully synthesized cubic phase $Cs_2AgIn_xBi_{1-x}Cl_6$ (x = 0, 0.3, 0.6, and 0.9) nanocrystals (NCs) using the hot injection method. The intrinsic chirality of $Cs_2AgIn_{0.9}Bi_{0.1}Cl_6$ NCs was observed while we studied the chiral signals induced by chiral molecules in perovskite nanocrystals. HADDF-STEM imaging and simulation confirmed chiral defects, specifically screw dislocations in $Cs_2AgIn_{0.9}Bi_{0.1}Cl_6$ NCs. Under the measurement of the circularly polarized transient absorption spectrum, both untreated and chiral ligand-treated $Cs_2AgI_{0.9}Bi_{0.1}Cl_6$ NCs exhibited remarkably long spin depolarization lifetime, spanning 10 ns. Additionally, we also investigated the degree of spin-polarized current under dark conditions in R-/S-MBA-treated $Cs_2AgIn_{0.9}Bi_{0.1}Cl_6$ NCs devices, induced by the chiral-induced spin selectivity (CISS) effect. Most importantly, we provide further proof of the CISS effect in spin photovoltaic devices with the measurement of the spin-polarized photocurrent at 0V under different directions of the magnet field. These findings enhance our understanding of the chiral properties and mechanisms of lead-free double perovskite nanocrystals and have significant implications for the design and development of spintronic applications based on these chiral perovskite nanomaterials.

List of publications

(1) Qi Wei, **Hui Ren (co-first author),** Jinjie Liu, Qi Liu, Chenhao Wang, Ting Wai Lau, Luwei Zhou, Tieyuan Bian, Yifan Zhou, Pengzhi Wang, Qiong Lei, Omar F. Mohammed, Mingjie Li, and Jun Yin. Long-lived hot carriers in two-dimentional perovskites: The role of alternating cations in interlayer space. **ACS Energy Letters** 2023 8 (10), 4315-4322

(2) **Hui Ren**, Qi Wei, Qi Liu, Luwei Zhou, Jun Yin, Taoyuan Du and Mingjie Li. Long lived spin polarization in Lead-free double perovskite nanocrystals with screw-dislocation for spintronics devices. **Nature materials** (submitted)

(3) Qi Wei, Jonas S, Peter, **Hui Ren (co-first author)**, Weizhen Wang, Luwei Zhou, Qi Liu, Stefan Ostermann, Jun Yin, Songhua Cai, Susanne F. Yelin and Mingjie Li. Circularly polarizaed superfluorescence from chiral perovskite quantum well superlattice. **Nature** (under review)

(4) Qi Wei, Bing Tang, **Hui Ren (co-first author),** Jun Yin, and Mingjie Li. Long-lived exciton spins in chiral colloidal perovskite quantum wells at room temperature. **Advanced Materials** (submitted)

(5) Qi Liu, Qi Wei, **Hui Ren,** Luwei Zhou, Pengzhi Wang, Chenhao Wang, Jun Yin and Mingjie Li. Circular polarization-resolved ultraviolet photonic artificial synapse based on chiral perovskite. **Nature Communications** 2023 14, 7179

(6) Ze Wang, Xiaodong Liu, **Hui Ren,** Li Liu, Xinyu Tang, Xianghua Yao, Zhenhuang Su, Xingyu Gao, Qi Wei, Haijiao Xie, Yonghao Zheng, and Mingjie Li. Insight into the enhanced charge transport in quasi-2d perovskite via fluorination of ammonium cations for photovoltaic applications. **ACS Applied Materials & Interfaces** 2022 14 (6), 7917-7925

(7) Chenhao Wang, Jianhui Fu, Qi Wei, **Hui Ren,** Qi Liu, Luwei Zhou, Pengzhi Wang, and Mingjie Li. Electric-field-enhanced electroluminescence color tuning of colloidal type-II tetrapods. **Nano Letters** 2023 23 (12), 5705-5712

(8) Lyuchao Zhuang, Qi Wei, Chuanzhao Li, **Hui Ren,** Yanyong Li, Fangyi Shi, Lingling Zhai, Kai Leng, Mingjie Li, and Shu Ping Lau. Efficient light-emitting Diodes via hydrogen bonding induced phase modulation in quasi-2D perovskites. **Advance Optical Materials** 2022 10 2201180.

(9) Yifan Chen, Jun Yin, Qi Wei, Chenhao Wang, Xiaoting Wang, **Hui Ren,** Siu Fung Yu, Osman M. Bakr, Omar F. Mohammed and Mingjie Li. Multiple excton generation in tin-lead halide perovskite nanocrystals for photocurrent quantum efficiency enhancement. **Nature Photonics** 2022 16, 485-490.

Acknowledgement

Completing this 3-years PhD thesis has been a challenging yet immensely rewarding journey, First and foremost, I extend my heartfelt gratitude to my supervisor, Dr. Li Mingjie, for his unwavering support, guidance, and mentorship throughout my PhD research. His abundant expertise, constructive feedback, and continuous encouragement have been invaluable in my growth as a researcher.

I am also very thankful to my group member, Mr. Liu Qi, Mr. Zhou Luwei, Dr. Wang Pengzhi, Dr. Wang Chenhao, Dr Zhang Xiang, Dr. Kang Chengbing, Dr Zhao Leyi, and Dr. Peng Jiangbo for their insightful comments, useful suggestions, and rich expertise that have enriched my research work. Their diverse perspectives about my research have broadened my understanding and enhanced the quality of my thesis. Additionally, some colleagues from other groups, Dr. Zhuang Lyuchao, Mr. Liu Duanzijing, and Dr. Zhen Xiaodong have also offered me abundant support in some experimental measurements.

I am grateful to the department of Applied Physics staff, for providing a conformable academic environment and abundant experimental resources essential for completing my PhD thesis.

Special thanks to my fellow researcher, Dr. Wei Qi, who provided me with countless help during my three years of PhD study. He helped me test the paper data repeatedly and could provide me with ideas when I encountered problems in my research.

I would like to express my deepest appreciation to my family and friends for their unwavering love, continuous understanding, and strong encouragement throughout my academic research.

I am grateful to my friends for their continuous support, encouragement, and understanding. Their presence has provided much-needed respite and joy during the demanding phases of this research journey.

Lastly, I acknowledge my boyfriend, Luke, for his meticulous care over the years. Scientific research life is undoubtedly full of challenges, so his optimism and positivity also gave me the courage to overcome failure in my research.

Table of Contents

List of Figures

Chapter 1 Introduction

1.1 Background

Since the discovery of giant magnetoresistance, the field of spintronics has seen significant advancements, particularly within nanotechnology. Spintronics aims to leverage spin manipulation and spin-polarized electronic transport in materials, contributing to its rapid development. Perovskite nanomaterials have experienced unprecedented growth due to their exceptional photoelectrical properties, such as composition diversity, adjustability, solution processability, and long exciton diffusion length. Recently, spintronics in perovskites have emerged, utilizing the spin degree of freedom. Previous research on the intrinsic spin-related properties of perovskite materials, including the Stark effect, spin-orbit coupling, Rashba effect, triplet formation, and polarized-light effect, highlights their limitless potential for spintronics applications. Innovative spin-related optoelectronic properties in perovskite devices have achieved both theoretical and experimental progress, offering new strategies for spintronic materials. These advancements enable the development of novel devices, such as spin valve devices, spin photovoltaics (solar cells), spin light-emitting diodes/lasers, and circular polarization light detectors. However, several challenges remain, including a deeper understanding of spin-related effects between photons and electrons, the stability of perovskites under various conditions, and the degree of spin polarization in spintronics. Addressing these challenges will further enhance the optoelectronic applications of spintronics in perovskite materials.

1.2 Objective of Research

Organic-inorganic hybrid perovskite materials have made significant strides in traditional optoelectronic devices like solar cells, light-emitting diodes, and photodetectors due to their unique characteristics. The development of spintronics is a recent application of perovskite materials, leveraging properties such as strong spin-orbit coupling, Rashba splitting, magneto-optical effect, and Stark effect. The chiral-induced spin selectivity effect (CISS) can produce spin-polarized electrons without magnetic materials. In low-dimensional systems, strong confinement leads to atomic-like energy levels with large interlevel spacings, weakly coupling to phonons, thereby suppressing spin relaxation by phonon scattering and prolonging spin lifetime.

However, experimental studies have reported short spin relaxation lifetimes in quantum-confined perovskites, typically ranging from femtoseconds to picoseconds at room temperature, much shorter than conventional II-V GaAs semiconductors. Achieving long-lived spin orientation at room temperature without a magnetic field is highly desirable for spintronics applications. Chirality-induced spin selectivity offers a promising approach for efficient spin generation and manipulation. Therefore, improving spin lifetime and polarization in perovskite nanomaterials is a current priority.

Our first study aims to investigate the spin generation, dynamics, and transport properties of newly developed colloidal chiral $CsPbBr_3$ perovskite nanoplates (NPLs) with varying well thicknesses. Circularly polarized transient absorption experiments were conducted on all $CsPbBr_3$ NPLs to understand the spin-flip mechanism and quantify the exciton spin relaxation lifetime. Theoretical calculations were performed to examine the influence of chiral ligands on symmetry breaking in $CsPbBr_3$ nanocrystal platelets (NPLs). Chiral ligands alter the spin-orbit coupling environment, induce symmetry breaking in NPLs, and create an additional barrier to spin flipping due to spin states in different momentum valleys. To explore the potential of spintronics applications in $CsPbBr_3$ NPLs, we measured the CISS effect on the spin current under dark conditions, providing valuable insights into the underlying spin-filtering transport mechanism and the potential of chiral perovskite nanomaterials in spintronic applications.

Additionally, lead-free perovskite materials are promising alternatives to conventional lead-based perovskites due to their reduced toxicity and increased environmental stability. Lead-free perovskites typically use elements such as tin, bismuth, or antimony as the A-site cation in the perovskite crystal structure. These materials have demonstrated promising optoelectronic properties, including high photoluminescence quantum yields, high carrier mobility, and excellent stability under ambient conditions. However, their performance is typically lower than lead-based perovskites, and challenges remain in synthesis and stability. Recent research has focused on addressing these challenges and improving the performance of lead-free perovskites through approaches such as modifying the crystal structure with dopants or defects and using hybrid perovskites to enhance stability and performance. Despite the focus on chiral perovskite thin films and single crystals, research on the chiral properties of lead-free

double perovskite nanocrystals is scarce, prompting us to direct our research towards this area.

The first challenge is synthesizing cubic phase $Cs_2AgIn_xBi_{1-x}Cl_6$ (x = 0, 0.3, 0.6, and 0.9) nanocrystals (NCs) via hot injection at high temperatures. The morphology and crystal structure of $Cs_2AgIn_xBi_{1-x}Cl_6$ NCs are confirmed through various characterizations to ensure successful synthesis. The next challenge is achieving successful chiral ligand exchange in $Cs_2AgIn_{0.9}Bi_{0.1}Cl_6$ NCs using post-treatment with chiral R-/S-MBA molecules. We then characterize the chirality behaviors in R-/S-MBA treated $Cs_2AgIn_{0.9}Bi_{0.}1Cl_6$ NCs and explore the spintronics dynamics and CISS effect in these chiral ligand-treated NCs. Circularly polarized transient absorption measurements were conducted to study exciton spin relaxation in $Cs_2AgIn_xBi_{1-x}Cl_6$ NCs. Additionally, the CISS effect was identified in devices by measuring spin-polarized current and photocurrent in $Cs_2AgIn_xBi_{1-x}Cl_6$ NCs and chiral ligand-treated $Cs_2AgIn_xBi_{1-x}Cl_6$ NCs. These findings aim to enhance the understanding of chiral properties and mechanisms in lead-free double perovskite nanocrystals, with important implications for designing and developing optoelectronic devices based on these materials.

1.3 Outline of Research

The dissertation proposes two strategies for the studies of spintronics in perovskite nanomaterial. First, we demonstrate the synthesis of the $CsPbBr_3$ NPLs and $Cs_2AgIn_xBi_{1-x}Cl_6$ (x = 0, 3, 6 and 9) NCs. For the absence of long-lived spin polarization at room temperature, we proposed $CsPbBr_3$ NPLs with different layers to investigate the spin dynamics in it. Additionally, the stability of the lead-based perovskite nanomaterials was also settled by the $Cs_2AgIn_xBi_{1-x}Cl_6$ (x = 0, 0.3, 0.6, and 0.9) lead-free double perovskite nanocrystals. The main contents of our thesis are organized as below:

Chapter 1 exhibits the background, origin of our research and the summary of the whole dissertation.

Chapter 2 presents a short introduction to our research backgrounding in the chiral perovskite nanomaterials, and potential spintronics applications in these chiral perovskite nanomaterials.

Chapter 3 summarizes the chemical material used in the synthesis process, the method and the main characteristics of chiral $CsPbBr_3$ NPLs and $Cs_2AgIn_xBi_{1-x}Cl_6$ (x = 0, 0.3, 0.6, and 0.9) NCs.

Chapter 4 proposes the slow spin relaxation dynamics in the n = 2-5 chiral $CsPbBr_3$ monolayer (ML) using circular polarized transient absorption spectroscopy. The layered $CsPbBr_3$ NPLs show an increasing spin relaxation lifetime with increasing NPLs layers, which is a result of the Rashba splitting and phonon scattering effect in these quantum-confined nanostructures. In the $CsPbBr_3$ NPLs treated with chiral organic molecule R-α-methylbenzylamine (R-MBA), we achieved a degree of polarization of P_{CPL} = 5.0%, the discovery of spin depolarization lifetimes up to hundreds of picoseconds and spin diffusion length ~ 33 nm has led to promising applications of chiral perovskite nanostructures in spintronic devices. We used chiral-induced spin selectivity (CISS) to produce spin-polarized carriers with spin polarization value P ~ 43% at room temperature without magnetic fields or ferromagnetic contact.

Chapter 5 introduces the successful synthesis of cubic phase $Cs_2AgIn_xBi_{1-x}Cl_6$ (x = 0, 0.3, 0.6, and 0.9) NCs with regular morphology and uniform size. Then, we discovered the intrinsic chirality of $Cs_2AgIn_{0.9}Bi_{0.1}Cl_6$ NCs while studying the chiral signals induced by chiral molecules. Most significantly, we confirmed that the intrinsic chirality of nanocrystals arises from chiral defects, more specifically, screw dislocations, with HADDF-STEM imaging. In the measurements of the circularly polarized transient absorption of the $Cs_2AgI_{0.9}Bi_{0.1}Cl_6$ NCs and the R/SMBA-$Cs_2AgI_{0.9}Bi_{0.1}Cl_6$ NCs, both show a remarkably long spin depolarization lifetime, spanning 10 ns. Additionally, we estimated the degree of spin-polarized current of +50% for RMBA-treated $Cs_2AgIn_{0.9}Bi_{0.1}Cl_6$ NCs CISS device and −47% for SMBA-treated $Cs_2AgIn_{0.9}Bi_{0.1}Cl_6$ NCs CISS device, respectively. Most importantly, we have further proof of the CISS effect in spin photovoltaic devices with $Cs_2AgIn_{0.9}Bi_{0.1}Cl_6$ NCs and SMBA-/RMBA-treated $Cs_2AgIn_{0.9}Bi_{0.1}Cl_6$ NCs devices.

Chapter 6 is a summary of the whole thesis and an outlook of the following research.

Chapter 2 Overview of Literature Review

2.1 Developments of Perovskite Materials

Energy is the cornerstone that has enabled human civilization to emerge and develop. From the slash-and-burn agriculture of our ancestors from tens of thousands of years ago to the modern industrial and technological revolutions, it can be regarded as a grand epic of the changes in how humans obtain and use energy. The global population has been growing alarmingly, especially in the modern world. In particular, the exponential growth of the global population since the beginning of the modern era has resulted in an unprecedented energy demand. The energy demand is even greater than ever before. To this day, humans obtain energy mainly through fossil energy sources such as coal, oil and natural gas. However, due to the limited storage, uneven distribution and non-renewable nature of these fossil energy sources, many countries and regions are experiencing increasingly serious problems.

However, because these fossil energy sources are limited, unevenly distributed and non-renewable, a large number of countries and regions are experiencing an increasingly severe energy crisis. The large amount of CO_2 produced when fossil energy is used accelerates global warming, and other harmful gases are causing serious environmental pollution. Therefore, it is important to change energy. Hence, all countries need to change the energy structure and develop and utilize new clean, low-pollution and renewable energy sources. A series of new energy sources, such as nuclear energy, wind energy, solar energy and tidal energy, have been applied successively in this context. Among them, solar energy stands out because of its "inexhaustible" and zero-emission non-polluting characteristics and is the most ideal clean energy in the future clean energy in the future. The share of solar energy in new energy sources is increasing year by year. As a new type of light absorbing material, organic-inorganic hybrid perovskite has an excellent absorption coefficient, small exciton binding energy, high carrier mobility and long carrier diffusion distance. Therefore, the photoelectric conversion efficiency (PCE) of perovskite solar cells increased rapidly from 3.8% to more than 26% in just a few years, showing broad application prospects.

2.1.1 Characteristics of Perovskite Materials

(1) Suitable and easily adjustable band gap widths

Organic and inorganic hybridized chalcogenides have a suitable band gap (Energy Gap, Eg), for example, the Eg of $MAPbI_3$ chalcogenides is 1.5 eV, which ensures the effective absorption of the PSCs in the solar spectrum, and it is within the Eg range that is most suitable for use as the active layer of photovoltaics cells.[1] In addition, the Eg of chalcogenide is flexible and easy to adjust. By replacing and combining ions on the A, B and X positions, countless kinds of chalcogenide materials can be obtained, and the Eg can be adjusted at will within a wide range.

(2) High absorption coefficient

Organic and inorganic hybridized perovskite materials have very high absorption coefficients, and the absorption coefficient of 500 nm thick $MAPbI_3$ chalcogenides is about 105 cm^{-1}, which is one order of magnitude higher than that of GaAs films of the same thickness.[2] Such a high absorption coefficient ensures that PSCs can fully utilize the sunlight within the absorption band gap.

(3) Low exciton binding energy

Organic and inorganic hybridized chalcogenides have a low exciton binding energy of about 2 ~ 50 mV, which is much smaller than GaAs, CIGS, and other materials.[3,4] The low exciton binding energy ensures that the photogenerated excitons in PSCs can be quickly split to produce electrons and hole carriers to be utilized by PSCs, which is also the guarantee of high photoelectric conversion efficiency.

(4) Long carrier diffusion distance

Organic-inorganic hybridized chalcogenide has a relatively long carrier diffusion distance, generally more than 1 μm, while in traditional photovoltaic materials the carrier diffusion length of about tens of nanometers.[5] The long carrier diffusion distance of chalcogenide materials is determined by the low concentration of defect states in chalcogenide films and the characteristics of bipolar transport, which avoids carrier complexation during the transport process.[6]

2.1.2 Crystal structure of perovskite materials

The term perovskite originated from the mineral $CaTiO_3$, which was discovered and studied by the Russian mineralogist Perovskite in 1839.[7] In honor of his contribution, the scientific community named all compounds with perovskite structures after him, under the name "Perovskite". Perovskite is a special crystal. Its crystal structure is

shown in Figure 2.1 and can be represented by ABX_3.[8] The B-site metal ion and the surrounding 6 X negative ions form the octahedral structure BX_6, with the metal ion located in the center of the octahedron. The octahedral structure shares X anions with the six surrounding octahedrons, forming a BX_6 octahedral corner-sharing structure. This is repeated, forming a three-dimensional network structure. The A-position cations occupy the cavity between the regular octahedrons.

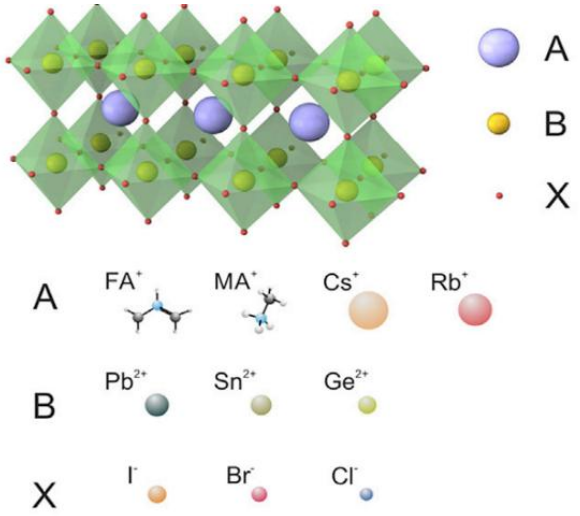

Figure 2.1 Crystal structure of ABX_3 perovskite with different atoms.[8]

In PSCs, the A-position cations of perovskite active materials are generally $CH_3NH_3^+$ (MA^+), $NH{=}CHNH_3^+$ (FA^+), Cs^+, etc. B is a metal ion, usually Pb^{2+}, Sn^{2+}, etc. The X anions are Cl^-, Br^-, I^-, etc. The half-size of these ions is the key to determining whether the perovskite structure is stable and can be determined by the tolerance factor (τ) and octahedral factor (μ). When $0.81 \leq \tau \leq 1.11$, $0.44 \leq \mu \leq 0.90$, a stable perovskite structure can be formed, otherwise only a non-perovskite phase, δ phase, can be formed (Figure 2.2).[9]

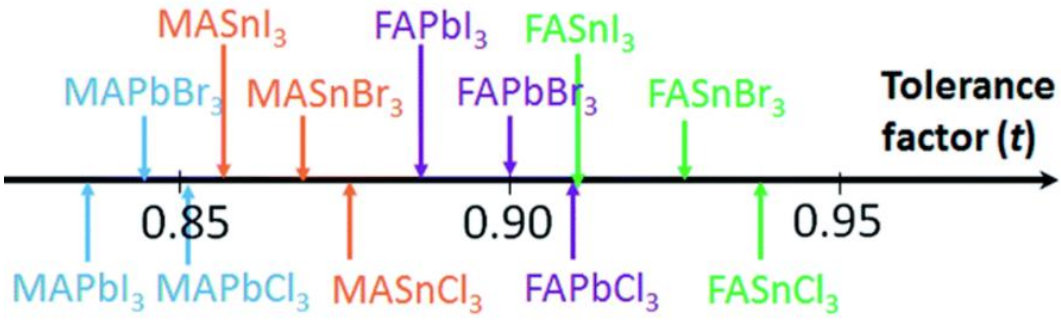

Figure 2.2 Illustration of tolerance factor in perovskites with different compositions.[9]

In addition, the perovskite phase of the octahedral structure also changes with temperature. As shown in Figure 2.3, at room temperature, the stable crystal structure of $CsPbI_3$ perovskite is a ruse crystal, also known as the δ phase (light yellow), with a band gap width of 2.8 eV, which is almost non-conductive and cannot be used for photovoltaic power generation.[10] When the temperature rises to 360 °C, $CsPbI_3$ perovskite will change from a pale yellow δ phase to a black α phase, in a similar process. The band gap width of α-phase $CsPbI_3$ perovskite is 1.7 eV and carrier mobility is 25 cm^2V^{-1} s^{-1}, which meets the PSCs perovskite active layer requirements. Like organic and inorganic hybrid perovskites, octahedral symmetry decreases at low temperatures. When the temperature drops to 260 °C and 175 °C, respectively, the lattice symmetry of α phase $CsPbI_3$ perovskite will gradually decrease, and the process will be divided into β phase and γ phase. The band gap width and mobility of $CsPbI_3$ perovskites in β and γ phases did not change significantly and could still be used for PSCs. As the temperature decreases and the water vapor triggers, the γ phase $CsPbI_3$ will return to the δ phase.

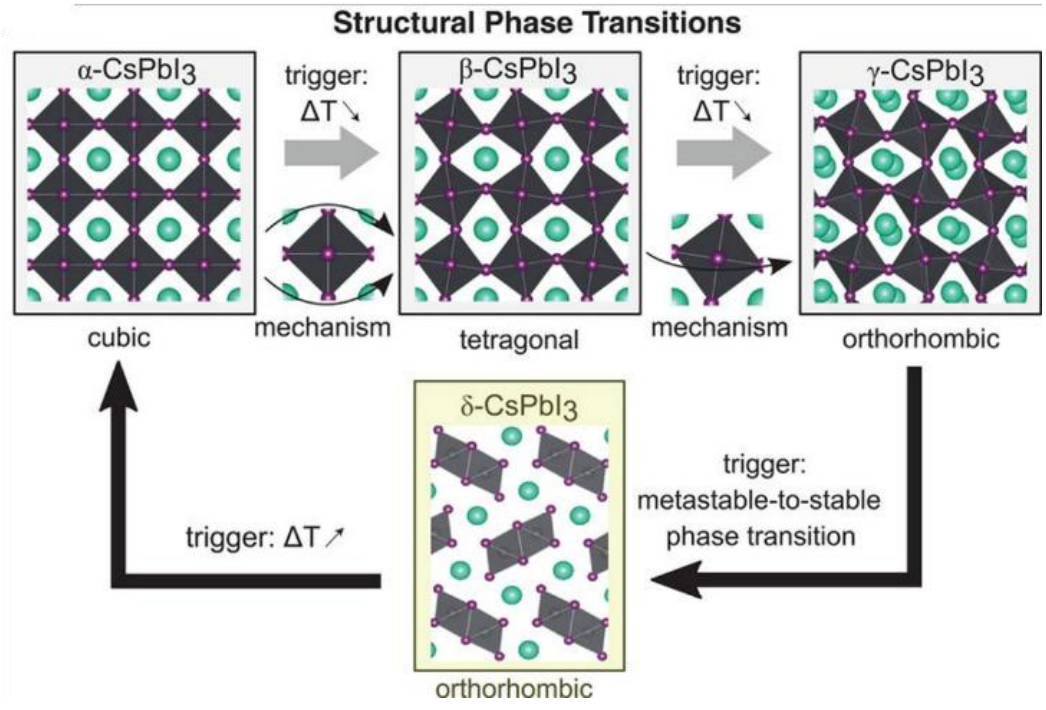

Figure 2.3 Schematic diagram of the phase transition process of all-inorganic $CsPbI_3$ perovskite crystals.[10]

2.2 The Perovskite Nanomaterials

Perovskite nanomaterials are materials that are less than 100 nanometers (nm) in size.

Examples include quantum dots, nanosheets and nanowires, the most common types of nanomaterials.[11] Compared to perovskite bulk and thin film materials, perovskite nanomaterials are formed at the nanoscale, thus forming a unique quantum size effect, which can significantly improve the properties of the materials. For example, perovskite nanomaterials have fewer defects, higher exciton binding energy, and higher quantum efficiency than perovskite single crystals.[12] Compared with the complex process and high-cost preparation process of perovskite single crystals, the manufacturing process of perovskite nanomaterials is simpler and lower cost. On October 4, 2023, for the "discovery and synthesis of quantum dots," Monji Bavendi from the Massachusetts Institute of Technology, Louis Bruce from Columbia University, and Russian physicist Alexei Ikimov were awarded the 2023 Nobel Prize in Chemistry. In general, the properties of an element depend on how many electrons it has. When semiconductors are reduced to nanometer sizes, an unusual phenomenon occurs as the size decreases, the bandwidth increases, resulting in a "blue shift," where the emitted light becomes increasingly blue. Conversely, as the size increases, the bandwidth decreases, leading to a "red shift," where the emitted light becomes progressively redder.[13, 14] This strange phenomenon is also known as the "quantum size effect." A quantum dot is a kind of semiconductor nanoparticle, its size is very small, from a few nanometers to ten nanometers, cadmium selenide, indium phosphide and other common quantum dot materials. Because of the quantum size effect, the colour of light will be different for different sizes of cadmium selenide nanoparticles.[15] John Oquist, chairman of the Nobel Committee for Chemistry, said: "Quantum dots have many fascinating and unusual properties. Importantly, they come in different colours depending on their size. Figure 2.4 shows the morphologies of perovskite nanomaterials of different sizes.[16] Therefore, perovskite nanomaterials have great potentials to be developed in flexible electronics, micro sensors, solar cells and sensors.

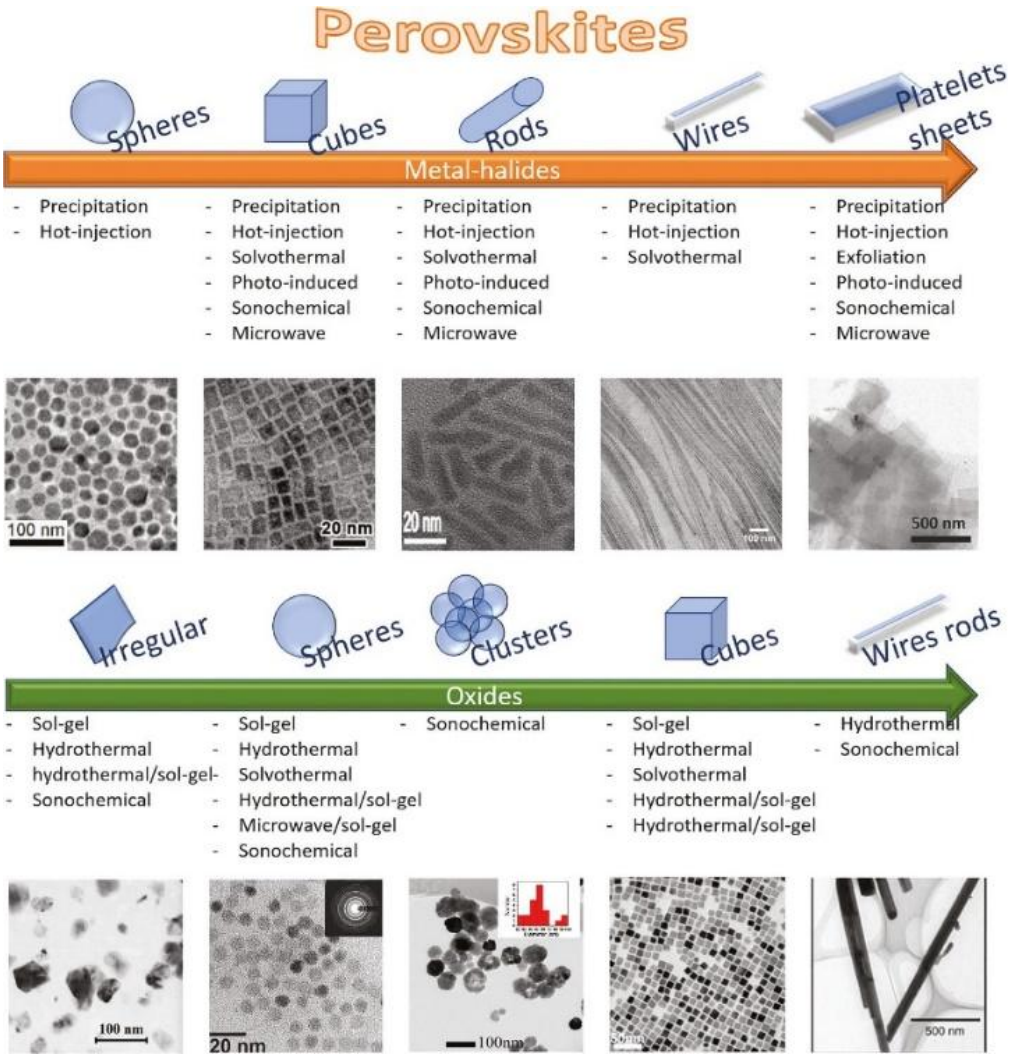

Figure 2.4 Perovskite nanomaterials of different sizes obtained by different synthesis methods.[16]

2.2.1 Synthesis methods of Perovskite nanomaterials

(1) Template Synthesis Method

The template method is based on the processed mesoporous template of nanometer size. A perovskite nanomaterial with adjustable size was obtained by spinning the perovskite precursor solution on the template and annealing and drying it. There are four commonly used mesoporous templates: mesoporous silicon nanowires, mesoporous silica dioxide, mesoporous metal oxides, and metal-organic frameworks. In 2016, Zhang et al. used an oriented microporous metal-organic framework as a growth template to synthesize the $MAPbI_2X$ (X = I, Br and Cl) QDs. The synthesis process is shown in Figure 2.5 below.[17] To overcome the impact of structural inhomogeneities in optoelectronic properties of nanoscale structures, Michael et al. conducted the template

of anodized aluminium oxide (AAO) to synthesize perovskite ($CH_3NH_3PbI_3$, $CH_3NH_3PbBr_3$ and $CsSnI_6$) nanowire arrays.[18]

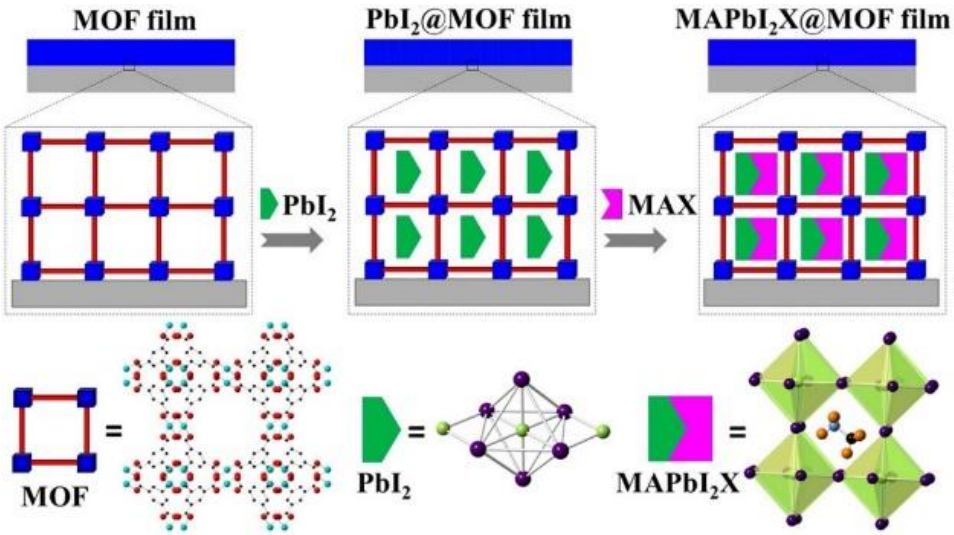

Figure 2.5 Schematic diagram in the synthesis process of $MAPbI_2X$ (X = Cl, I and Br) perovskite QDs in MOF module.[17]

(2) Hot Injection Synthesis Method

The most common method to synthesize the perovskite nanomaterials is the hot injection method. The synthesis process by hot injection can be divided into three parts: dissolution of the synthesized material, injection of the precursor solution and quenching of the reaction. However, most of the hot injection methods need to be carried out at high temperatures and therefore require high boiling polar solvents to ensure successful synthesis. The nanocrystals synthesized by this method have good crystallinity, fewer defects and better stability. In 2015, Kovalenko successfully synthesized $CsPbX_3$ (X = I, Br and Cl) nanocrystals with different luminescent colours for the first time using the hot injection method, as shown in Figure 2.6.[19] Thus, during the synthesis, the size and morphology of the nanocrystals can be controlled by controlling the injection temperature of the precursor, the time of the reaction and the ratio of the synthesized materials. Additionally, the stable lead-free (e.g. tin-based) perovskite nanocrystals ($CsSnBr_3$) were also synthesized by the hot injection method.[20] Notable efforts were made in the hot injection approach to lead to a favorable optoelectronics property in perovskite nanomaterials and extend the potential for photovoltaic.

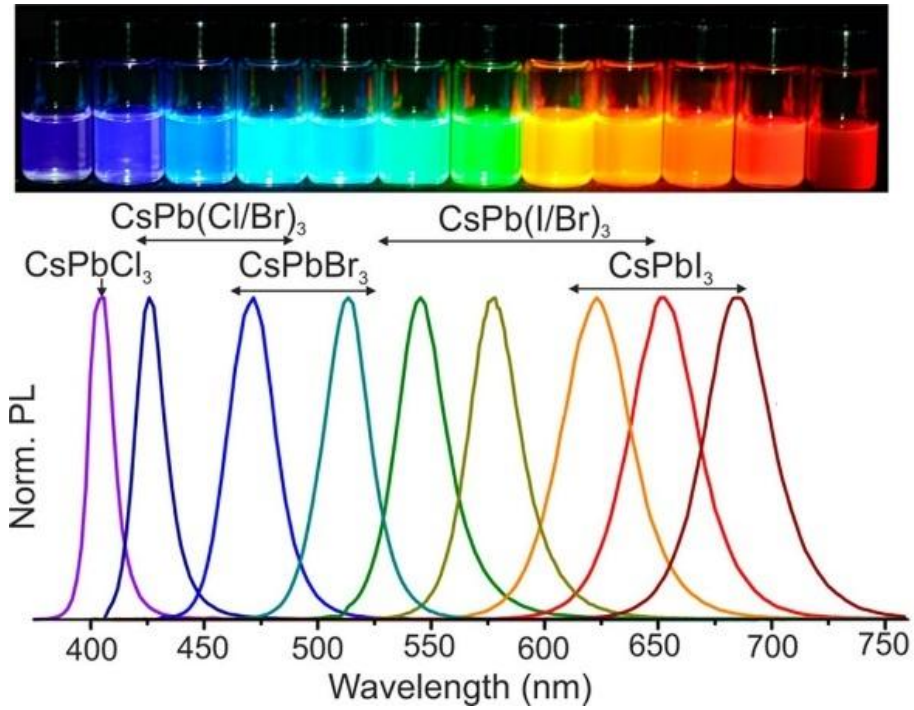

Figure 2.6 $CsPbX_3$ (X =Cl, Br, and I) perovskite nanocrystals with different emission colors under 365 nm UV light by using the hot injection method.[19]

(3) Ligand-Assisted Reprecipitation Synthesis Method

The ligand-assisted Reprecipitation Synthesis Method (LARP) is used to synthesize nanocrystals by exploiting the aggregation properties of chalcogenide materials. This method has a simple operation process, low production cost and excellent optical performance products. In 2015, Zhong's group synthesized $CH_3NH_3PbBr_3$ quantum dots with an average size of 3.3 nm for the first time by using the LARP method, and these $CH_3NH_3PbX_3$ (X = I, Br and Cl) quantum dots have tunable luminescence position and luminescence quantum yield as high as 70% as well as narrow emission with a full width at half maximum (FWHM) of about 20-50 nm. Just as shown in Figure 2.7, the process of the LARP method used to synthesize $CH_3NH_3PbBr_3$ is divided into two steps.[21] Because of the low PLQY, insufficient stability, etc., the blue-emitting perovskite nanoplates (NPLs) were synthesized by the LARP method. These $CsPbBr_3$ NPLs (thickness from 2 to 6 monolayers) show a narrow photoluminescence peak (432-515 nm), and a high PLQY up to 75%, which is favorable for the application of perovskite LEDs.[22]

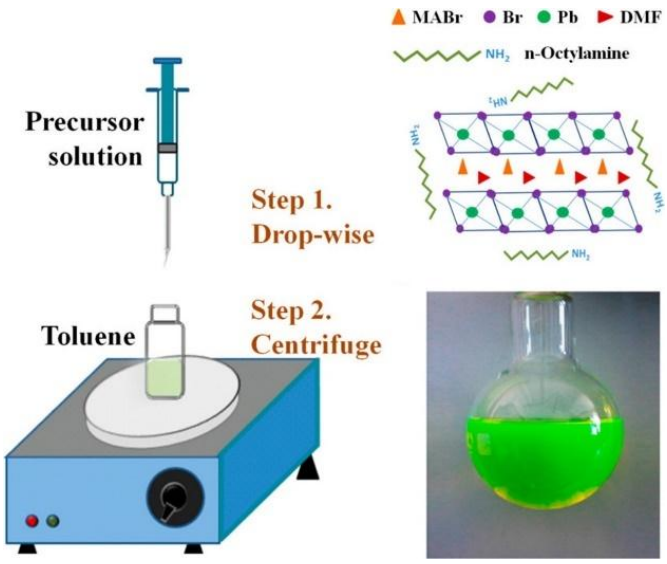

Figure 2.7 Schematic diagram in the synthesis process of $CH_3NH_3PbBr_3$ QDs using the LARP method.[21]

(4) Ultrasound Synthes Method

Ultrasonic synthesis methods are simpler, more efficient and more environmentally friendly than the above synthesis methods that require the use of polar solvents. On the one hand, most of those polar solvents are toxic and not easy to remove completely. The residual polar solvents not only tend to accelerate the decomposition of chalcogenide nanocrystals, but also the long-chain amine ligands will affect the conductivity of chalcogenide nanocrystals in optoelectronic devices. In 2016, Song's group prepared a series of chalcogenide nanocrystals of $APbX_3$ by ultrasonic synthesis. As shown in Figure 2.8, the component chalcogenide precursor materials AX: PbX_2: OAm were dissolved in toluene in the ratio of 1:1:3, and then ultrasonication was performed to control the synthesis rate of chalcogenide nanocrystals.[23]

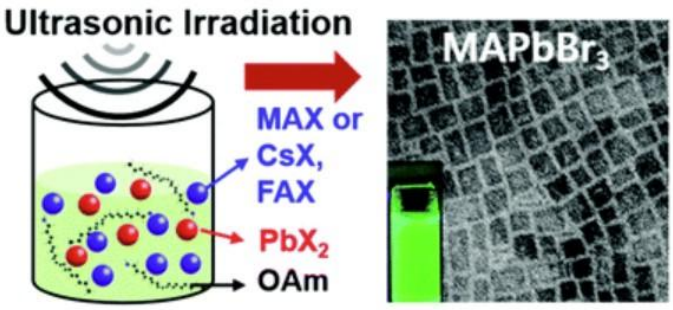

Figure 2.8 Schematic diagram in the ultrasound-induced synthesis process of $MAPbBr_3$ nanocrystals and morphology.[23]

(5) Other Synthesis Methods

In addition to the several methods mentioned above, which have been used primarily for the synthesis of perovskite nanomaterials, there are several other methods such as chemicals vapour deposition synthesis (CVD), microfluidic reactor synthesis method, mechanical ball milling method, hydrothermal method and so on (Figure 2.9).[24]

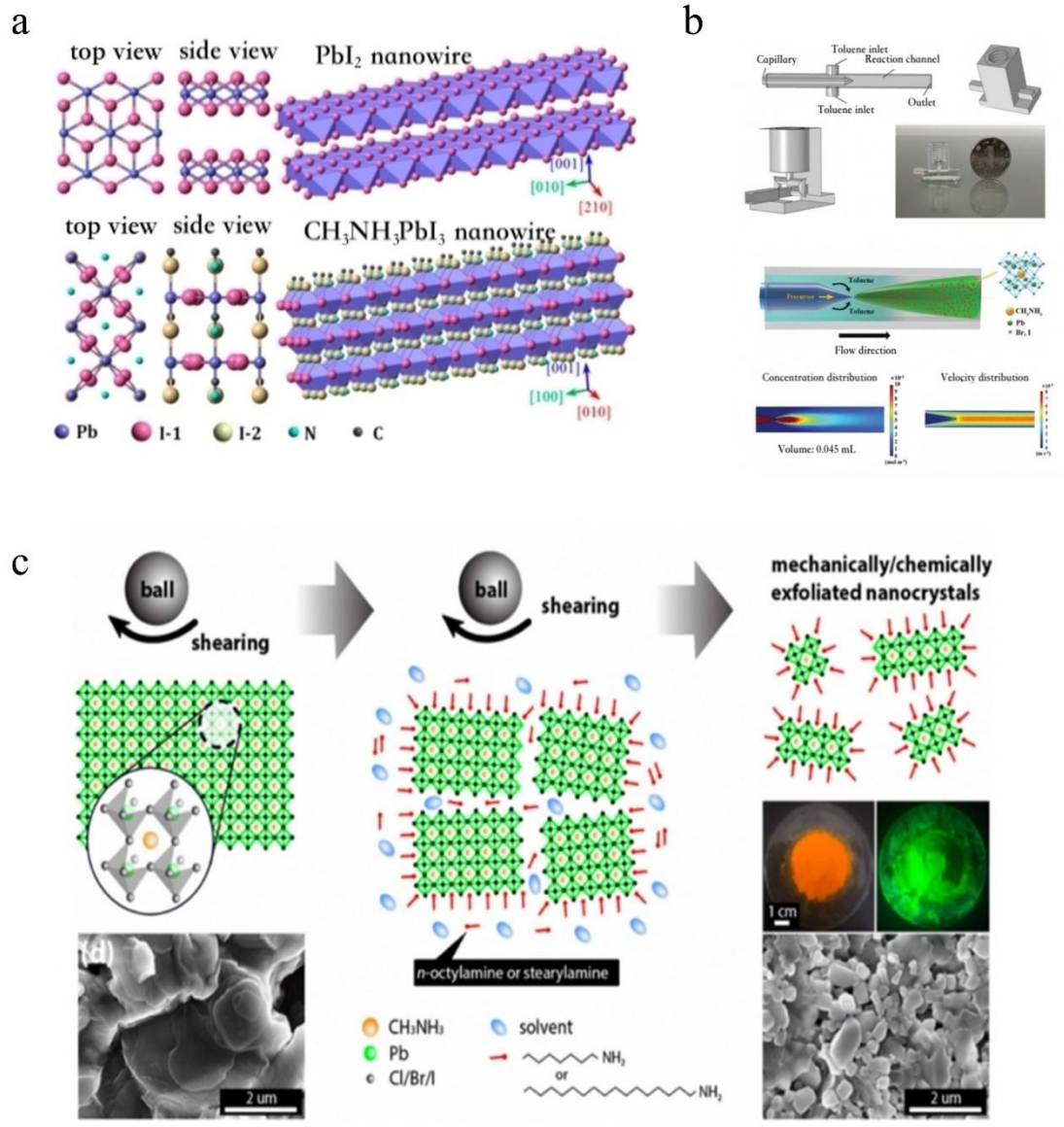

Figure 2.9 (a) Conventional CVD method of synthesis of PbI_2 and $CH_3NH_3PbI_3$ nanowires. (b) The synthesis process of $MAPbX_3$ (X = I and Br) nanocrystals using the microfluidic reactor method. (c) Schematic diagram of reaction process in mechanical ball milling synthesis method.[24]

2.2.2 Applications of Perovskite nanomaterials

(1) Perovskite light-emitting diodes (PeLEDs)

Perovskite nanocrystals have emerged as a favourable candidate for the next generation of sharper and more vivid light-emitting diodes due to their high PLQY of up to 100%, narrow emission fwhm of a few tens of nanometers, and the possibility of emission position tuning across the entire visible spectrum region. The most conventional device structures used in PeLEDs are inverted and forward structures, as shown in Figure 2.10.[25] The PeLED devices always include a transparent electrode, hole transport layer (HTL), perovskite nanocrystals emitting material layer (EML), electron transport layer (ETL), and a back electrode. The principle of the PeLED is that under the applied voltage, holes and electrons are transmitted from the anode and cathode respectively to the EML layer, resulting in radiation recombination for luminescence performance. The rare-earth-based perovskite nanomaterials are promising candidates to modulate the properties of perovskites, including flexible redox characteristics, electromagnetic properties, unique luminesce and so on, which enables these materials favourable for PeLEDs.[26]

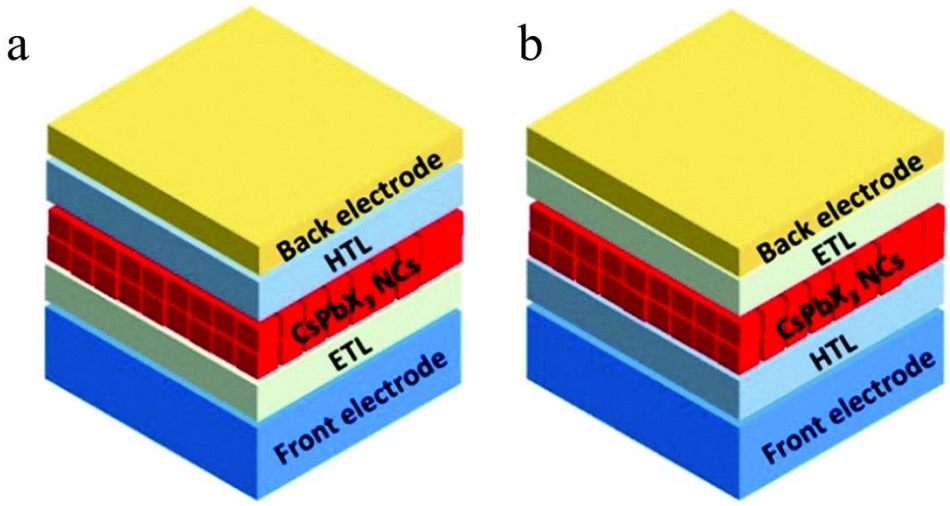

Figure 2.10 Conventional device structure of forward and inverted $CsPbX_3$ NCs PeLEDs.[25]

(2) Perovskite solar cells (PSCs).

Benefiting from its adjustable band gap, simple preparation process and controllable surface chemistry, perovskite nanomaterials have great potential in the application of solar cells. In 2016, Akkerman et al. first used $CsPbBr_3$ NCs to fabricate PSCs and

achieved a PCE exceeding 5%, as shown in Figure 2.11.[27] Since then, a great deal of scientific research has been devoted to improving the efficiency of PSCs, for example, in-situ doping and passivation, ligand manipulation, surface engineering, post-treatment, device-structure engineering and so on. Currently, the highest PCE of PSCs in nanomaterials is 19.1%.[28]

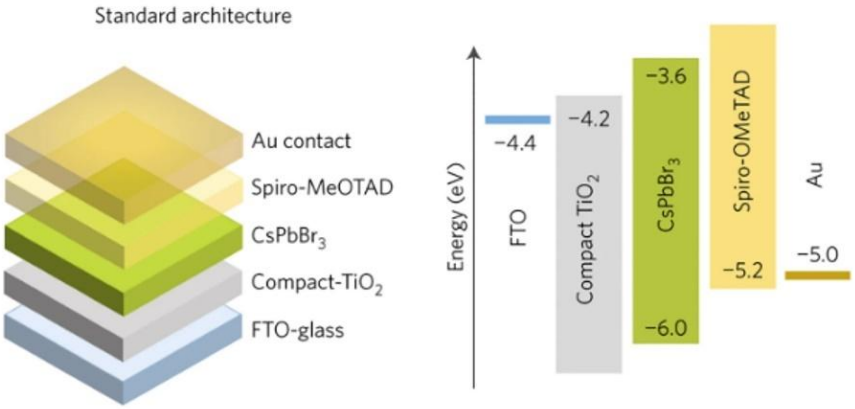

Figure 2.11 Schematic diagram of the device architecture in $CsPbBr_3$ solar cells and the energy level of each layer.[27]

(3) Perovskite Laser

Perovskite nanomaterials have exhibited excellent optical absorption and emission properties. Research has found that perovskite nanomaterials have very high photon-to-electric conversion efficiency and can achieve broad-spectrum absorption and tunable narrow-band emission, providing a good foundation for the fabrication of laser devices. In 2021, Liang et al. synthesized the $CsPb_2Br_5$ microplatelet by hydrothermal method and used it as a natural Fabry-Perot microcavity. Then the situ crystallization of the $CsPbBr_3$ nanocrystals was realized in the $CsPb_2Br_5$ to form the waterproof $CsPbBr_3/CsPb_2Br_5$ core-shell heterostructure. The laser-induced luminescence of $CsPbBr_3/CsPb_2Br_5$ core-shell heterostructure with different patterns was realized. The $CsPb_2Br_5$ matrix offers the better choice to fabricate the waterproof and thermal-stable perovskite laser (Figure 2.12a).[29] Zhao's group demonstrated a wettability-guided screen-printing method to prepare perovskite microdisk laser arrays with large-scale and multicolour. The process of the patterned template is shown in the Figure 2.12b.[30] Then the perovskite precursor solution was spin-coated on the patterned template to form the perovskite laser arrays. These patterned perovskite lasers can lase at a low

threshold and different colour, which also offer the potential to produce the perovskite LED.

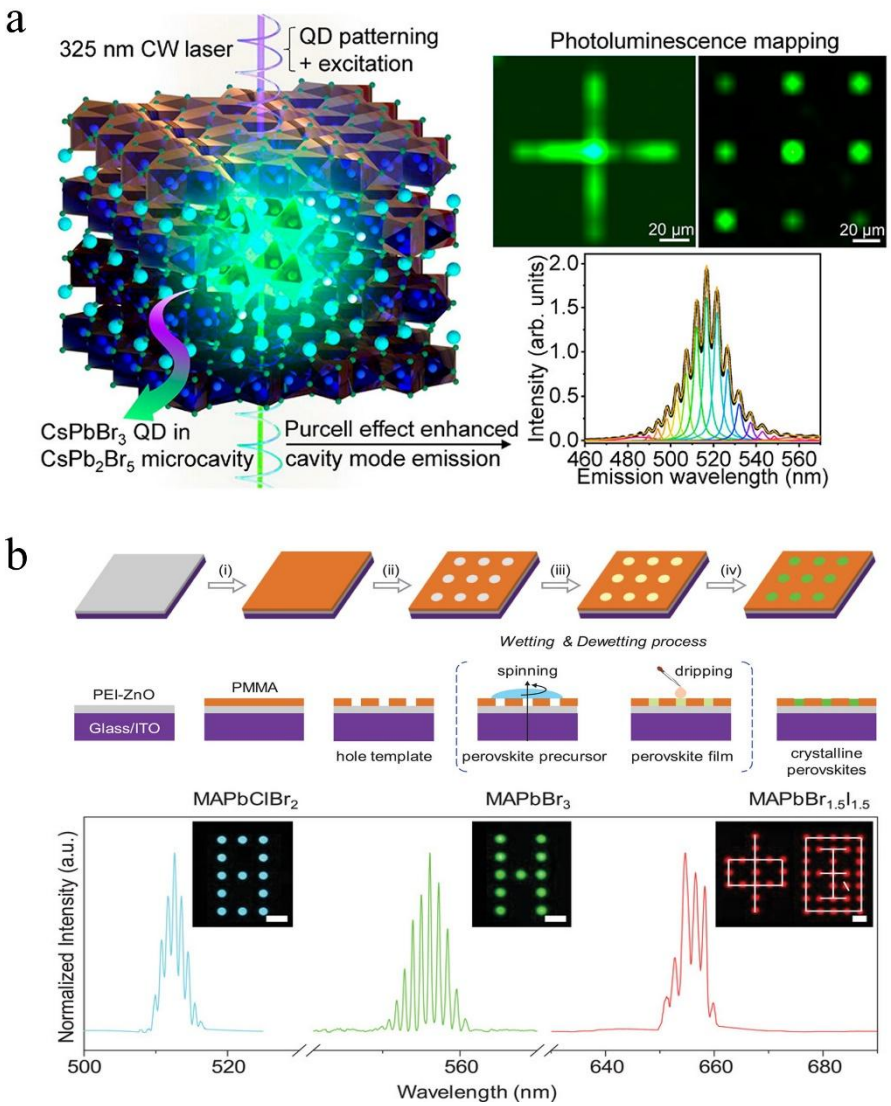

Figure 2.12 (a) Spontaneous emission of the situ crystallized $CsPbBr_3$ QDs induced by a 325 nm continuous wave (CW) laser in $CsPb_2Br_5$ microplatelets.[29] (b) Schematic diagram of the fabrication process of $MAPbX_3$ (X = I, Br and Cl) perovskite microlaser arrays.[30]

(4) Photodetector

Perovskite nanocrystals demonstrate remarkably high charge carrier mobility and long carrier lifetime, which are crucial for efficient charge transport and collection in photodetectors. This leads to high photoconductive gain and fast photoresponse. The first $CsPbI_3$ PNCs photodetector was reported in 2015 with an on/off photocurrent ratio of 10^5 (Figure 2.13a).[31] To solve the stability of $CsPbCl_3$ PNCs, Gong et al. used 3-

mercaptopropionic (MPA) to passivate the $CsPbCl_3$ PNCs surface, then print these PNCs on the graphene field-effect transistors (GFETs). The $CsPbCl_3$ PNCs/GFETs achieved a fast photoresponse time of 0.3s, and a high responsivity of 10^6A/W. Moreover, the $CsPbCl_3$ PNCs can be used to fabricate the flexible device and the optoelectronic performance can be retained after 25 bending cycles (Figure 2.13b).[32] In 2017, Zhen et al. successfully synthesized the $CH_3NH_3PbI_3$ perovskite nanoflakes on a flexible PET substrate by a low-temperature two-step method. The flexible $CH_3NH_3PbI_3$ perovskite nanoflakes photodetector shows a high responsivity of 12 A W-1 and a photoresponse time of 2.2 ms (Figure 2.13c).[33]

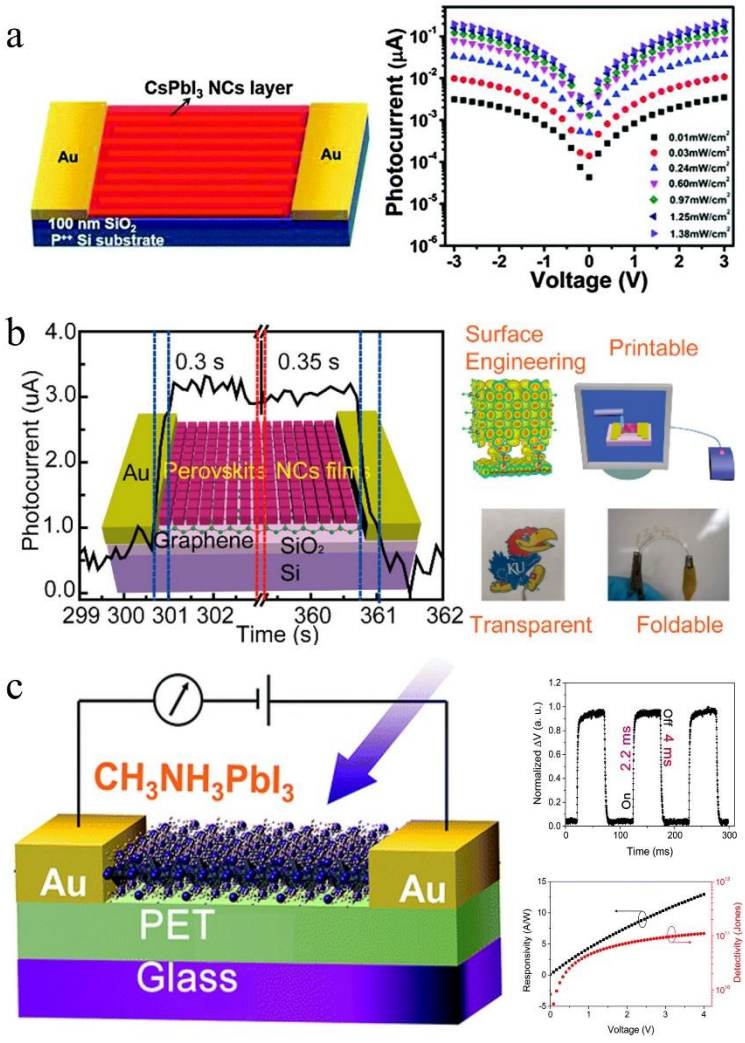

Figure 2.13 (a) Device structure and I-V curves of different incident laser intensity in $CsPbI_3$ NCs photodetector.[31] (b) Schematic of the $CsPbCl_3$ NCs/GFETs heterojunction photodetector based on solid Si/SiO_2 and flexible sunstrate.[32] (c) Diagram of device structure and the photoresponse in $MAPbI_3$ nanoflake flexible photodetector.[33]

2.3 Chiral Perovskites

Chiral materials have low symmetry due to their geometric properties, so they exist in two forms that are mirror images of each other, called enantiomers. Chiral materials differ in photoelectric properties due to their structural differences. Perovskite materials are not only widely used in various optoelectronic devices because of their tunable structural diversity, but also expand the possibility of chiral optoelectronics applications.[34] The first chiral perovskite single crystal was successfully synthesized by Lemmerer did it in 2006 with the solution method.[35]

2.3.1 Basic characterization of chirality

The two main methods used to characterize the chirality of perovskite materials are circular dichroism (CD) spectra and circularly polarized luminescence (CPL) spectra. The CD spectra measure the chiroptical signal of chiral materials in ground states, while CPL demonstrates the signal of chiral materials in excited states.

Circular dichroism refers to the differential absorption of left-circularly polarized (LCP) and right-circularly polarized (RCP) light by chiral materials. The CD signals are decided by the difference $\Delta\varepsilon = \varepsilon_L - \varepsilon_R$. ε_L is the extinction coefficients for LCP and ε_R is the extinction coefficients for RCP. The intensity of CD signals is ellipticity (θ, with the unit of mdegree (mdeg)), which is calculated by the formula:

$$\theta = 32980 \times \Delta\varepsilon \times C \times L \qquad \text{Equation 2.1}$$

Where L is the path length, and C is the concentration.

The absorption dissymmetry factor (g_{abs}) is the other parameter to evaluate the chirality of materials, which is given as

$$g = \frac{\theta}{32980 \times A} \qquad \text{Equation 2.2}$$

Where A is the absorption.[36]

Similarly, the circularly polarized luminescence spectrum measures the difference in fluorescence intensity generated by chiral materials after excitation. The intensity of CD signals is also θ and the luminescence dissymmetry factor (g_{lum}), which is defined as

$$g_{lum} = 2 \times \frac{I_{LCP} - I_{RCP}}{I_{LCP} + I_{RCP}} \qquad \text{Equation 2.3}$$

I_{LCP} and I_{RCP} are the emission intensity of chiral perovskite materials under LCP and RCP.[37]

2.3.2 Chirality Transfer Mechanisms in Chiral Perovskites

For chirality in perovskite materials, the following four chiral mechanisms have been demonstrated:

(1) Chiral-organic molecules induce chiral perovskite crystal structures

(2) Chiral surface distortion or chiral-organic molecule aggregation induced by using chiral-organic molecules

(3) electronic interactions between chiral-organic molecules and achiral perovskite crystal structures

(4) chiral defects (screw dislocations)

The first and fourth mechanisms are the intrinsic chirality of the perovskite crystal structure. And the second and the third mechanisms are the CISS in perovskites.[38]

2.3.3 Synthesis Method of Chiral Perovskites

(1) Direct-induced synthesis

In the direct-induced synthesis of chiral perovskites, the chiral molecules were directly mixed with the perovskites to achieve chiral behaviors (e.g. cooling crystallization, slow-evaporation crystallization, aqueous synthesis, etc.).[39] Moon's research group reported the first direct synthesis of 2D chiral perovskite single crystals in 2017, and it was the first time to use a circular dichroism spectrum to study the chiroptical behaviour of two-dimensional chiral single crystals (Figure 2.14a).[40] The following year 2018, Yuan et al. used antisolvent vapour-assisted crystallization to directly synthesize $(R/S\text{-}MPEA)_{1.5}PbBr_{3.5}(DMSO)_{0.5}$ chiral perovskite nanowires. Based on the chiral perovskite nanowires, the nonlinear optical effect is demonstrated. Tang's group synthesized 1D R- and S-α-$PEAPbI_3$ single crystals in 2019 and the CPL detectors were fabricated based on it chiral 1D R- and S-α-PEA)PbI_3 films. In 2021, Nanosheets with intrinsic chirality are directly synthesized by the introduction of chiral A-site cations R- or S-β-methylphenethylamine (R- or S-MPEA), which are inserted into the perovskite structure to form a chiral crystal structure by chiral amine organic molecules. Moreover, the chiral optical properties of chiral R/S-MPEA perovskite nanosheets were regulated

by controlling the volume of achiral oleic acid, and the highest g-factor was obtained, which was $6.5*10^{-3}$ (Figure 2.14b).[41] As shown in Figure 2.14c, Tian's research group proposed using chiral cysteine additives for ligand-assisted exfoliation to obtain self-assembled chiral Cs_4PbBr_6 nanorods and observed obvious CD and CPL signals.[42]

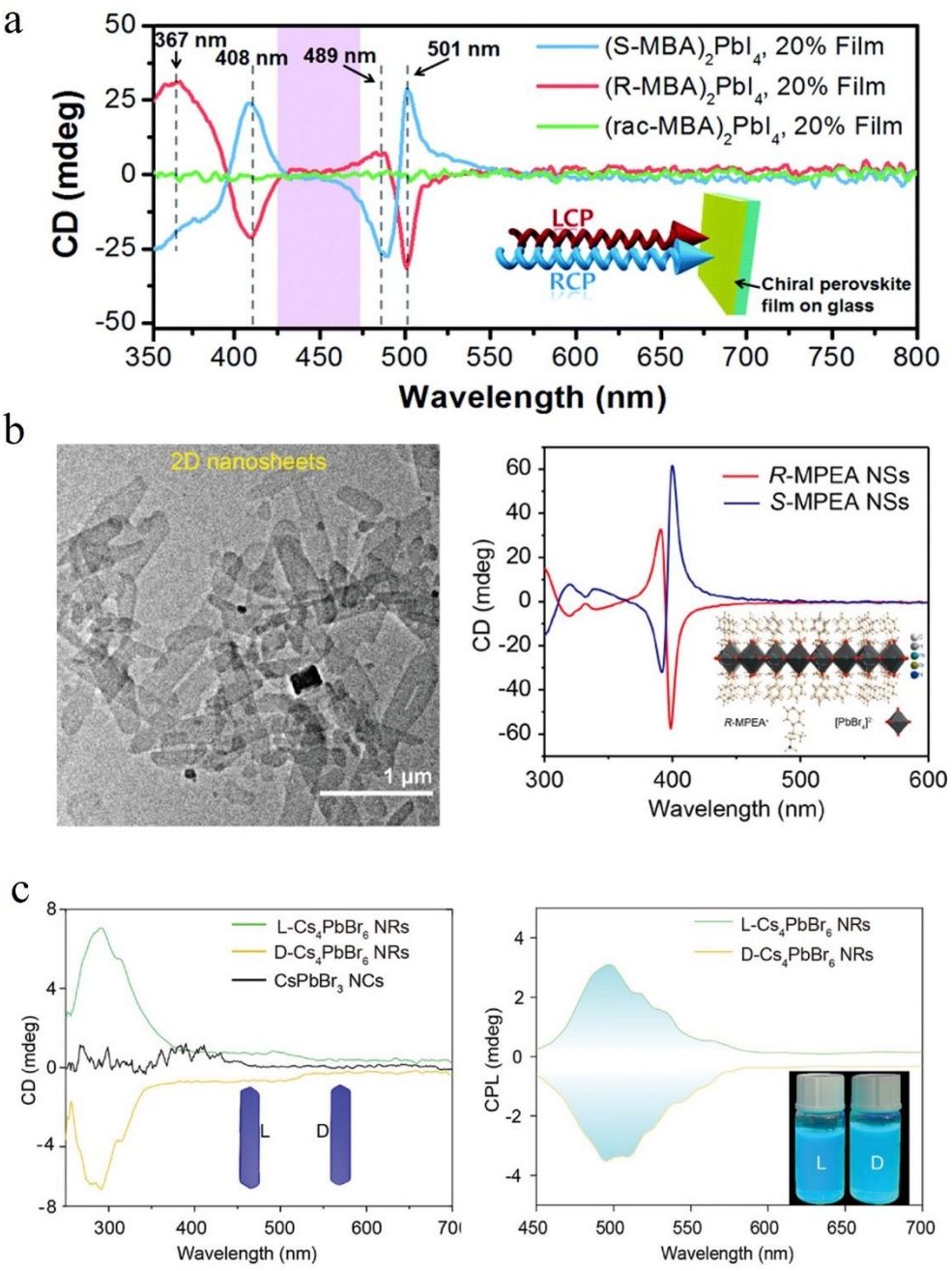

Figure 2.14 (a) The CD spectra of $(R\text{-}MBA)_2PbI_4$, $(S\text{-}MBA)_2PbI_4$, and $(rac\text{-}MBA)_2PbI_4$ films.[40] (b) Schematic diagram of intrinsic chirality in 2D R-/S-MPEA perovskite nanosheets.[41] (c) CD and CPL spectra of chiral L, D-Cs_4PbBr_6 NRs induced by cysteine-capped self-assembly $CsPbBr_3$ NCs.[42]

(2) Chiral ligand-induced synthesis

In contrast to the direct synthesis, the chiral-ligand exchange approach influences the perovskite crystal structure to induce the chirality in it.[43] The first research about chiral perovskite nanocrystals synthesized by post-ligand exchange was also reported in 2017. The CD spectrum revealed that the $CsPb(I/Br)_3$ NCs exhibited negative and positive CD signals after the R- and S-DACH ligand exchange different from the pure R- and S-DACH solutions. They also studied the origin of chirality by experiments and came up with two factors that could contribute to the CD behaviour of $CsPb(I/Br)_3$ NCs with chiral R-/ S-DACH. The first factor is the distortion or defect of the surface of the chiral nanocrystal caused by the chiral ligand and the second is the electronic interactions of the chiral ligand and the nanocrystal around each other (Figure 2.15a).[44] In 2022, Shuang et al. utilized different chiral ammonium halide salts to post-treat the $CsPbBr_3$ NCs to regulate the CD signals in the chiral intensity (longitudinal dimension) and the wavelength range (transverse dimension). Moreover, the highest g-factor (0.0026) reported among chiral PNCs at the time was achieved (Figure 2.15b).[45] In addition, Duan's research group has studied the synthesis of $CsPbBr_3$ perovskite nanocrystals based on chiral ligands (R- and S-a-octylamine). The chiral ligands partially replace the achiral ligands of the $CsPbBr_3$ perovskite nanocrystals, which results in surface distortion of the $CsPbBr_3$ perovskite nanocrystals. Based on this $CsPbBr_3$ chiral perovskite nanocrystal, the first case of upconversion circularly polarized luminescence with two-photon absorption has been reported (Figure 2.15c).[46] In 2018, Georgieva reported that chiral $MAPbBr_3$ nanoplatelets (NPs) with chiral S- or R-phenylethylammonium (S-PEA or R-PEA) ligands, and the CD signals between 400 and 450 nm show that the chirality was imprinted onto $MAPbBr_3$ NPs (Figure 2.15d).[47]

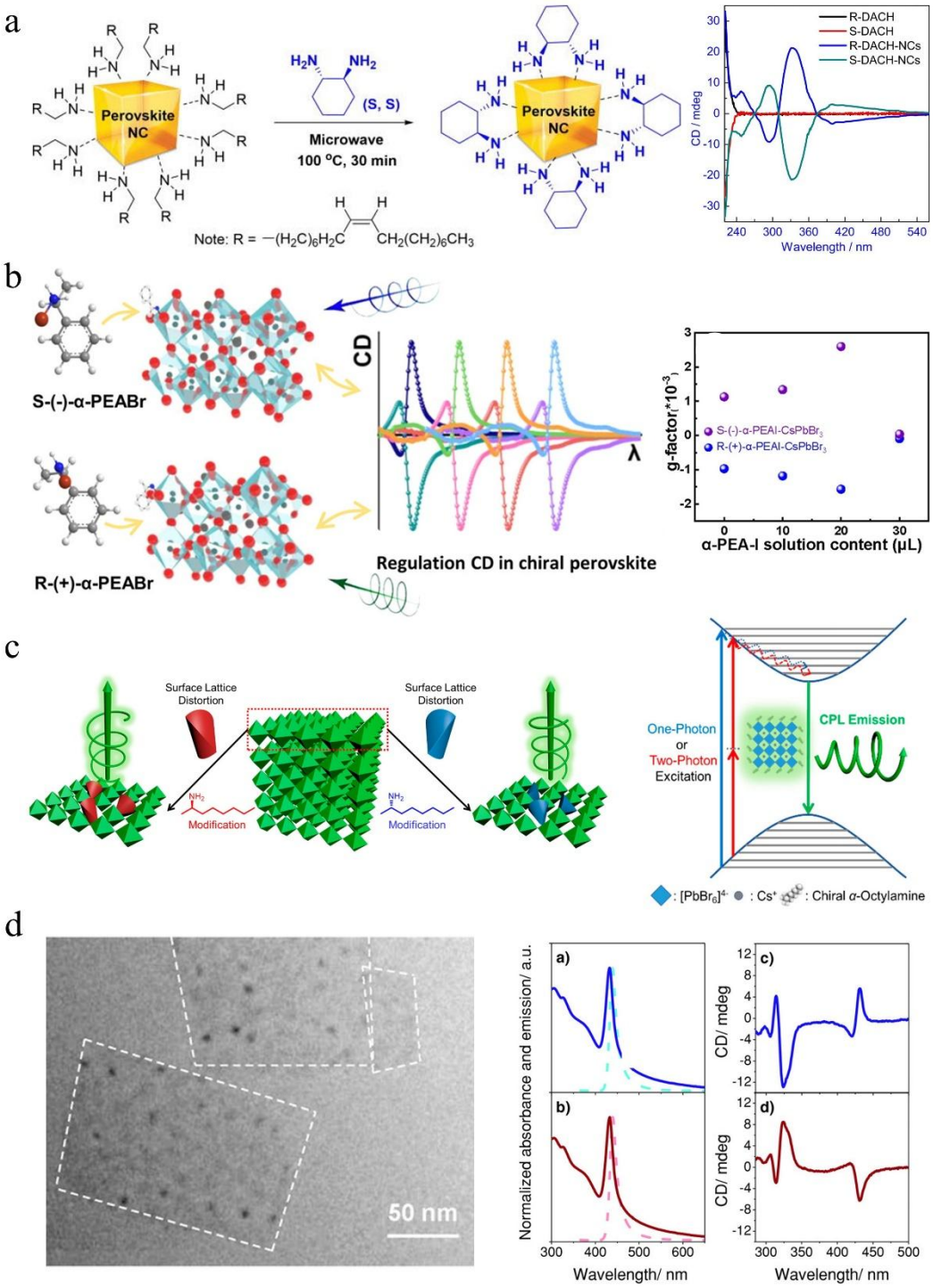

Figure 2.15 (a) The procedure of ligand exchange on perovskite NCs using chiral DACH and the CD spectra of R-/S-DACH perovskite NCs.[44] (b) The CD spectrum and g-factor of chiral R-/S-α-PEA ligand modified $CsPbBr_3$ NCs.[45] (c) Schematic diagram of the chirality and the two-photo absorption-based upconverted circularly polarized luminescence (TP-UCPL) phenomenon in chiral $CsPbBr_3$ perovskite NCs.[46] (d) The absorption and CD spectrum of chiral $MAPbBr_3$ nanoplates.[47]

(3) Chiral assembly combination perovskite nanocrystals

In addition, the chiral self-assembly composed of perovskite nanocrystals and chiral materials also provides unlimited possibilities for developing chiral perovskite materials. Liu's group applied the direct tip sonication method to synthesize the large-scale and high PLQY $CsPbX_3$ (X=I, Br and Cl) perovskite NCs. After the synthesis of the $CsPbX_3$ NCs, the chiral lipid gelators (N, N′-bis(octadecyl)-l-glutamic diamide (LGAm) and its enantiomer DGAm) were coassembled with $CsPbX_3$ NCs to fabricate the chiral cogels. The chirality of chiral molecular was transferred to the $CsPbX_3$ cogels through congelation and an obvious CPL signal was demonstrated compared to the $CsPbX_3$ solutions (Figure 2.16a).[48] Furthermore, Zhao et al. prepared the chiral helical polymer/perovskite nanofibers with outstanding CPL signals through a one-step electrospinning strategy. The PeNCs were used as the fluorescence source, the chiral helical polyacetylene (PSA) served as the chiral source, and the polyacrylonitrile (PAN) was used as an electrospinning matrix. Moreover, the different chiral helical polymer/perovskite hybrid nanofibers were fabricated by adjusting the ratio of halide in it (PSA/B-PSK/PAN (B means blue) and PSA/G-PSK/PAN (G means green)). The g-factors in PSA/B-PSK/PAN are up to 10^{-2} levels of solutions (Figure 2.16b).[49] In 2022, Liu et al. used the chiral liquid crystal (LC) soft helix setups to act as a bilayer structure to fabricate a stable and bright green CPL. This is the first time a g-factor of up to 1.9 has been achieved without using a chiral luminescent material. The PeLC device obtained enhanced emission efficiency, excellent environmental stability, patterned CPL with tunable wavelengths and thermal-switchable CPL solutions (Figure 2.16c).[50] Lu's group first synthesised chiral carbon dots (Ch-CDs)-$CsPbBr_3$ NCs and found an amazing phenomenon that the CD signals of L-CDs-$CsPbBr_3$ and D-CDs-$CsPbBr_3$ were inversed under excitation state which induced by the charge transport from Ch-CDs to perovskite NCs (Figure 2.16d).[51]

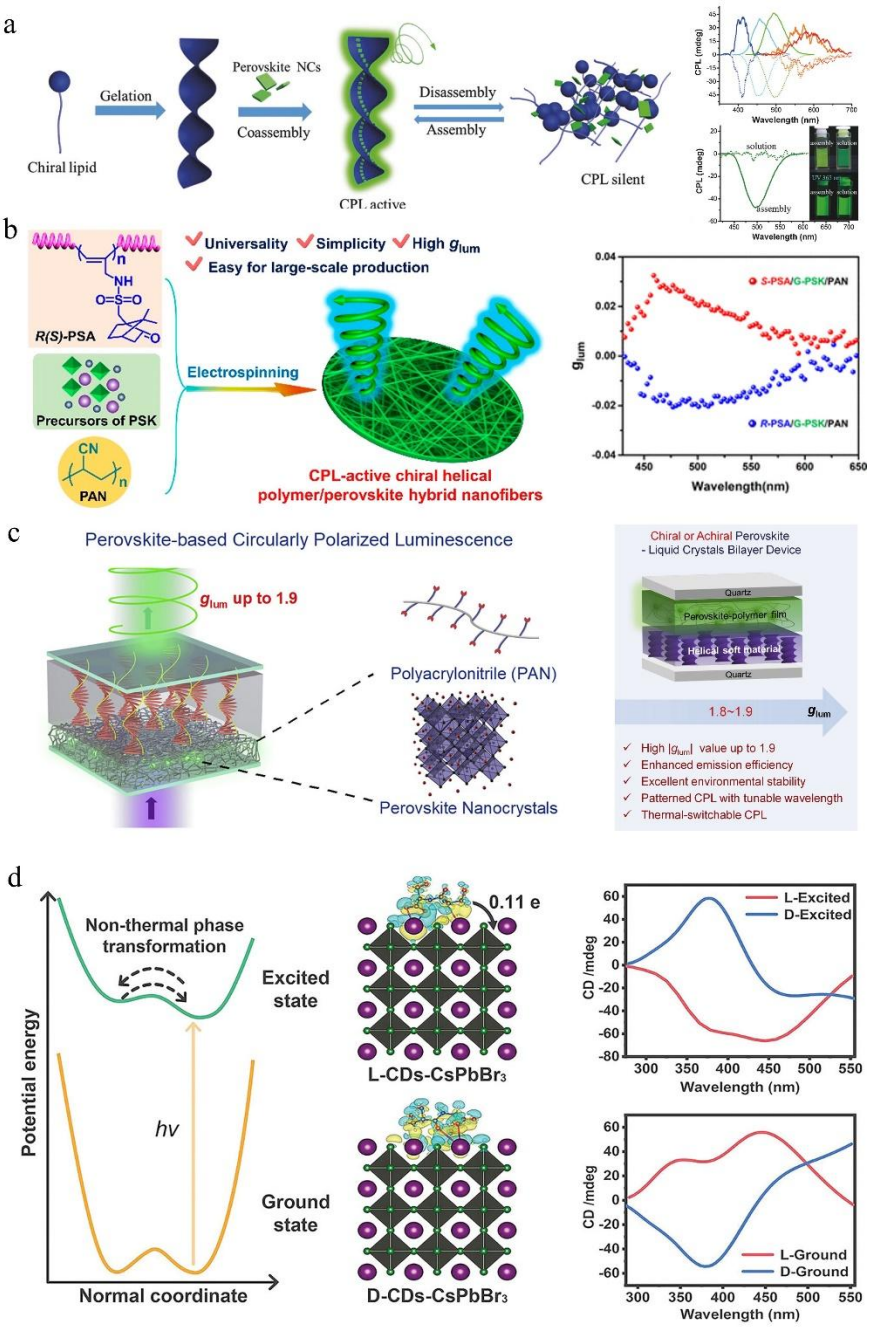

Figure 2.16 (a) Schematic diagram of the chirality of the $CsPbBr_xI_{3-x}$ NCs induced by the coassembly to form gels and the CPL spectrum of the coassembly $CsPbBr_xI_{3-x}$ gels under the excitation of 310 nm laser.[48] (b) Illustration of the electrospinning method to prepare the chiral helical polymer/perovskite nanofibers and the g_{lum} factor of the corresponding chiral PSA/G-PSK/PAN nanofibers.[49] (c) Schematic illustration of the soft helix bilayer architecture of chiral PeLC with enormous advantages.[50] (d) The charge transfer procedure, charge difference plot, and excited and ground state CD spectra of L-/D-CDs-$CsPbBr_3$ NCs.[51]

2.3.4 Optoelectronics Application of Chiral Perovskites

Based on the non-centrosymmetric structure of chiral perovskites, it has possibilities in CPL-PDs, CP-LEDs, spintronics, and ferroelectric devices.[34] Thus, we will briefly introduce some of the main applications of chiral perovskite in the following section.

(1) CPL photodetectors

In 2019, the supramolecular aggregation of pure prolinol-derived squaraines enantiomer, (R, R)- and (S, S)-ProSQ-C6, were implemented in the fabrication of the perovskite bulk heterojunction photodetector (PD) to achieve a maximum dissymmetry factor of circularly polarized photocurrent, ±0.1% (Figure 2.17a).[52] Lin et al. reported the successful synthesis of chiral quasi-2D perovskite single crystals ([(R)-β-MPA]$_2$MAPb$_2$I$_7$ and [(S)-β-MPA]$_2$MAPb$_2$I$_7$ SCs) with chiral β-methylphenethyl ammonium ((R)-β-MPA and (S)-β-MPA). Based on this chiral quasi-2D perovskite SCs fabricated the CPL PD and obtained the highest responsivity of 2D perovskite CPL detectors to date, 1.1A W^{-1} (Figure 2.17b).[53]

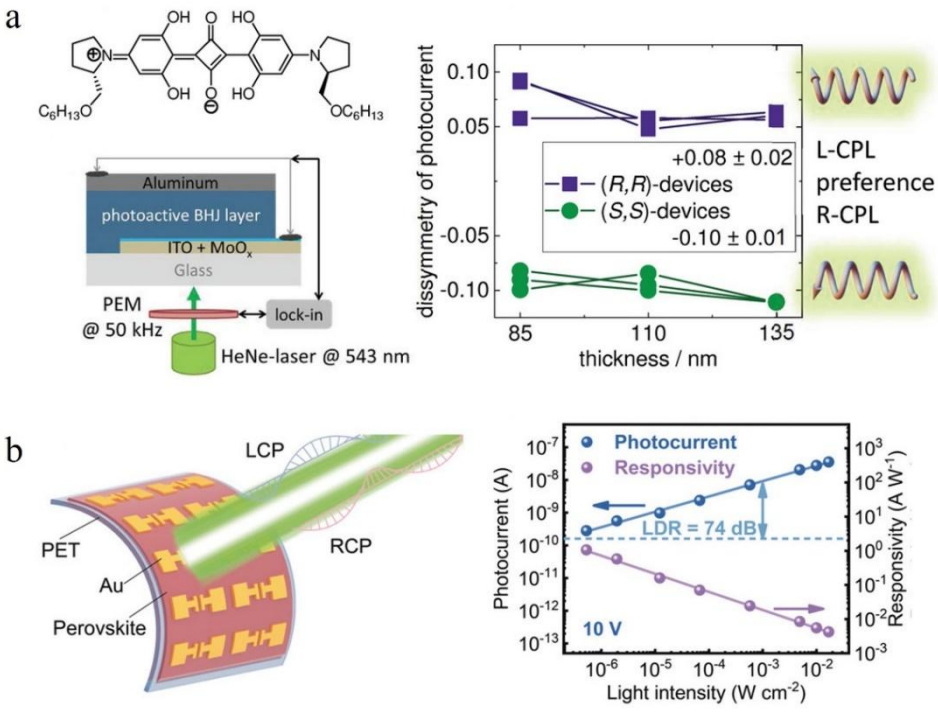

Figure 2.17 (a) Device architecture and dissymmetry of photocurrent in chiral (R, R)- and (S, S)-ProSQ-C6 device.[52] (b)Schematic diagram of the flexible photodetectors based on the chiral ([(R)-β-MPA]$_2$MAPb$_2$I$_7$ films under RCP-532nm and LCP-532nm light and the corresponding photocurrent/responsivity curves.[53]

(2) Circularly polarized LEDs

There are two parameters in CP-LEDs that can be used to evaluate their performance, one is the device performance, that is, the EQE of the LED; The second is the polarization degree (P) of circular polarization electroluminescence (CP-EL), which is defined as:

$$P_{CP-EL} = \frac{I_{left} - I_{right}}{I_{left} + I_{right}} \times 100\% \qquad \text{Equation 2.4}$$

In 2021, Kim et al. reported spin-LEDs based on the CISS organic layer to generate the spin-polarized carriers to transfer the chirality to the $CsPbI_3$ perovskite nanocrystal layer. The spin-LEDs show an EQE up to 10% in (R/S-MBA)$_2PbI_4$/$CsPbI_3$ NCs device and an average P_{CP-EL} of ± 2.6% in (R/S-MBA)$_2PbI_4$/$CsPb(Br_{0.1}I_{0.9})_3$ NCs device in room temperature(Figure 2.18a).[54] Considering that organic amine molecules are widely used in perovskite solar cells to solve energy band matching and stability problems, Yin's research group demonstrated a type-II core-shell $MAPbI_3$ NCs with low-dimensional (S- and R-PEA) chiral shells. The charity is transferred from the chiral shells to the achiral $MAPbI_3$ NCs core. These chiral core-shell NCs LED show a CP-EL emission with a P_{CP-EL} of 0.3% and an EQE of 3.6% at 3.0V (Figure 2.18b).[55]

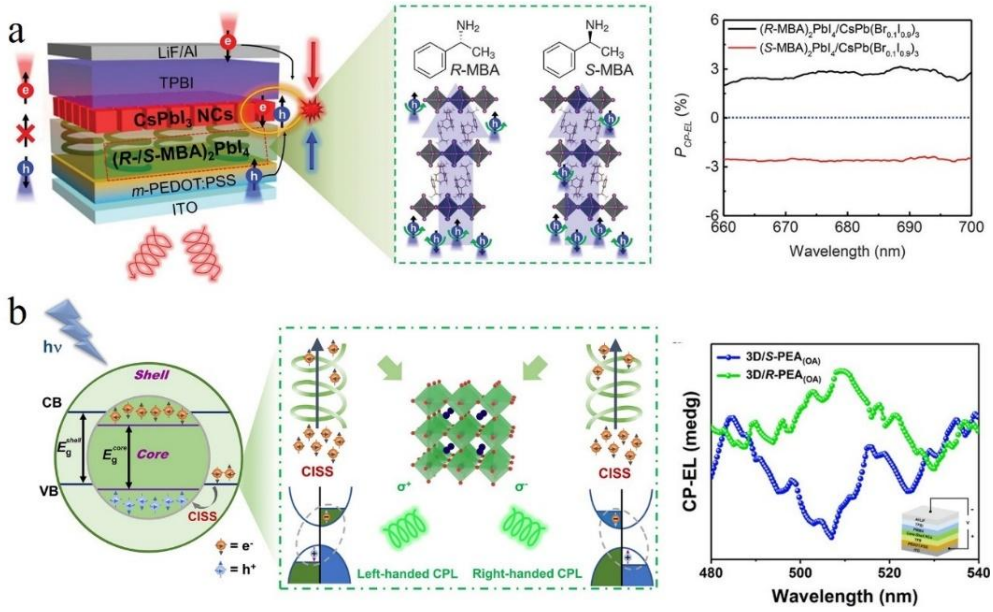

Figure 2.18 (a) Device structure and P_{CP-EL} characteristics in chiral $CsPbI_3$ NCs spin-LEDs based on (R/S-MBA)$_2PbI_4$ perovskite films.[54] (b)Schematic diagram of the core-shell 3D $MAPbBr_3$ perovskite NCs and the corresponding CP-EL spectrum induced by the CISS effect in it.[55]

(3) Spintronics

Among all applications based on the CISS effect, spintronics has been identified as a strong candidate for the next generation of electronics due to its rapid development.[56] In 2019, Lu et al. synthesised the chiral 2D (R/S-MBA)$_2$PbI$_4$ single crystals to fabricate the spin-valve device with a ferromagnetic (FM) electrode. The spin-filtering effect was confirmed by magnetoresistance (MR) measurements in chiral 2D (R/S-MBA)$_2$PbI$_4$ spin-valve devices. The MR is defined by the following formula:

$$\mathrm{MR} = \frac{\mathrm{R(B)-R(0)}}{\mathrm{R(0)}} \times 100\% \qquad \text{Equation 2.5}$$

From Figure 19a, the (R/S-MBA)$_2$PbI$_4$-based spin-valve devices show the exact opposite MR response. Vardeny's group reported another new photovoltaic (PV) application by using the same chiral 2D (R/S-MBA)$_2$PbI$_4$ single crystals.[57] The difference is the structure of the device and the measurement method. As shown in Figure 19b, the photocurrent response was obtained from 2D (R/S-MBA)$_2$PbI$_4$ PV devices under a 486nm laser with LCP and RCP.[58] There is an obvious difference in photocurrent between LCP and RCP, and the relative photocurrent difference is defined by the following formula

$$\Delta \mathrm{I/I} = \frac{\mathrm{I_{LCP}-I_{RCP}}}{(\mathrm{I_{LCP}+I_{RCP}})/2} \times 100\% \qquad \text{Equation 2.6}$$

The largest difference in the photocurrent is about 10% measured at the S-MBA)$_2$PbI$_4$ PV device with different CPL.

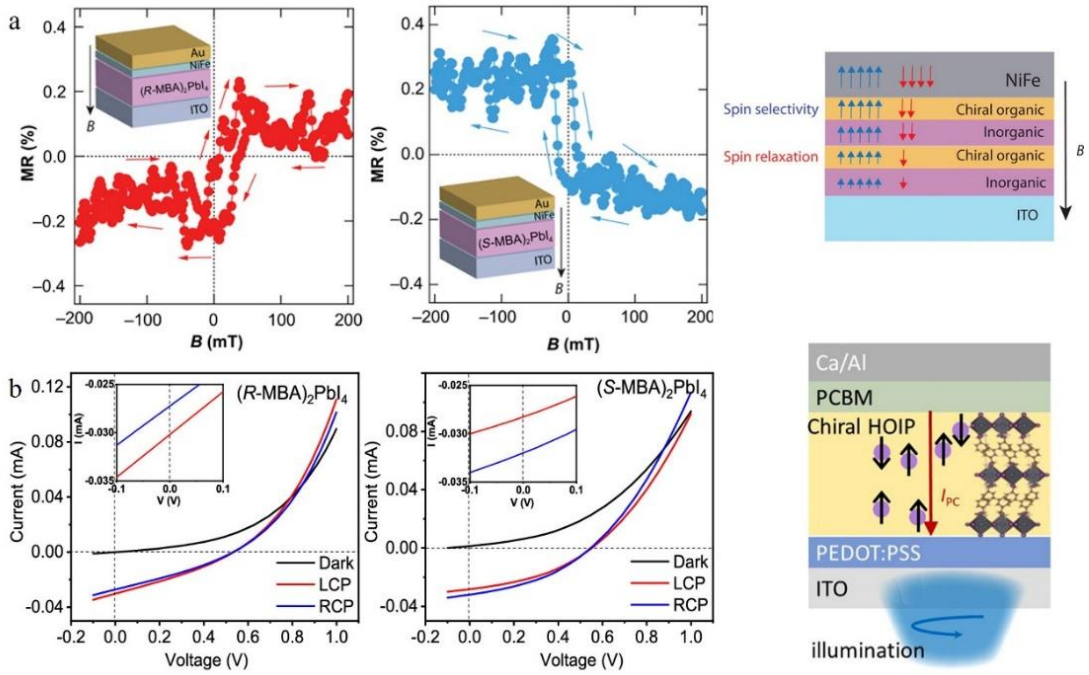

Figure 2.19 (a) Magnetoresistance measurements and spin transport process in the chiral (R/S-MBA)$_2$PbI$_4$-based spintronic devices.[57] (b) Measurements of the photovoltaic response and the schematic illustration of the photocurrent transport under excitation of circularly polarized light in 2D (R/S-MBA)$_2$PbI$_4$ PV devices.[58]

2.4 Spintronics Applications of Chiral Perovskite Materials

Spintronics applications in information technology have evolved rapidly since the discovery of giant magnetoresistance. Compared to traditional semiconductor devices that rely on charge-based transport, spintronics offers several advantages, including low power consumption, high-density memory, and fast processing capabilities. In the field of spintronics, a wide range of materials, including organic molecules, and traditional inorganic semiconductors like gallium arsenide (GaAs) or silicon (Si), have been explored for efficient and multifunctional spintronic devices. Recently, metal halide perovskites have gained significant attention due to their potential applications in spin optoelectronics.[59] However, their suitability for most spin-related applications still faces intrinsic limitations, i.e., the short spin coherence time. The presence of defects and strong spin-orbit coupling (SOC) interactions can lead to rapid spin relaxation and dephasing, hindering the efficient manipulation and control of spins.

2.4.1 Fundamental Principles of Spintronics

Spintronics is a new field which is composed of three traditional information carriers: electron spin, electron spin and photon. As shown in Figure 2.20, three processes of spintronics applied to information technology are electronic transmission for ground data processing, spin assembly for data storage, and finally optical connection for data transmission.[60] Since giant magnetoresistance was reported by scientists in 1988, spintronics has become one of the rapid research fields in the field of nanotechnology. The 2007 Nobel Prize in Physics was awarded to Luke in recognition of his scientific discovery. The discovery is then applied to the hard disk to read the data. Especially in today's information technology explosion, larger capacity data storage is the inevitable trend of future memory development.

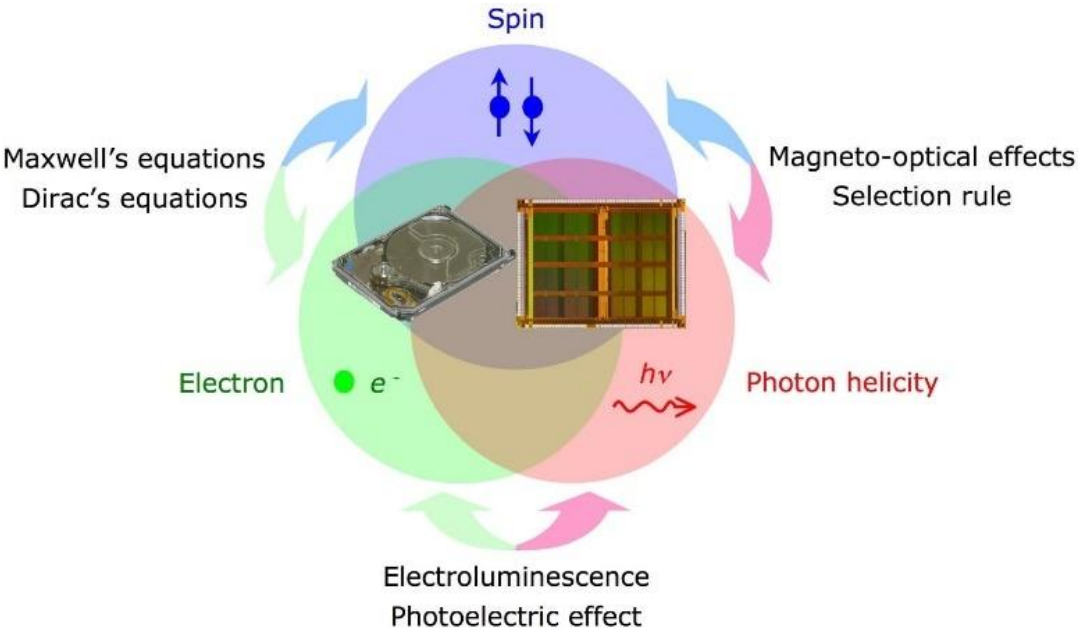

Figure 2.20 Data process of Spintronic device applications.[60]

2.4.2 Progress of Spintronics in Perovskite Materials

Organic-inorganic hybrid halide perovskite materials have made amazing progress in the field of spintronics due to their easy synthesis, adjustable composition, large spin-orbit coupling and spin-dependent photoelectric properties. Compared with the organic semiconductors used in spintronics in the early days, organic-inorganic hybrid halide perovskite materials can be composed of different organic cations, metal ions and halide ions in three-dimensional, two-dimensional, Ruddlesden-Popper phase, one-dimensional and zero-dimensional structure, which provides the possibility of

unlimited developments and opportunities in spintronics. Most of the recent research on spintronics of perovskite materials is based on Rashba splitting in spin-orbit coupling (SOC), chirality-induced spin selectivity (CISS) in chirality-spin coupling, and spin dynamics in charge carriers.[61]

(1) Rashba Effect in Perovskites

The Rashba effect based on the SOC is the most common property studied in the perovskite materials. In 2014, Kim et al. first demonstrated a ferroelectricity-driven Rashba splitting in $CH_3NH_3BX_3$ (B = Sn, Pb; X = Br, I) by first-principles and tight-binding analysis. The SOC and structural inversion asymmetry originate from the Rashba effect, which appears as a splitting of the spin-polarized bands. There are three parameters are utilised to describe the Rashba effect: momentum offset (k_0), Rashba splitting energy (E_0) and Rashba coefficient ($\alpha = 2E_0/k_0$). Niesneret al. reported an experimental finding of Rashba effect in $CH_3NH_3PbBr_3$ single crystals by angle-resolved photoelectron spectroscopy (ARPES) to measure the highest-energy valence band (VB) dispersion. The strongest Rashba splitting of the VB maximum (VBM) by $k_0 = 0.043$ $Å^{-1}$ and a 0.16 eV deep local minimum at the high-symmetry point at the time (Figure 2.21a).[62] Besides the Rashba effect has been found in conventional 3D perovskites, 2D perovskites with large organic amine molecules also show the possibility to exhibit a Rashba effect. For example, as shown in Figure 2.21b, 2D Dion-Jacobson (DJ) perovskite $(AMP)PbI_4$ shows the coexistence of Rashba effect and robust ferroelectricity (where AMP is 4-(aminomethyl)piperidinium. The 2D DJ $(AMP)PbI_4$ show a saturated polarization (P_s) of 9.8 $\mu C/cm^2$ and a Curie temperature (T_c) of 352 K. Thus, the presence of the room temperature Rashba ferroelectric in 2D DJ $(AMP)PbI_4$ perovskites provides a possibility for spintronics applications.[63]

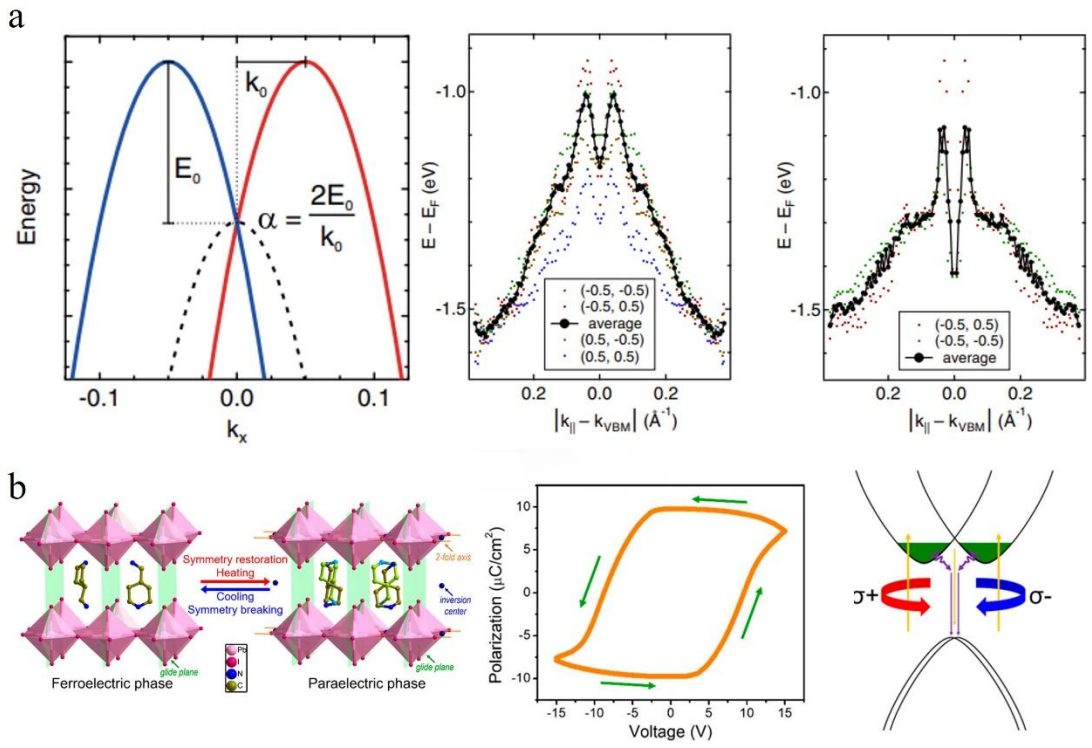

Figure 2.21 (a) Schematic diagram of Rashba splitting and the band dispersion in $CH_3NH_3PbBr_3$ single crystals.[62] (b) Procedure of the symmetry restoration and breaking at 298 K and 373 K and P-V measurements based on the Rashba effect in DJ (AMP)PbI_4 single crystals.[63]

(2) Chirality-induced Spin Selectivity in Perovskites

In 2011, chirality-induced spin selectivity (CISS) was found in organic molecules (double-stranded DNA) using a setup with a nickel substrate controlled by a permanent magnet. As shown in Figure 2.22a, the current of self-assembled monolayers (SAMs) was measured between -3 to +3 V under the different polarized directions of the nickel electrode.[64] The high spin selectivity was observed at room temperature, which showed the potential for the spin filter. Huang et al. studied the magneto-optical Kerr effect of the chiral-HOIP/NiFe heterostructures, demonstrating the potential of chiral perovskites for chiral opto-spintronic applications (Figure 2.22b).[65] Additionally, Wang revealed spin-QLEDs with chiral 2D (R/S-MBA) $_2PbI_4$ perovskites as the CISS layer and CdSe/ZnS QDs as emitting layer, which demonstrate a $g_{CP\text{-}EL}$ of 1.6×10^{-2}. The spin lifetime of the carrier affects the value of $g_{CP\text{-}EL}$. Thus, it is critical to improve the spin lifetime to achieve efficient spin-LEDs (Figure 2.22c).[66] As shown in Figure 2.22d, to solve the problems of anisotropic factors, photoresponsivity, and electrical conductivity in CPL detectors, Hao reported a heterojunction device composed of chiral templates

and single-walled carbon nanotubes (SWCNT). This chiral (R-/S-MBA)$_2$CuCl$_4$/SWCNT heterostructure demonstrates a high photoresponsivity (452 A/W), a large anisotropy (0.21) and a low working voltage (0.01).[67]

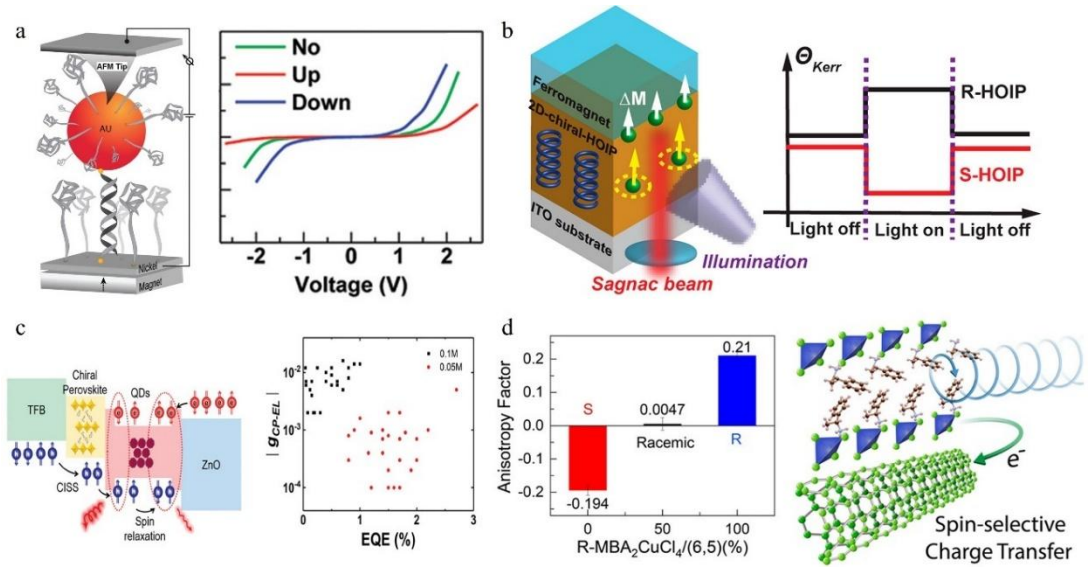

Figure 2.22 (a) Schematic illustration of the experimental setup for spin I-V curves in SAMs of ssDNA and dsDNA device.[64] (b) Diagram of Sagnac MOKE experiment and the Kerr signal under the photoexcitation to identify the CISS effect in the chiral-HOIP/NiFe heterostructures.[65] (c) Energy band alignment and curves of $g_{CP\text{-}EL}$ in the R-/S-MBA$_2$PbI$_4$ based CdSe/ZnS QDs spin-LEDs.[66] (d) Mechanism of the photoexcited electron transportation at the interface of chiral (R-/S-MBA)$_2$CuCl$_4$/SWCNT heterostructure and the measurement of the anisotropy factor in corresponding chiral devices under 405 nm circularly polarized light at V_{DS} = 2V.[67]

(3) Spin Dynamics in Perovskites

Spin dynamics is a fundamental characterization used to study and understand spintronics in perovskite materials, including research on spin relaxation/dephasing, spin transport/diffusion, etc. The ultrafast spectroscopy is one of the important tools to characterize the spin dynamics behaviours. The Rashba effect found in the $CH_3NH_3PbI_3$ perovskites offers the possibility of the application of the spintronics. As shown in Figure 2.23a, the $CH_3NH_3PbI_3$ thin films show a spin lifetime of 7 ps at 75k in electron, which stems from the Elliot-Yafet effect in intraband carrier spin-flip by using circularly polarized (same- and counter-polarized) transient absorption (CPTA) spectra.[68] In 2020, Wang reported a study about the spin relaxation time of quasi-2D perovskites ((PEA)$_2$(MA)$_4$Pb$_5$Br$_{16}$) that shows an extra-long spin lifetime of up to

nanoseconds (Figure 2.23b).[69] In addition, the research about the spin lifetime in RP ($BA_2MA_{n-1}Pb_nI3_{n+1}$) perovskite single crystals (SCs) with different n values (n = 2, 3, 4) and $MAPbI_3$ was reported in 2023. The n value represents the number of PbI_6 octahedral layers in $MAPbI_3$ perovskites (Figure 2.23c).[70] The finding revealed that RP SCs with smaller n values show a longer spin lifetime. However, the recent method of introducing chiral properties into perovskite nanocrystals by chiral molecules provides a new way to study the application of spintronics. Yao et al. fabricated a chiral quasi-2D perovskite LED based on R/S-$NEA_2(FA_{0.85}Cs_{0.15})_2Pb_3Br_{10}$, which achieved long-lived as long as a nanosecond and a record EQE of 13.5% (Figure 2.23d).[71]

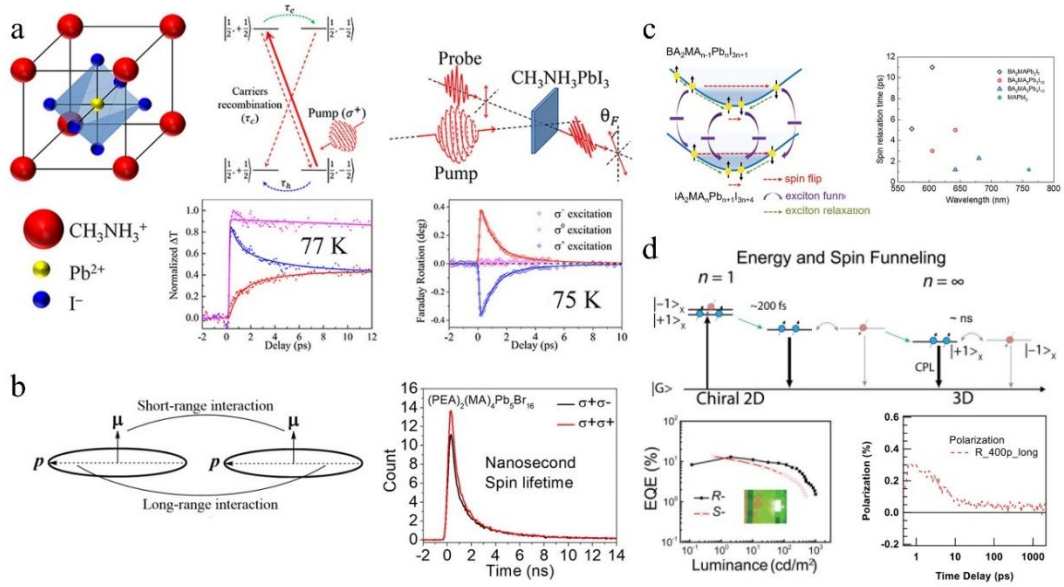

Figure 2.23 (a) Schematic diagram of the band-edge photoexcitation spin dynamics by σ+ photon in $CH_3NH_3PbI_3$ perovskites and the corresponding normalized CPTA spectrum under 19 μJ/cm^2 σ+ pump and σ+/σ- probe at 77 K and 75 K.[68] (b) Illustration of the orbit interaction occurs between polarizations or magnetic dipoles and measurements of the spin lifetime under σ+ (405 nm; 6 μW) excitation in quasi-2D ($(PEA)_2(MA)_4Pb_5Br_{16}$) perovskites.[69] (c) The process of the spin relaxation in excitation and the spin lifetimes of RP ($BA_2MA_{n-1}Pb_nI3_{n+1}$) perovskite SCs .[70] (d) The energy and spin funnelling procedure of chirality-induced exciton polarization and the performance characterize in a chiral quasi-2D R/S-$NEA_2(FA_{0.85}Cs_{0.15})_2Pb_3Br_{10}$ perovskite LED.[71]

2.4.3 Current Challenges for Spintronics in Chiral Perovskite Materials

Although chiral perovskite materials have made amazing progress in spintronics application, giving us a greater understanding of condensed-matter physics, scientists are still lacking studies in material preparation, device optimization, and physics performance testing.

(1) Preparation of the Perovskite materials

Perovskite materials used in spintronics are also limited by two major problems in photovoltaic devices: the toxicity of lead and the stability of the perovskite materials itself. First of all, to solve the toxicity of lead, candidate metal elements that can replace lead can be selected from P-block metals (e.g., Sn, Bi, Ge) and transition metals (e.g., Cu, Mn, Fe).[72] For example, Zhao et al. successfully synthesized 0D tin-based chiral perovskites ((R-/S-MPEA)$_2$SnBr$_6$) with an acentric space group P2$_1$ and achieved the bulk effect second harmonic generation (SHG) response to prove an efficient second-order nonlinear optical (NLO) effect in it (Figure 5.24a).[73] In 2022, Rajput et al. reported a 0D lead-free ((R-/S-MBA)$_4$Bi$_2$I$_{10}$) chiral perovskite derivative. The synthesized chiral perovskite crystals were measured by CD measurements to confirm the chiroptical properties (Figure 5.24b).[74] Secondly, the problem of stability can be referred to as the solution of introducing hydrophobic organic amine molecules to form low-dimensional perovskite structures in solving the stability problem of 3D perovskite photovoltaic devices. Additionally, the substitution of the halide is another efficient method to improve the stability of the chiral perovskite materials. The first 2D chiral perovskite ferromagnets (R-/S-MPEA)$_2$CuCl$_4$ were synthesized in 2020. These 2D hybrid chiral perovskites show an intense CD signal and clear ferromagnetic behaviours (Figure 5.24c).[75] Dehnhardt et al. demonstrated the synthesis of an isomorphous family of compounds [(R)-1-(4-F)PEA]$_4$[E$_2$X$_{10}$] (E=Bi and Sb; X=I, Br and Cl) with different absorption and achieved an efficient SHG, which shows good stability (Figure 5.24d).[76]

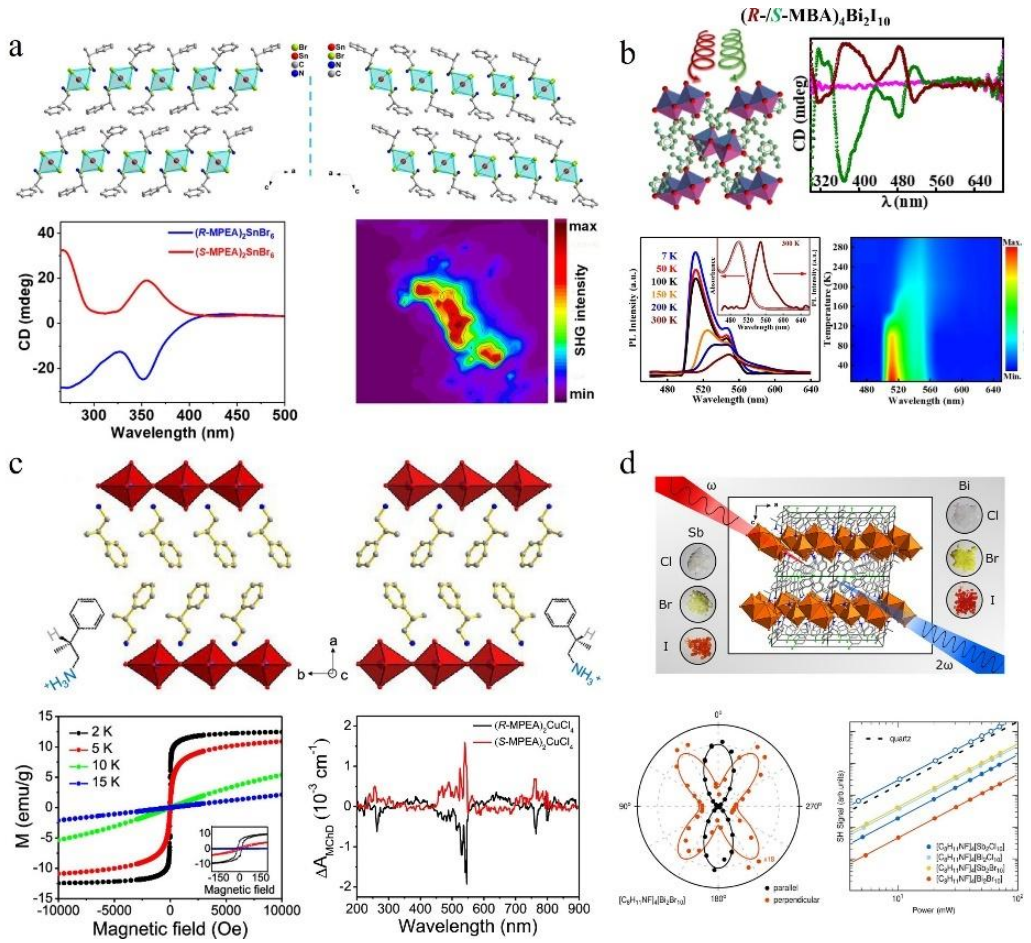

Figure 2.24 (a) Crystal structure of (R-/S-MPEA)$_2$SnBr$_6$ perovskites along the b-axis and the chiral optical feature in it (CD spectra and SHG signals).[73] (b) CD spectrum and temperature-dependent PL spectrum of the chiral 0D lead-free ((R-/S-MBA)$_4$Bi$_2$I$_{10}$) chiral perovskite thin films.[74] (c) Temperature dependence of the magnetic response curves and magneto-chiral dichroism (MChD) measurements in 2D chiral ferromagnets (R-/S-MPEA)$_2$CuCl$_4$ perovskites.[75] (d) Characteristics of the nonlinear optical properties of the chiral lead-free [(R)-1-(4-F)PEA]$_4$[E$_2$X$_{10}$] perovskite materials.[76]

(2) Optimization of the Perovskite devices

Previous studies on the spintronics of perovskite chiral materials mainly focus on the materials themselves, and lack of studies on the spin transport behaviour across the device interface. Scientists have recently invested in research on magnon valves, spin-LED, CPL detectors and so on.[77,78] Based on the research on these spin devices, many efforts can be devoted to optimizing the structure of the devices. For example, the spin-coating process of chiral perovskite films on the substrate can be optimized to obtain a larger chiral signal (CD, CPL, etc.).[79] In Figure 2.25, the intermittent spin-coating

method for chiral perovskite films shows higher CD signals in contrast to the conventional spin-coating method. In addition, the energy level of device can be changed through the optimization of the transmission layer, to improve the spin-related photoelectric performance of the device.

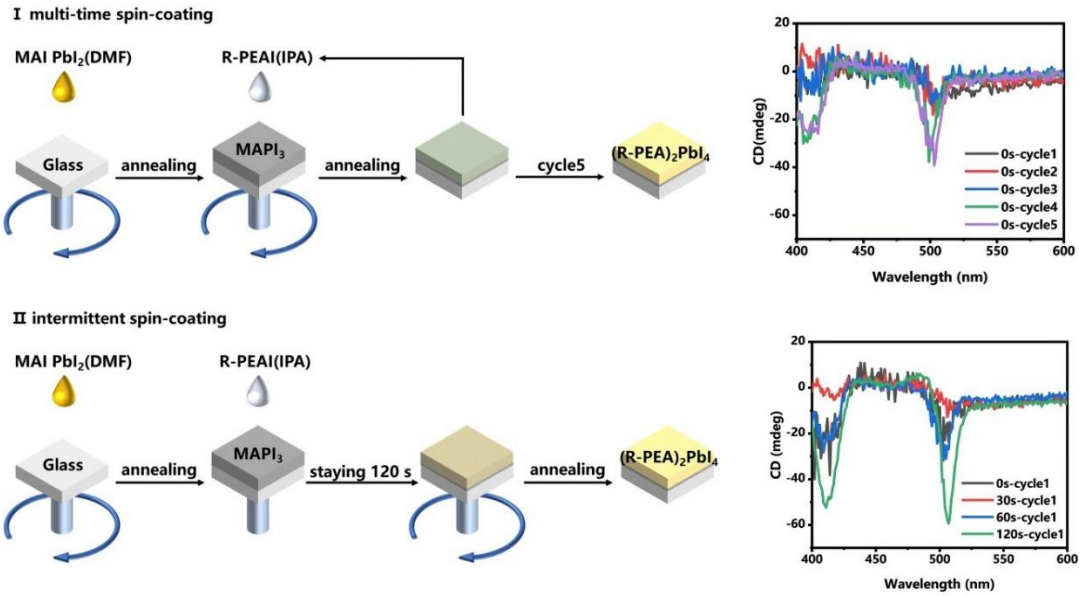

Figure 2.25 Fabrication procedure of the multi-time spin-coating method and intermittent spin-coating method for the chiral perovskite films.[79]

(3) Exploration of the Physics performance

Although some recent breakthroughs have been made in the spintronics of organic and inorganic hybrid perovskite materials, such as spin-optoelectronics phenomena,[58] magnon transport,[80] and so on. But exploring the connection between spintronics and electromagnetic fields, light and heat is also important.

Chapter 3 Experimental Materials, Synthesis and Characterization Methods

3.1 Experimental Materials

Table 3.1 Chemicals and Reagents.

Chemicals	Purity	Company
Cesium carbonate (Cs_2CO_3)	99.95%	Sigma Aldrich
Lead (II) bromide ($PbBr_2$)	99.0%	Sigma Aldrich
Oleic acid (OA)	90%	Sigma Aldrich
Oleylamine (OAm)	80-90%	Aladdin
Toluene	99.85%	Acros
Acetone	99.9%	Sigma Aldrich
Dimethylformamide (DMF)	99.9%	Sigma Aldrich
Hydrobromic acid (HBr)	48%	Sigma Aldrich
Ethanol	Absolute	Uni-Chem
Diethyl ether	99.8%	Sigma Aldrich
Silver chloride (AgCl)	99.5%	Aladdin
Indium chloride ($InCl_3$)	99.99%	Aladdin
Bismuth chloride ($BiCl_3$)	99.99%	Aladdin
1-octadecene (ODE)	> 90%, GC	TCI
Hexane	95%	Sigma Aldrich
(S)- (-)-α-Methylbenzylamine (S-MBA)	99.0%	Sigma-Aldrich

PEDOT: PSS	AI 4083	Heraeus
BCP	99.5%	Xi'an Yuri Solar Co., Ltd
$PC_{61}BM$	99.5%	Xi'an Yuri Solar Co., Ltd
Methyl acetate	99.5%	Aladdin
Hydrochloric acid (HCl)	37%	Sigma-Aldrich

All chemicals were used as received.

3.2 Synthesis of the perovskites

(1) Synthesis of Chiral Ligands (R-/S-MBABr): 5 mL (39 mmol) R-/S-MBA solution was mixed with 15 mL anhydrous ethanol in a 100 mL three-necked round bottom flask placed in an ice bath. 6.6 mL (58 mmol) HBr aqueous solution was added dropwise under vigorous stirring, and the solution remained under stirring overnight. The temperature of the mixture was raised to 70 °C for 30 min to completely evaporate the solvent. The obtained yellowish residue was dissolved in 5 mL of hot ethanol and placed in a freezer for 24 h to induce the recrystallization of R-/S-MBABr. The obtained yellowish crystals were centrifuged down and washed thoroughly with diethyl ether several times until they became colourless; then dried under a vacuum overnight to obtain a white precipitate as the end product. The synthesis of the chiral ligands R-/S-MBACl have the same procedure as above. The chiral ligands (RMBACl and SMBACl) are also synthesized by the same process with the above R-/S-MBABr.

(2) Synthesis of CsPbBr3 NPLs: The synthesis of $CsPbBr_3$ NPLs followed a modified anti-solvent strategy and was performed at room temperature under an ambient environment. Cs-oleate and $PbBr_2$ precursor solutions were prepared as follows: in a 30 mL glass bottle, 65 mg (0.2 mmol) Cs_2CO_3 powder was dissolved in 20 mL OA at 100 ℃; 146.8 mg $PbBr_2$ (0.4 mmol) powder, 40 mL toluene, 100 μL of OA, 100 μL of OAm were mixed in a 50 mL three-necked round bottom flask and heated at 80 °C under a vigorous stirring. Then, different ratios of Cs-oleate and $PbBr_2$ precursors were mixed with 2 mL acetone acting as an anti-solvent to fabricate $CsPbBr_3$ NPLs with the

desired thickness (in monolayer, ML). Specifically, 120 μL Cs-oleate was added to the varying amount of the PbBr2 precursors (as specified in Table S1 for synthesizing 2-5 ML $CsPbBr_3$ NPLs), and after 5 s, 2 mL acetone was added to initiate the growth of $CsPbBr_3$ NPLs. After 60 s, the crude solution was centrifuged at 4000 rpm for 4 min to obtain the NPL product as the precipitate which was redispersed in 1.5 mL toluene.

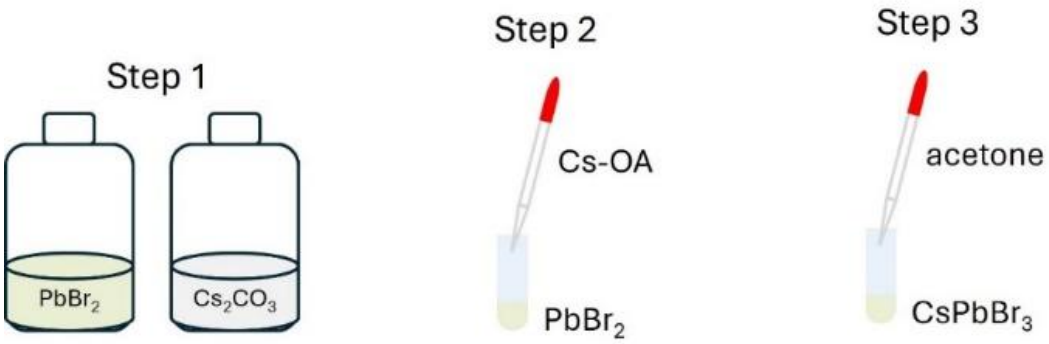

Figure 3.1 Synthesis process of the $CsPbBr_3$ NPLs.

(3) Synthesis of $Cs_2AgIn_XBi_{1-X}Cl_6$ NCs: In a typical reaction, AgCl (86 mg), $InCl_3$ (119 mg), $BiCl_3$ (19 mg), ODE (15 mL), OA (3 mL), OAm (3 mL), and HCl (0.3 mL) were loaded into a 100 mL two-necked flask and heated to 120 °C for 1 h, and then the temperature was raised to 260 °C under N_2 atmosphere, and 2 mL of hot Cs–OA solution was injected quickly under vigorous stirring. Five seconds after the injection, the mixture was cooled down by an ice-water bath. A centrifugation process (10 min at 8000 rpm) was performed to separate the DPNCs from the crude solution. After that, the crude DPNCs were redispersed in hexane and centrifuged again for 10 min at 8000 rpm. Then, the precipitates were discarded, and the supernatant was poured into another centrifuge tube with hexane added, following a centrifugation process for 10 min at 10000 rpm. Finally, the NCs were obtained by discarding the supernatant.

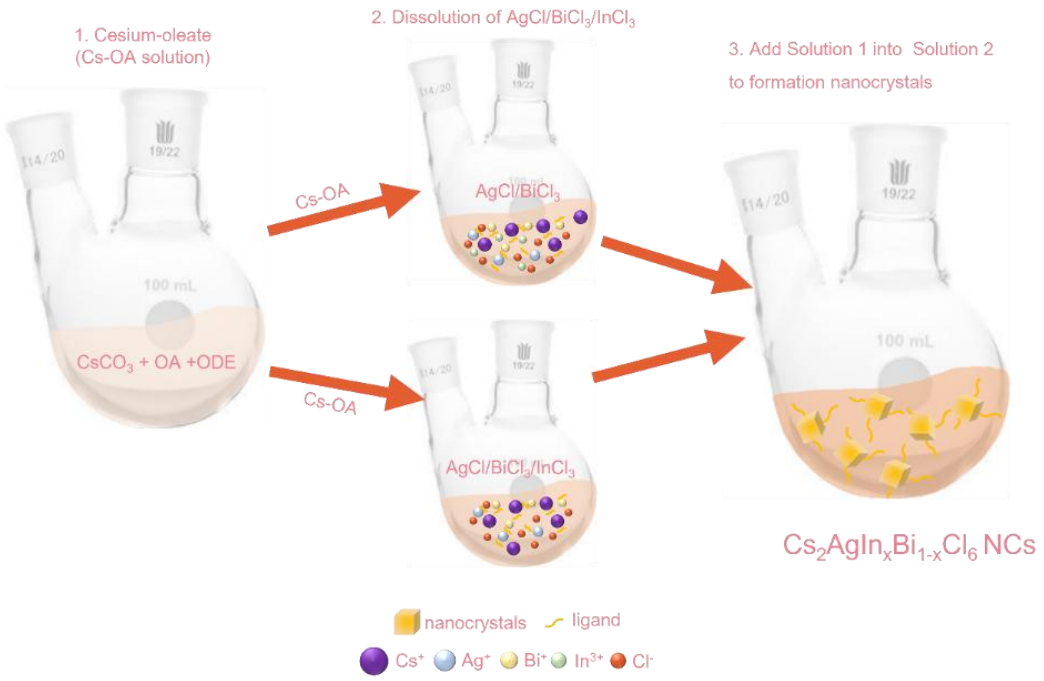

Figure 3.2 Synthesis process of the $Cs_2AgIn_XBi_{1-X}Cl_6$ NCs.

(4) Post-Preparative Treatment of $CsPbBr_3$ NPLs with Chiral Ligands: 244 mg (1.2 mmol) chiral ammonium salts of R-/S-MBABr were dissolved in 1.5 mL solution containing 500 µL DMF, 500 µL toluene, and 500 µL OA, followed by sonication for 1 min and centrifugation at 4000 rpm for 4 min to obtain a clear solution (supernatant). 0.5-5 µL of chiral R-/S-MBABr ligands were added to 1.5 mL of 2-5 ML $CsPbBr_3$ NPLs dispersions, followed by sonication for 1 min and centrifugation at 4000 rpm for 4 min to obtain perovskite NPLs modified with chiral ligands as the supernatant.

(5) Post-treatment of the $Cs_2AgIn_xBi_{1-x}Cl_6$ NCs with RMBA/SMBA ligands: 5 mL of a stock $Cs_2AgIn_xBi_{1-x}Cl_6$ NCs solution was centrifuged for 10 min at 8000 rpm and the $Cs_2AgIn_xBi_{1-x}Cl_6$ NCs supernatant was obtained. The solution of RMBACl and SMBACl in MeOAc was prepared by dissolving 60 mg of RMBACl and SMBACl in 5 mL of MeOAc and stirring 2h at 60 °C. Then, 1 mL of an RMBACl and SMBACl solution was mixed with 5 mL of purified $Cs_2AgIn_xBi_{1-x}Cl_6$ DPNCs, and the mixture was stirred for 30 min at 60 °C and then centrifuged at 8000 rpm for 10 min to collect the $Cs_2AgIn_xBi_{1-x}Cl_6$ NCs supernatant.

(6) Fabrication process of the device based on the $CsPbBr_3$ NPLs

ITO glasses were ultrasonically cleaned by DI water, ethanol and acetone for 15 min each, and then dried in an oven at 120 °C. ITO substrates were treated by UV-ozone

for 20 min before depositing the PEDOT: PSS. The PEDOT: PSS films were spin-coated on the ITO substrates at 5000 rpm for 30 s, and annealing at 150°C for 30 min. Then, the films were transferred into an N_2-filled glovebox. Next, the precursor solution $CsPbBr_3$ NPLs was spin-coated onto the substrate via a one-step process at 2000 rpm for 60 s for several times. A layer of BCP was spin-coated on the $Cs_2AgIn_xBi_{1-x}Cl_6$ NCs layer at 5000 rpm for 30 s. Finally, the device was completed by sequential vacuum deposition of 10 nm Ni under a high-vacuum atmosphere (<10^{-6} Torr). The device area was 0.05 mm^2 by the overlapping area of the ITO and Ni electrodes.

(7) Fabrication process of the device based on the $Cs_2AgIn_xBi_{1-x}Cl_6$ NCs

ITO glasses were ultrasonically cleaned by DI water, ethanol and acetone for 15 min each, and then dried in an oven at 120 °C. ITO substrates were treated by UV-ozone for 20 min before depositing the PEDOT: PSS. The PEDOT: PSS films were spin-coated on the ITO substrates at 5000 rpm for 30 s, and annealing at 150 °C for 30 min. Then, the films were transferred into an N_2-filled glovebox. Next, the precursor solution $Cs_2AgIn_xBi_{1-x}Cl_6$ NCs was spin-coated onto the substrate via a one-step process at 2000 rpm for 60 s for six times. A layer of BCP was spin-coated on the $Cs_2AgIn_xBi_{1-x}Cl_6$ NCs layer at 5000 rpm for 30 s. Finally, the device was completed by sequential vacuum deposition of $Ni_{80}Fe_{20}$, and Au under a high-vacuum atmosphere (<10^{-6} Torr). The thicknesses of $Ni_{80}Fe_{20}$, and Au were 10, and 30 nm, respectively. The device area was 0.02 mm^2 by the overlapping area of the ITO and Au electrodes.

3.3 Characterization Measurements for Perovskites

(1) The UV–vis absorbance spectra (UV-Abs) of the perovskite film were measured using a SHIMADZU UV–vis spectrometer (UV-2550). The UV-2550 double monochromator design provides a high-energy throughput optical system with ultra-low stray light. While featuring low stray light, excellent energy characteristics are provided over an extremely wide wavelength range.

(2) The photoluminescence spectra (PL) were measured using an Edinburgh Photoluminescence FLS 920.

(3) X-ray diffraction characterization was performed by Rigaku SmartLab with monochromatized Cu Kα radiation.

(4) Circular Dichroism spectra were characterized by a CD spectrometer (JASCO J-1500 Easton, MD, USA) at room temperature with a data pitch of 1 nm and a scan rate of 100 nm per minute.

(5) Circularly Polarized Luminescence (CPL) Spectra were measured by the setup we built.

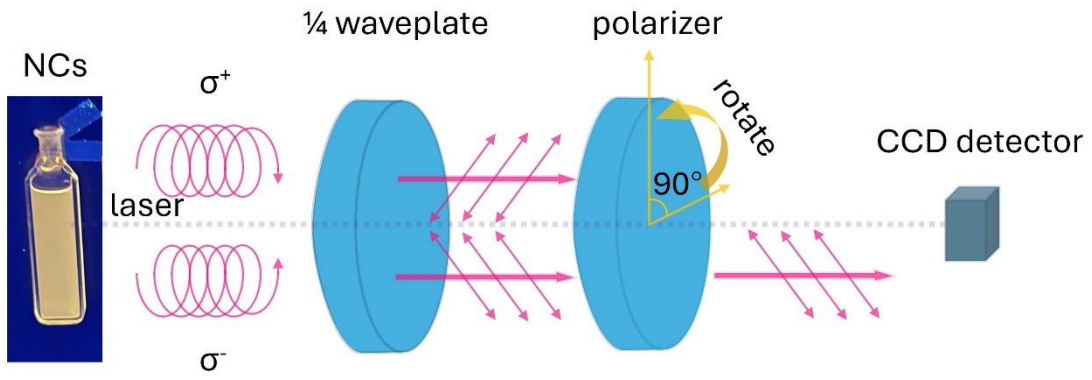

Figure 3.3 The setup of CPL measurements.

(6) Morphologies, crystal structures, and elemental distributions were investigated using a transmission electron microscope (JEOL, JEM-2100F; acceleration voltage, 200 kV) and a double spherical aberration-corrected transmission electron microscope (Thermo Fisher Spectra 300, operated at 300 kV).

(7) Transient absorption (TA) measurements were performed by a femtosecond (fs) pump-probe system (Helios, Ultrafast System LLC) under room temperature conditions. The 340 nm pump pulses (1.91 uJ cm^{-2}) were generated from an optical parametric amplifier (OPerA Solo) that was pumped by a 1-kHz regenerative amplifier (Coherent Legend, 800 nm, 150 fs, 4 mJ). The white-light probe continuum was generated by focusing the fundamental 800 nm beam from Ti: sapphire laser onto a CaF_2 plate. The time delay between the pump and probe pulses was varied by a motorised optical delay line (maximum ≈ 7 ns).

(8) The electrical measurements of the CISS device in chiral nanomaterials were performed by a Lakeshore Cryogenic Probe Station in a vacuum condition (< 10^{-6} Torr). The I-V curves were conducted in a dark environment.

(9) Following the fabrication process the spin PV device was transferred to a room condition for photovoltaic measurements. All measurements were conducted at room

temperature, using 340 nm laser light at an intensity of 86 mW/cm^2. The J–V response was measured by a four-point method using a Keithley 2450 multimeter.

Chapter 4. Long-lived Exciton Spins in Chiral Colloidal Perovskite Quantum Wells at Room Temperature

4.1 Abstract

Achieving long-lived spin orientation at room temperature in the absence of a magnetic field is highly desirable for spintronics applications. Chirality-induced spin selectivity provides a promising approach for efficient spin generation and manipulation. In this study, we investigate the spin generation, dynamics, and transport properties of newly developed colloidal chiral $CsPbBr_3$ perovskite nanoplates (NPLs) with varying well thicknesses. The chiral NPLs exhibit an extended spin depolarization lifetime of approximately 210 ps, which is around one order of magnitude longer than their nanocrystal counterparts. Notably, they also demonstrate high circularly polarized emission (5.0%), spin current polarization up to approximately 43%, and a spin diffusion length reaching 33 nm. Theoretical calculations indicate that the introduction of chiral ligands induces asymmetry in $CsPbBr_3$ nanocrystal platelets (NPLs), creating an additional barrier to spin flipping due to the distinct momentum troughs associated with different spin states. Our findings provide valuable insights into the underlying mechanisms and highlight a novel class of materials with great potential for future spintronic applications.

4.2 Introduction

Spintronics applications in information technology have evolved rapidly since the discovery of giant magnetoresistance.[60] Compared to traditional semiconductor devices that rely on charge-based transport, spintronics offers several advantages, including low power consumption, high-density memory, and fast processing capabilities. In the field of spintronics, a wide range of materials, including organic molecules,[81] and traditional inorganic semiconductors like gallium arsenide (GaAs) or silicon (Si),[82] have been explored for efficient and multifunctional spintronic devices. Recently, metal halide perovskites have gained significant attention due to their potential applications in spin optoelectronics. However, their suitability for most spin-related applications still faces intrinsic limitations, i.e., the short spin coherence time.[83] The presence of defects and strong spin-orbit coupling (SOC) interactions can lead to rapid spin relaxation and dephasing, hindering the efficient manipulation and control of spins.[84]

In the low-dimensional system, the strong confinement leads to atomic-like energy levels with large interlevel spacings which could couple very weakly to phonons (phonon bottleneck), and hence, spin relaxation by phonon scattering could be suppressed and the spin lifetime can be prolonged. However, to date, experimental studies reported short spin relaxation lifetimes in quantum-confined perovskites, typically ranging from femtoseconds to picoseconds at room temperature, which is much shorter than those of conventional II-V GaAs semiconductors.[85-89] The exciton spin relaxation is reported on the time scale of 1.9 ~ 3.9 ps at room temperature for $CsPbI_3$ and $CsPbBr_3$ perovskite QDs, which varies with the size of the quantum dots.[87] Todd et al. reported an extended spin-relaxation time ∼of 10 ps in butylamine-based 2D perovskites (n = 3) and proposed a D'yakonov−Perel (DP) spin-relaxation pathway. Matthew C. Beard et al. discovered exciton-spin relaxation times of EOA_2PbI_4 (EOA = ethanolamine) up to ∼26 ps at low excitation densities and at room temperature. Despite these achievements, the spin lifetime is still much shorter than that of conventional III-V GaAs semiconductors (typically 1-30 ns),[90] limiting their applications.[91] The primary proposed mechanism that governs the short exciton spin relaxations in low dimensional perovskites is the strong spin−orbit interaction at low excitation fluence (D'yakonov−Perel (DP) mechanism) and exciton exchange interaction at high excitation fluence (BAP mechanism).[85] The strategy to slow down the spin lifetime in perovskites is thus highly desired. Chiral halide perovskites refer to a class of perovskite materials that exhibit chirality.[92] The flexibility nature of halide perovskite allows the incorporation of chiral organic molecules into the perovskite lattice, creating chiral semiconductors with a high degree of circularly polarised photoluminescence (CPL) and CD.[93, 94] In general, the chiral-induced spin selectivity effect would produce spin-polarized electrons without the need for magnetic materials.[95] It also provides a fundamentally different approach to spintronic materials and enables a range of interesting devices with novel functionalities, such as spin valve devices, spin photovoltaics (solar cells),[96] spin light emitting diodes/lasers, [54, 92, 97] and circular polarization light detection.[54, 55] By carefully designing the ligands and controlling the crystal structure of chiral halide perovskites, it is possible for low-dimensional chiral perovskites to exhibit a high degree of spin polarization and long depolarization time and create spintronic devices.[98]

In this work, we achieve slow spin relaxation dynamics in the n = 2-5 chiral $CsPbBr_3$ monolayer (ML) using circular polarized transient absorption spectroscopy. The layered $CsPbBr_3$ NPLs show an increasing spin relaxation lifetime with increasing NPLs layers, which is a result of the Rashba splitting and phonon scattering effect in these quantum-confined nanostructures. In the $CsPbBr_3$ NPLs treated with chiral organic molecule R-α-methylbenzylamine (R-MBA), we achieved a degree of polarization of P_{CPL} = 5.0%, the discovery of spin depolarization lifetimes up to hundreds of picoseconds and spin diffusion length ~ 33 nm has led to promising applications of chiral perovskite nanostructures in spintronic devices. We used chiral-induced spin selectivity (CISS) to produce spin-polarized carriers with spin polarization value P ~ 43% at room temperature without magnetic fields or ferromagnetic contact. The chiral ligands would change the environment of spin-orbit coupling, induce the breaking of symmetry in NPLs, and thus creates an additional barrier to spin flipping because the spin states are in different momentum valley.

4.3 Result and Discussion

Transmission electron microscope (TEM) images evidenced the NPLs morphology as shown in Figure 4.1. It can be seen that the thickness of the $CsPbBr_3$ NPLs increases with the increasing of the layers $CsPbBr_3$ monolayer and the lateral size of the $CsPbBr_3$ NPLs is barely constant. Additionally, the shape of the $CsPbBr_3$ NPLs in TEM images also show a high crystallization.

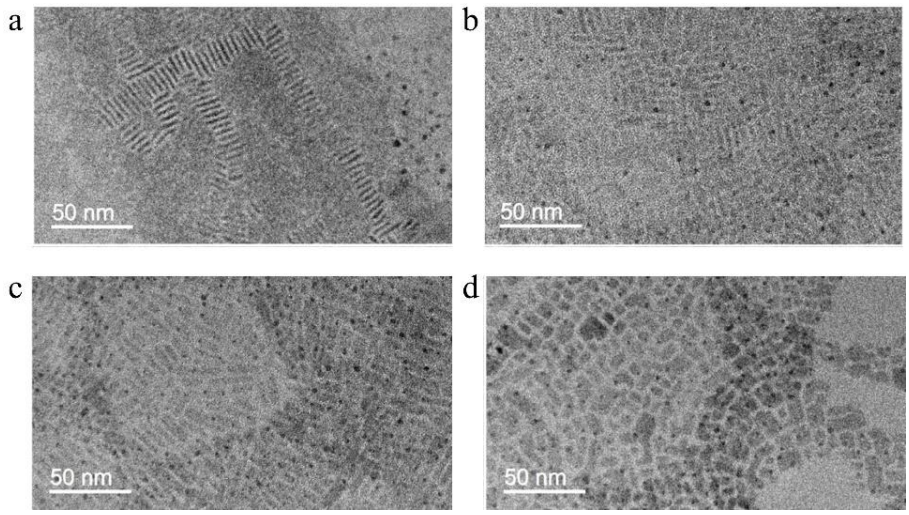

Figure 4.1 Transmission electron microscope (TEM) images for 2-5 ML $CsPbBr_3$ NPLs, respectively.

Figure 4.2a shows the linear UV-vis absorption of 2 to 5 MLs $CsPbBr_3$. All the NPLs show obvious absorption onset, the excitonic absorption peak is around 2.90, 2.71, 2.66, and 2.57 eV, respectively. Each photoluminescence spectrum (Figure 4.2b) comprises only one single peak close to the excitonic absorption peak. Similarly, the sharp excitonic absorption peaks and small Stokes shifts indicate the good-sized monodispersity of NPLs. Here, a blue shift in the absorption and PL spectra with a decreasing number of layers $CsPbBr_3$ stems from the quantum confinement effect. Absorption spectra are fitted with a 2D quantum-well absorption model, yielding an exciton binding energy of 302, 278, 179, and 150 meV for 2-5ML $CsPbBr_3$ nanoplatelets, respectively. (Table 4.1).

Table 4.1 Fitting parameters of absorption spectra in Figure 4.2a.

	E_0/eV	E_b/eV	η/eV	r/eV	r_c/eV	A_c/eV
2ML	2.868	0.302	0.0620	0.0392	0.329	5.12
3ML	2.693	0.278	0.0525	0.0558	0.291	10.78
4ML	2.640	0.179	0.0104	0.0762	0.287	13.71
5ML	2.593	0.150	0.0318	0.0874	0.163	8.77

Note:

The exciton binding energy was determined by fitting the extinction spectrum with a quantum-well absorption model.

$$p(E) = p_x + \frac{A_c}{2}\left[\mathrm{erf}\left(\frac{(E-E_0)-E_b}{r_c}\right) + 1\right] \quad \text{Equation 4.1}$$

$$p_x = \frac{1}{2\eta}\left[\mathrm{erf}\left(\frac{(E-E_0)}{r_c} - \frac{r}{2\eta}\right) + 1\right] \exp\left(\frac{r^2}{4\eta^2} - \frac{(E-E_0)}{\eta}\right) \quad \text{Equation 4.2}$$

Here p_x is the absorption line shape for a quantum-well exciton with asymmetric broadening η. E_0 and E_b are the absolute exciton energy and binding energy, respectively. r is the line width of the absorption peak. A_c and r_c are the step height and width of the continuum edge.

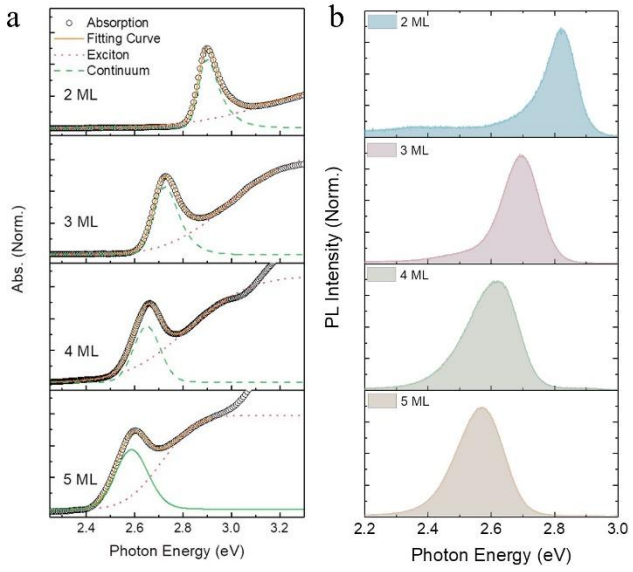

Figure 4.2 (a) The normalized absorption spectra for $CsPbBr_3$ layered nanoplatelets. The exciton and continuum edge contribution fitting for absorption spectra of 2ML, 3ML, 4ML, and 5ML $CsPbBr_3$ nanoplatelets, respectively. Absorption data (open circle) are fitted with a quantum well absorption model (full line), yielding an exciton binding energy of 302, 278, 179, and 150 meV for 2ML, 3ML, 4ML, and 5ML $CsPbBr_3$ nanoplatelets, respectively. (b) Photoluminescence spectra for $CsPbBr_3$ monolayers.

To understand the principle of the spin-flip mechanism and quantify the exciton spin relaxation lifetime in $CsPbBr_3$ NPLs, we then conducted the circularly polarized (same- and counter-polarized) transient absorption experiment on all the NPLs. According to the well-established quantum states in halide perovskites, the top of the valence band is a doubly degenerate state with total angular momentum quantum number J = 1/2 and angular momentum $m_j = \pm 1/2$. Since the presence of SOC, the conduction band edge is also a doubly degenerate state with J = 1/2 and $m_j = \pm 1/2$.

In circularly polarized TA configuration, for example, the σ+ photon pumps the transition from VB to CB state and exclusively stimulates carriers/excitons carrying angular momentum of $m_j = +1$. Such change of $m_j = +1$ state can only be detected by a σ^+ probe photon but not a σ^- probe photon before carriers/excitons spin flip; in this situation, carriers/excitons spin-flip (the spin depolarization of corresponding states) causes the decay of signal (namely measured by the same polarized configuration). On the other hand, the σ- probe can monitor the change of J = +1/2 state (decay signal of carriers' exciton) and the formation of the state with J = -1/2, i.e., measured by the

counter-circularly (CC) polarized pump/probe case (see Figure 4.3a). It is worth mentioning that the circularly polarized TA measurement used here does not measure the spin flipping of electrons and holes, but the overall exciton spin flipping time.

To get rid of the influence from interlevel spin relaxation, we select pump photon in resonance with the band edge transition for each $CsPbBr_3$ NPL sample. The excitation photon energy is 2.90 eV for n = 2, 2.71 eV for n = 3, 2.66 eV for n = 4, and 2.57 eV for n = 5. Additionally, the experiments were performed under low pump fluence to make sure the perovskite in the ensemble was excited with only one exciton or less. The circular polarized transient absorption spectra of $CsPbBr_3$ NPLs and their TA kinetics probed at band-edge photobleaching from the co- and counter-polarized pump-probe experimental results can be found in Figure 4.3b. To quantitatively determine the spin coherence time, we plot the population kinetics of the difference between $\sigma+$ and $\sigma-$ bleach signals for n = 2, 3, 4, and 5 monolayers (in Figure 4.3c). The difference kinetic curves can be generally fitted with a mono-exponential decay model, the dashed line indicates the fitting line. The spin coherence time shortens from 1.14 ps in n = 5 monolayer to ~ 0.24 ps in n = 2 monolayer; the characteristic spin coherence time is 0.26 ps for n = 5 monolayer, and is 0.95 ps for n = 5 monolayer, respectively. The spin relaxation rate $K_{spin} = 1/\tau_{spin}$ is plotted against the exciton binding energy for 2-5 ML $CsPbBr_3$ nanoplatelets as shown in Figure 4.3d.

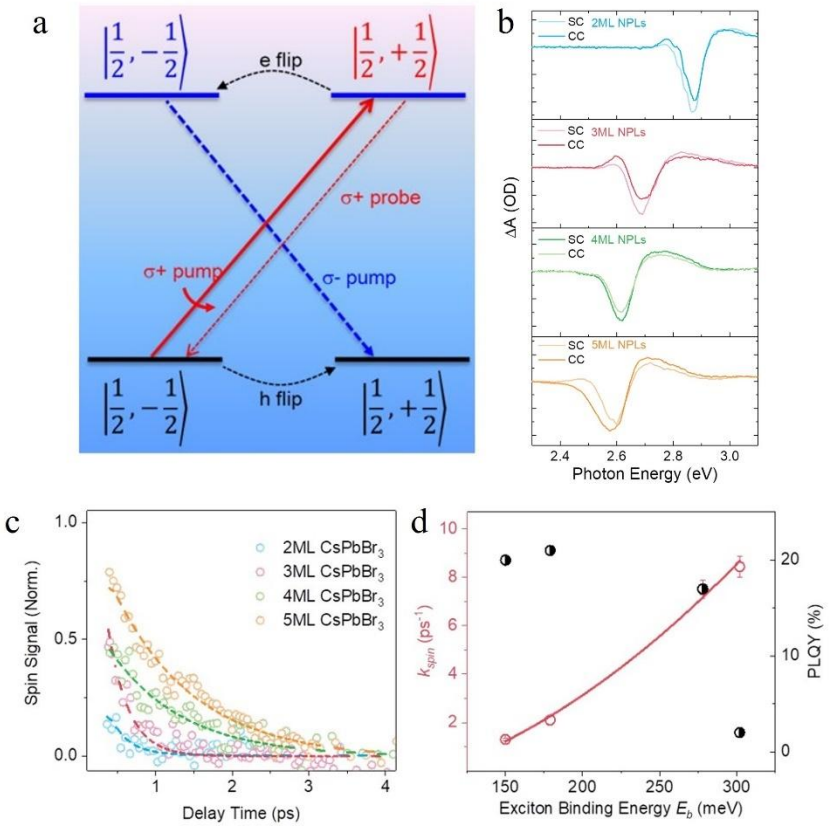

Figure 4.3 (a) Principle of spin relaxation measurements in $CsPbBr_3$ NPLs using circularly polarized TA. (b) Transient circular polarized transmission spectra of layered $CsPbBr_3$ nanoplatelets, pumped at band-edge of same and counter circularly polarized pump and probe at 1 ps delay for the number of layer n = 2−5. (c) The dynamics of spin coherence are plotted as the net spin signal for n = 2-5 perovskite NPLs, the dashed line represents the single exponential fit to the spin coherence dynamics. (d) Extracted spin relaxation time as a function of the number of perovskite layers.

In general, three spin-relaxing mechanisms are thought to be involved in perovskite semiconductors: the Elliott-Yafet (EY), D'yakonov-Perel (D-P), and Bir-Aronov-Pikus (BAP) mechanisms.[83] In most of the iodine-based halide 3D perovskites, i.e. $MAPbI_3$ or $CsPbI_3$ (bulk or nanocrystals), their spin relaxation process is dominated by the phonon scattering process (E-Y mechanism).[84, 86] For the non-centrosymmetric-quantum-well structures (2D halide perovskite) or Br-based perovskites ($MAPbBr_3$ or $CsPbBr_3$), the dominant spin relaxation can be described by D'yakonov-Perel (D-P) mechanism, where carrier spin relax through spin-orbit coupling.[84, 85, 89, 99] In the D-P spin relaxation mechanism, the spin-coupling and symmetry breaking will induce the creation of a local pseudo-magnetic field.

In a word, there are several mechanisms of spin relaxation, most involving spin-orbit coupling to provide the spin-dependent potential, in combination with momentum scattering to provide a randomizing force.[83]The Rashba splitting is a result of the breaking of inversion symmetry and spin-orbit coupling in semiconductors. When reducing the dimensionality, for the instance of 2D layered quantum well structures, the breaking of symmetry becomes more noticeable and thus induces stronger Rashba splitting. A larger Rashba splitting is likely responsible for the lengthened spin coherence lifetime in many semiconductor systems.[88] As a counteracting factor, phonon scattering, can faster spin depolarization. Assuming the spin-flip probability due to momentum scattering during thermalization to be α, the observable spin polarization is given by:[85]

$$P = P_0 e^{-\alpha \Delta E} \qquad \text{Equation 4.3}$$

Here, P_0 is the photoexcited spin polarization and $\Delta E = E_{pump} - E_{probe}$ is the energy difference between the pumping and the probing state (band edge), i.e., energy loss due to thermalization (hot carrier cooling process). The momentum scatterings (i.e., with carriers, impurities, or longitudinal optical phonons) inevitably cause the loss of spin information, typically via the Elliot-Yafet mechanism at a rate proportional to the momentum-scattering rate. [83, 85, 100]

We first analyzed the relationship between the exciton binding energy and the spin relaxation rate ($1/2\tau_{spin}$) in these NPLs according to the D-P mechanism, where the relaxation rate shows a quadratic dependence ($1/2\tau_{spin} \sim a + bE_b^2$) on exciton binding energy. In Figure 4.3d, the relaxation rate enhances monotonically with increasing binding energy and can be well-fitted with the quadratic equation. However, the largest Rashba splitting energy in 2ML $CsPbBr_3$ NPLs (obtained from theoretical results, see detail in Figure 4.4) would possess the longest spin coherence lifetime, which is in stark contrast with the trend in our experimental results. In particular, for 2ML $CsPbBr_3$ NPLs, the slight difference between the co- and counter-circularly polarized TA spectra is accompanied by a fast spin relaxation time and a much higher exciton binding energy, suggesting that trap states or strong phonon scattering play a role in the spin relaxation. Previous studies have shown that phonon scattering rates are directly related to the strength of electron-phonon coupling.[101]

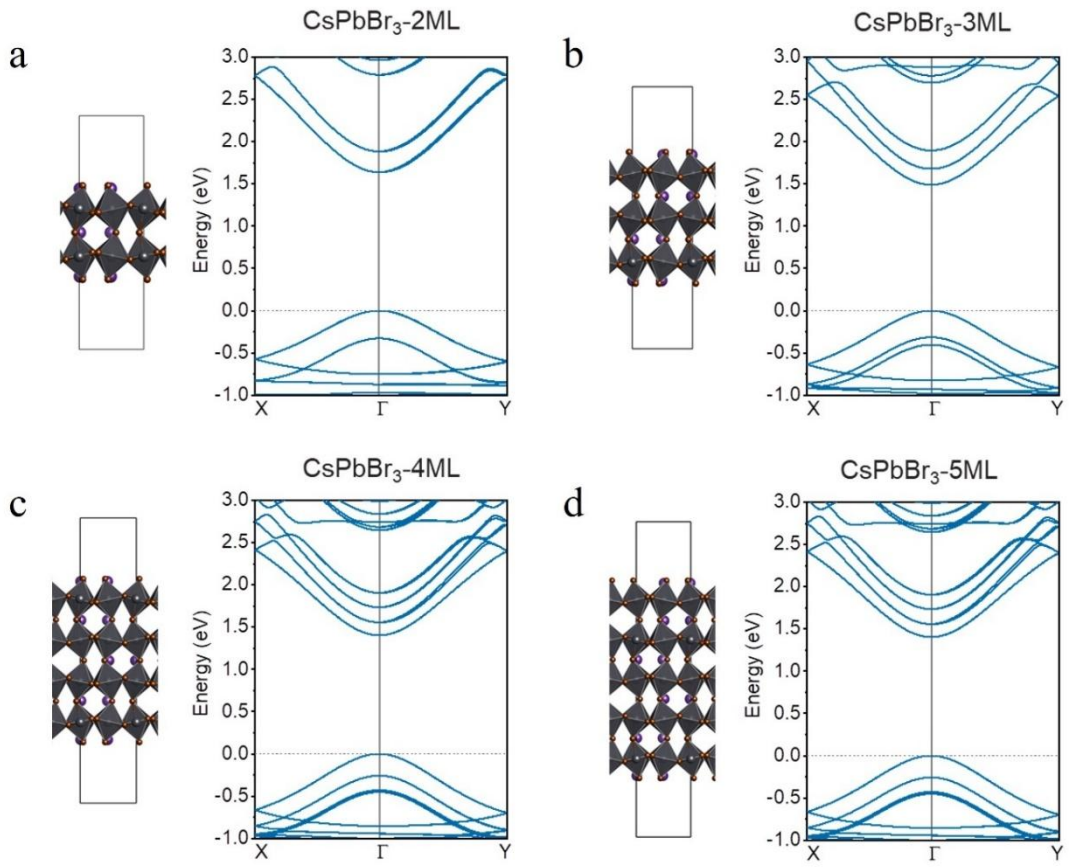

Figure 4.4 Optimized crystal structures and electronic bands for Cs-$CsPbBr_3$ with (a) 2ML, (b) 3ML, (c) 4ML, and (d) 5ML, as calculated at GGA/PBE+SOC level of theory.

Based on our temperature dependent on PL line width experimental results (see Figure 4.5), we find that both exciton-phonon coupling strength Γ_{LO} (meV) and optical phonon energy E_{LO} in 2ML are much larger than that of in 5ML $CsPbBr_3$ NPLs, indicating decreased electron-phonon coupling for increasing n number, which is consistent with other 2D perovskite systems. With an increased rate of phonon scattering for the smaller number of layers, spins depolarize faster. The observed trend in spin coherence lifetime is quite similar to the previous reports, which is a result of the trade-off between Rashba splitting and phonon scattering.[84, 88, 102] The interplay between these two factors gives the longest spin relaxation lifetime in the 5ML $CsPbBr_3$ NPLs.

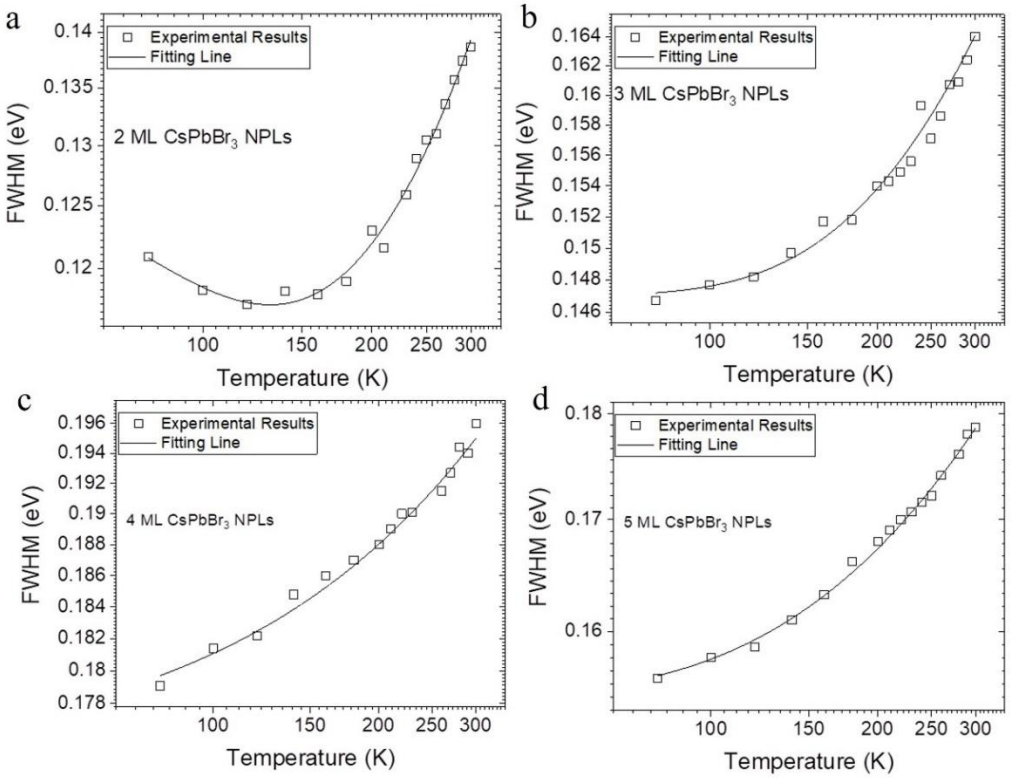

Figure 4.5 Temperature-dependent photoluminescence line width of (a) 2ML $CsPbBr_3$ NPLs, (b) 2ML $CsPbBr_3$ NPLs, (c) 2ML $CsPbBr_3$ NPLs, and (d) 2ML $CsPbBr_3$ NPLs.

The organic-inorganic nature of chiral halide perovskites allows for the incorporation of organic ligands with tunable properties, which is possible to enhance their spin-dependent properties. Herein, we treated the $CsPbBr_3$ NPLs with R-α-methylbenzylamine (R-MBA) and S-α-methylbenzylamine (S-MBA) ligands. The exciton absorption peaks of 2-5 ML NPLs showed a slight shift after R-MBA treatment as compared to the untreated NPLs in. We used the electronic circular dichroism spectra to study the chiroptical activity of R-MBA/ S-MBA treated perovskite NPLs. The significant bisignate peak overlaps with the maximum exciton absorption for 2ML and 3ML NPLs samples, which can be generally assigned to the electronic coupling interaction between the chiral shell and the nanoplates (Figure 4.6a and b). With increasing NPL thickness, bisignate CD peaks corresponding to lower and higher excitonic transitions of NPLs follow a similar redshift.[103] All the peaks in the CD spectra appear to be at the same wavelengths for (R- and S-MBA treated NPLs) films but with opposite signals (Figure 4.6). The incorporation of chiral organic amines leads to optical chirality in the inorganic Pb-I framework.[104]

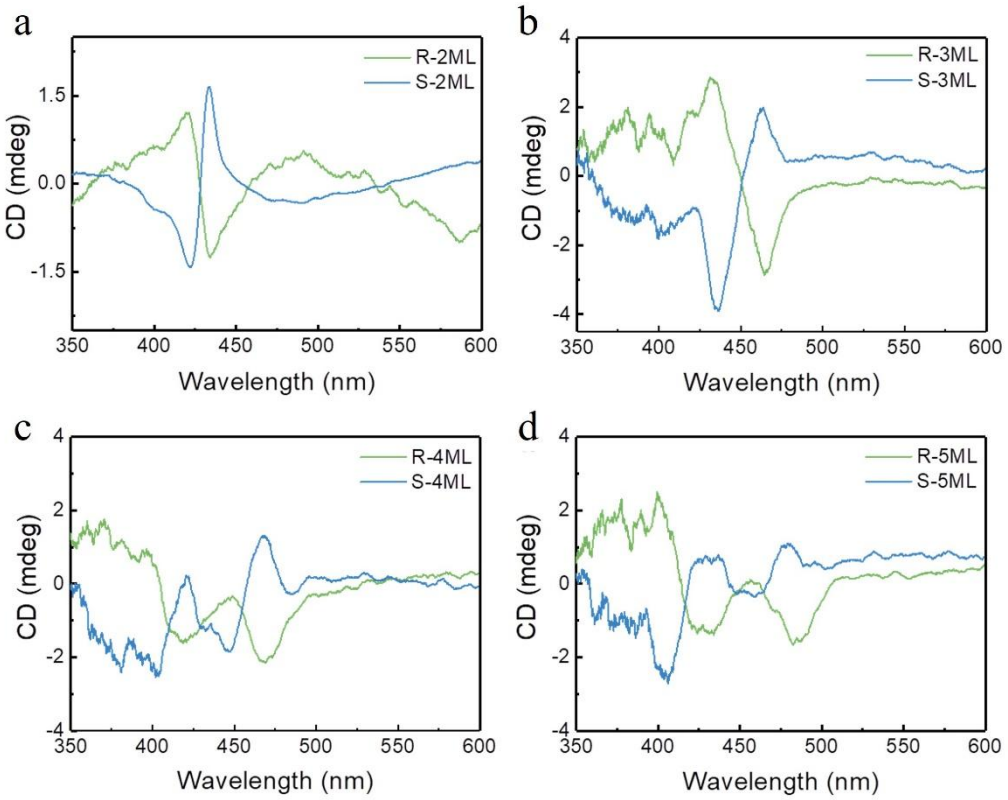

Figure 4.6 Circular dichroism spectra of R-MBA and S-MBA treated 2-5 ML $CsPbBr_3$ NPLs.

To further understand the polarization dynamics in these chiral ligands treated $CsPbBr_3$ NPLs. We conducted the TA spectra with a linear polarization pump and circular polarization probe configuration. As shown in Figure 4.7d, the TA signals for both right-handed and left-handed polarized probes have similar photobleaching features with long decay lifetimes beyond 3 ns in R-5ML $CsPbBr_3$ NPLs. For the probes with different polarization directions, we observed an energetic splitting (~18.6 meV for the exciton bleaching peak) between the two spectra starting from time zero in R-5ML NPLs. The energetic splitting ~ 5.3 meV becomes smaller in R-4ML NPLs (Figure 4.7c). In contrast to the chiral R-5ML and R-4ML with clear spin splitting, the TA spectra with right-handed and left-handed polarized probes overlap with each other at all delay times for the R-3ML samples (see Figure 4.7b). According to the previous reports,[105] the energy splitting detected by this linearly polarized pump and circularly polarized probe configuration is attributable to the intrinsic chiral character of the sample, which differs from the experimental results obtained from co- and counter-circularly polarized pump-probe spectra. The difference in energy splitting of TA signals indicates that intrinsic chirality of perovskite can be modified by the chiral ligands. In Figure 4.7h,

the R-5ML exhibits different decay kinetics for σ+ and σ− probes. The degree of polarization for σ+ and σ− probe starts from 0% at time zero and increases to the maximum positive value of ~ 0.05 during the initial 1 ps, after which it decays to 0 at ~ 1000 ps. In comparison with R-5ML, the R-MBA treated 2-4ML NPLs show a shorter polarization relaxation lifetime, which depends on the layers of NPLs (see Figure 4.7e-g).

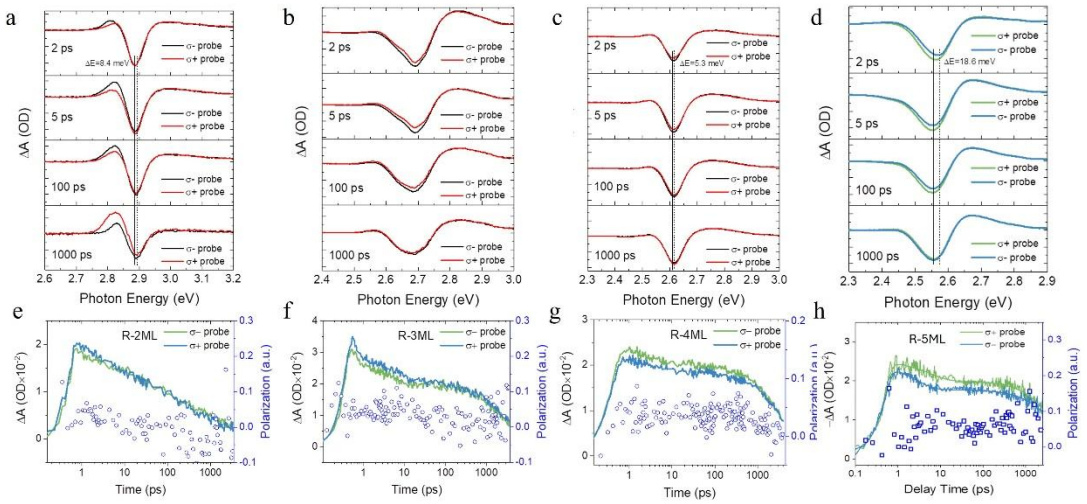

Figure 4.7 Evolution of circularly polarized TA spectra of (a) R-MBA treated 2ML $CsPbBr_3$ NPLs, (b) R-MBA treated 3ML $CsPbBr_3$ NPLs, (c) R-MBA treated 4ML $CsPbBr_3$ NPLs and (d) R-MBA treated 5ML $CsPbBr_3$ NPLs with a linear pump and circularly polarized probe; (e) Comparison of TA kinetics with linear pump and circularly polarized probes showing net circular polarization in (e) R-MBA treated 2ML $CsPbBr_3$ NPLs, (f) R-MBA treated 3ML $CsPbBr_3$ NPLs, (g) R-MBA treated 4ML $CsPbBr_3$ NPLs and (h) R-MBA treated 5ML $CsPbBr_3$ NPLs.

To characterize the spin-split states in R-MBA treated $CsPbBr_3$ NPLs, we conducted the co- and counter-circularly polarized pump-probe configurations, with σ+ excitation light. A clear intensity difference is observed when probing R-MBA treated $CsPbBr_3$ NPLs with σ+ and σ- photons. Compared to the CC pump-probe configuration, the TA signals at the PB region with the SC pump-probe configuration always show higher intensities, such observations are similar to those of untreated $CsPbBr_3$ NPLs. Figure 4.8a shows the 2D colour plot of the net spin signal with σ+ photon excitation of 5ML chiral $CsPbBr_3$. We then extracted the spin coherence lifetime from the net spin TA kinetic that probed at bleach signals (in Figure 4.8b). The net spin TA kinetics, i.e., the difference between the σ+ and σ- bleach signals, were fitted with a bi-exponential decay

model, which yielded a fast exciton spin relaxation time of about 1.28 ps and a long spin relaxation time of about 210 ps. Figure 4.8c demonstrates the spin coherence lifetime versus the number of monolayers. In all chiral $CsPbBr_3$ MLs, an additional long spin relaxation process is found, which may arise from the coupling interaction between the chiral ligand and the $CsPbBr_3$ lattice. The fast exciton spin relaxation time is estimated to be ~ 0.24, 0.26, and 1.01 for n = 2-4 $CsPbBr_3$ MLs, respectively. The spin relaxation time also shows a monotonically increasing trend with the increasing number of layers of NPLs, i.e., the exciton binding energy. We then performed circularly polarized PL measurements at room temperature on $CsPbBr_3$ monolayers. The calculated P_{CPL} of 5ML chiral $CsPbBr_3$ at room temperature is 5.0% (Figure 4.8d), which is comparable with previously reported values for the chiral $FAPbBr_3$ NCs.[98] In contrast, archiral $CsPbBr_3$ monolayers show no detectable difference in PL intensity between right-handed and left-handed detection channels. In Figure 4.8e, we collected TA spectra from 5ML chiral $CsPbBr_3$ NPLs with four polarized pump-probe configurations probed at 2 ps delay time. Following excitation with σ+ or σ− photons, a clear intensity difference is observed in the PB and PIA regions when probing 5ML chiral $CsPbBr_3$ NPLs with σ+ and σ− photons. In chiral ligand-treated perovskite, we interpret the difference in spin relaxation kinetics as further evidence for a spin-related contribution to the chirality polarization.

We then compare the exciton depolarization dynamics in R-MBA treated and untreated NPLs. The polarization can be described by the equation as follow:

$$P(t) = \frac{\Delta A_{counter} - \Delta A_{co}}{\Delta A_{counter} + \Delta A_{co}} \qquad \text{Equation 4.4}$$

where ΔA_{co} and $\Delta A_{counter}$ are the TA signals with the same or opposite pump−probe circular polarization, respectively. Figure 4.8f shows the exciton depolarization dynamics of 5ML and R-MBA treated 5ML NPLs, respectively. The degree polarization of 5ML NPLs starts from a value of ~0.6 and then decays rapidly over the 3ps to 0. In turn to the polarization of R-MBA treated 5ML NPLs, when excitation with σ+ photons, the spin polarization degrees of NPLs increase to a maximum value of ~ 0.6 during the first 1 ps and experience a fast decay during the first 10 ps, which is limited by the short exciton spin lifetime. A long depolarization time of up to hundreds ps can be found, and the degree of polarization stabilizes at ~0.2, demonstrating that chiral ligand-treated NPLs inherently have a larger polarization degree at a long delay time and a long

polarization relaxation lifetime close to 1 ns. While following excitation with σ- photons, the polarization degree with a maximum positive value of ~ 0.3 decays to ~ 0.03 at 2 ps, it then decays to 0 with the depolarization time closed to ~ 100 ps. In the chiral perovskites, it was reported that the chiral crystal structures would first provide an initial polarized state, and the angular momentum orientations of polarized excitons would also be preserved, resulting in a longer spin relaxation time in the nanosecond time range.[88, 105] Here, we surmise that the introduction of R-α-methylbenzylamine as chiral ligands would change the environment of spin-orbit coupling, leading to symmetry breaking in NPLs and creating an extra barrier to spin flipping due to the spin states being in different momentum valleys.

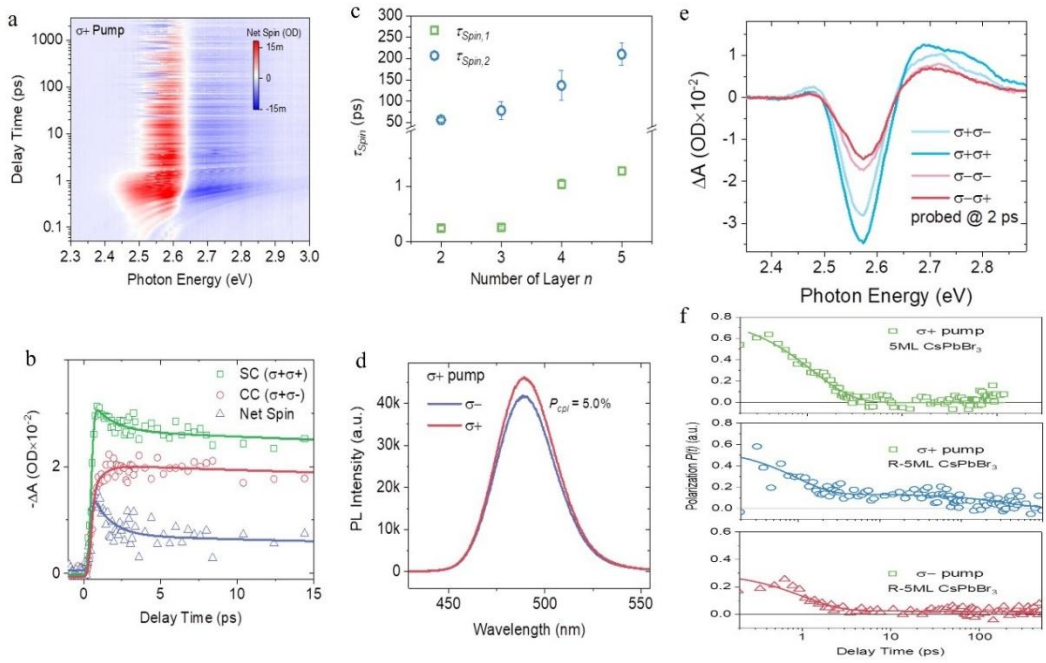

Figure 4.8 Chirality-induced spin selectivity (CISS) spin relaxation (a) 2D color plot of net spin signal in 5ML chiral $CsPbBr_3$, the transient circular polarized absorption spectra were obtained from same and counter circularly-polarized pump and probe configuration; (b) Transient co- and counter-circular polarized pump-probe kinetics with their difference of R-5ML $CsPbBr_3$ NPLs, pumped at band-edge of same (σ+σ+) and counter (σ+σ-) circularly polarized pump and probe; (c) Extracted spin relaxation time as a function of monolayer number in RMBA treated perovskite; (d) Circularly polarized photoluminescence of 5ML chiral $CsPbBr_3$ with σ+ light excitation; (e) The extracted exciton depolarization dynamics for archiral and chiral 5ML $CsPbBr_3$ nanoplatelets, respectively.

Figure 4.9a summarizes the spin relaxation lifetime of low-dimensional semiconductors reported in previous literature.[84, 88, 89, 98, 106] The $CsPbBr_3$ monolayers reported in this study exhibit an exceptional spin coherence time. Figure 4.9b displays the average degree of polarization P_{CPL} in CPL for chiral $CsPbBr_3$ monolayers with n = 2-5. The steady-state degree of spin polarization is generally determined by the balance between spin excitation and decay. In this case, we calculated the degree of polarisation P_{cal} using the equation provided: $P_{cal} = \frac{P_0}{1+\frac{\tau}{\tau_s}}$, where P_0 is the initial polarization ratio after excitation, which for pristine perovskite can be 100%. τ is the recombination time of photoexcitations, and τ_s is the spin relaxation time.[83] Here, the long spin lifetime value is selected as τ_s to calculate the P_{cal} value. In Figure 4.9b, it shows that P_{cal} is close in value to P_{CPL}, indicating that the majority of P_{CPL} comes from the chiral ligand-induced long spin depolarization. The spin diffusion length is an important quantity for spintronics. In $CsPbBr_3$ NCs, excitons occupy individual NCs and can hop between nearest neighbour NCs. Exciton transport in semiconductor NC solid is understood in the framework of incoherent hopping mediated through dipole-dipole interactions. The spin diffusion length was calculated according to exciton hoping mode[107]:$L_s = \sqrt{D_s \tau_s}$, τ_s is the spin relaxation lifetime, the spin diffusion coefficient D_s can be expressed as $D_s = D_{hop} + D_{exc}$; includes charge/spin hopping (D_{hop}) and exchange-mediated coupling between spins on adjacent molecules (D_{exc}). Based on previous reports, exciton diffusivity was measured to be around 0.01-0.5 cm s^{-1}. The spin diffusion length L_S for archiral and chiral $CsPbBr_3$ monolayers are compared in Figure 4.9c.

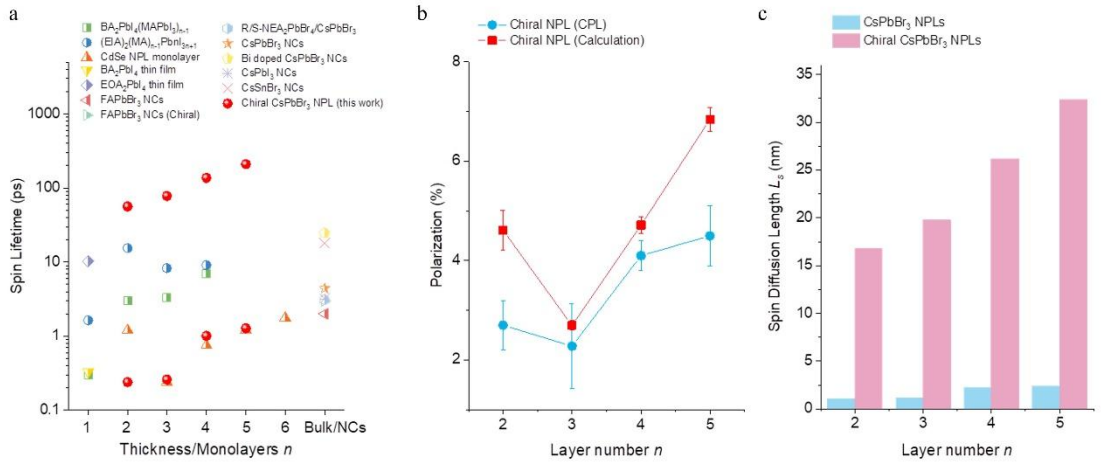

Figure 4.9 (a) Comparison of the room temperature spin relaxation lifetime of chiral perovskite NPLs with the low dimensional semiconductors reported in the literature. (b) The degree of polarization in CPL for chiral $CsPbBr_3$ nanoplatelets, respectively. P_{cpl} represents the polarization of chiral $CsPbBr_3$ obtained from the CPL results. The P_{cal} value is calculated from the equation: $\mathbf{P} = \frac{\mathbf{P_0}}{\mathbf{1+\frac{\tau}{\tau_s}}}$, where P_0 is the initial polarization ratio after excitation, which for pristine perovskite can be 100%. τ is the recombination time of photoexcitations, and τ_s is the spin relaxation time. (c) The spin diffusion length $\mathbf{L_s}$ for archiral and chiral $CsPbBr_3$ monolayers. The spin diffusion length was calculated according to exciton hoping mode: $\mathbf{L_s} = \sqrt{\mathbf{D_s \tau_s}}$, $\boldsymbol{\tau_s}$ is the spin relaxation lifetime, the spin diffusion coefficient D_s can be expressed as $D_s = D_{hop}+D_{exc}$; includes charge/spin hopping (D_{hop}) and exchange-mediated coupling between spins on adjacent molecules (D_{exc}).

Spin-filtering Charge Transport in $CsPbBr_3$ Nanoplatelets

In a chiral molecule, the current generated in the presence of a magnetic field is directly proportional to the effective magnetic field experienced by electrons as they traverse the molecule. This phenomenon is known as chirality-induced spin selectivity (CISS), which induces a spin-scattering effect on charge carriers within the chiral molecule. Consequently, carriers with a specific spin orientation encounter resistance. The spin-polarized current observed in such cases is attributed to the spin-filtering effect of the oriented chiral organic molecules. [95] The impact of the effective magnetic field on spins, whether parallel or antiparallel to the chiral molecule's handedness, can vary. To investigate the CISS effect in chiral $CsPbBr_3$ nanoplatelets, people employed a device with the following structure: ITO/PEDOT: PSS/$CsPbBr_3$ NPLs/BCP/nickel (Ni)

(Figure 4.10a).[108] The spin filter effect can be quantified using the spin-polarization parameter, denoted as P:

$$P = \frac{I_{up} - I_{down}}{I_{up} + I_{down}} \quad \text{Equation 4.5}$$

Where I_{up} and I_{down} are the measured currents at a particular voltage when the magnetic field is pointing up or down, respectively. In the I-V measurements, bias from -2.0 V to 2.0 V was applied for each CISS $CsPbBr_3$ NPLs device. The Ferromagnetic Ni electrode was premagnetized by an external magnet with an up/down magnetization direction before the measurements. In the charge-carrier injection from the indium tin oxide (ITO)/(PEDOT: PSS) electrode, the carriers drifted perpendicularly through the horizontally oriented chiral halide perovskite and then were injected into the BCP layer before penetrating the magnetized electrode. For ITO/PEDOT: PSS/$CsPbBr_3$ NPLs/BCP when the electrode was magnetized in the up-direction, a higher current can be observed as compared to that when the Ni electrode was magnetized in the down-direction. The results indicate that spin-up charge carriers are preferentially transferred through the RMBA-treated NPLs filtering out the spin-down ones. We obtained a spin-polarized current, P of 40% in R-2ML $CsPbBr_3$ NPLs (Figure 4.10b) which is higher than that P of 10% in untreated 2ML $CsPbBr_3$ NPLs, and P of 43% in chiral 5ML $CsPbBr_3$ NPLs (Figure 4.10c) is higher than that P of 10% in archiral 5ML $CsPbBr_3$ NPLs (Figure 4.10d). The huge difference in spin filtering ability between RMBA treated and untreated $CsPbBr_3$ NPLs illustrates the more predominant role of SOC effect (i.e. Rashba splitting) induced by chiral ligands rather than the SOC effect caused by metal ion (large spin-orbit coupling from heavy Pb atoms). It should be noted that the measurement method only demonstrated that the charge transport in the out-of-plane direction, however, the in-plane charge transport is not clear. The calculated values of P for $CsPbBr_3$ NPLs are smaller than commonly reported chiral halide perovskite bulks (P ~ 80-90%),[54, 93, 109, 110] and comparable to the 2D chiral (R/S-HP1A)$_2PbBr_4$ perovskite thin film (P ~ 40-45%),[111] which could due to the mole fraction of chiral ligands in the NPLs and participation of chiral ligands in the out-of-plane spin transport.[109]

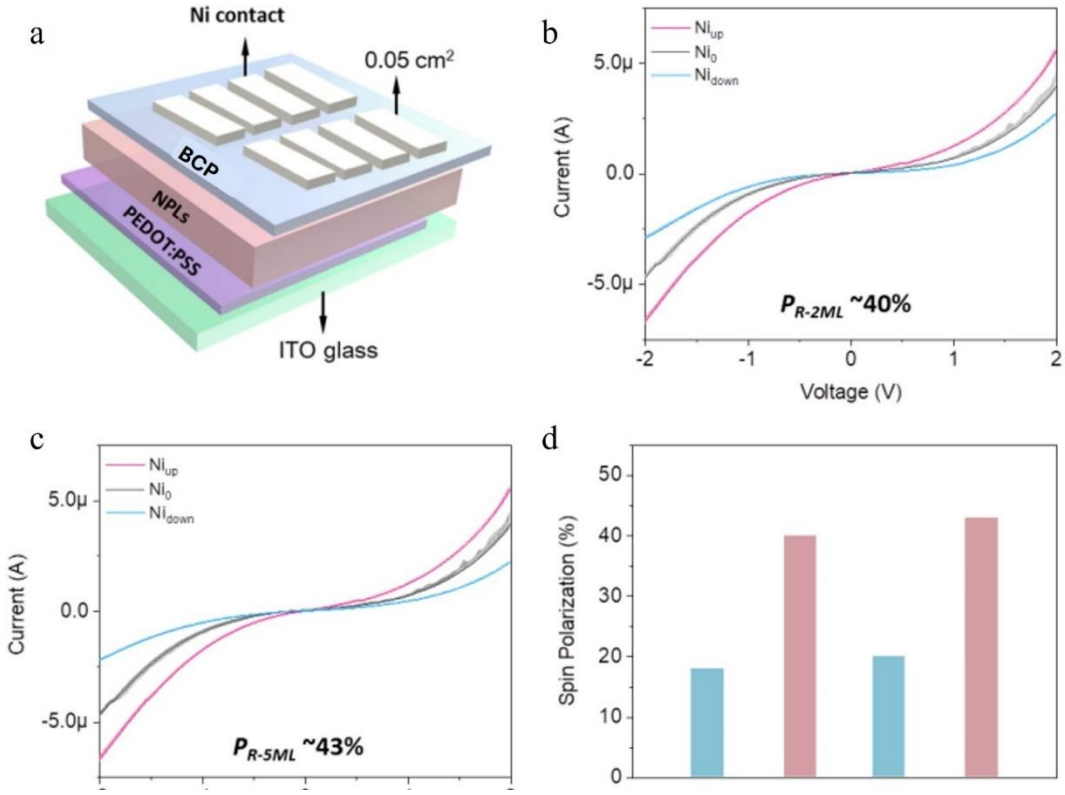

Figure 4.10 Spin-filtering Charge Transport in $CsPbBr_3$ Nanoplatelets. (a) schematic illustration of magnetized I-V response measurement based on $CsPbBr_3$ nanoplatelets; the magnetized I-V response for R-2 ML (b) R-5 ML $CsPbBr_3$ NPLs (c); The Ni contact layer is magnetized in the north (blue), south (red), and non-magnetized (black). The I-V response for each perovskite film was averaged over 10 scans. (d) the extracted spin polarization extracted from (b) and (c), the degree of spin polarization (P) is calculated based on the equation: $P = (I_{up} - I_{down}) / (I_{up} + I_{down})$, where I_{up} and I_{down} are the measured currents at −2 V when the tip magnetic field is pointing up or down, respectively. We obtained a spin-polarized current of ~ 43% in the R-5ML $CsPbBr_3$ film, which is slightly higher than in an analogous R-2ML $CsPbBr_3$ NPL thin film, where P is estimated to be 40%.

Chirality transfer leads to different spin textures for the spin sub-bands between archiral and chiral $CsPbBr_3$ monolayers. To understand the spin-band splitting and spin texture in chiral $CsPbBr_3$ monolayers, we conducted DFT calculations using monolayer models at the GGA/PBE level, incorporating van der Waals (vdW) interactions and spin-orbit (SO) coupling. The band structures shown in Figure 4.11 for the chiral $CsPbBr_3$ monolayers demonstrate that they exhibit greater band splitting compared to the archiral $CsPbBr_3$ monolayers. We observed no obvious band splitting for n = 3 chiral $CsPbBr_3$

monolayers, while n = 2 chiral $CsPbBr_3$ monolayers showed the greatest band splitting along the Γ→X direction compared to the Γ→Y direction when compared to n = 4 and 5 monolayers.

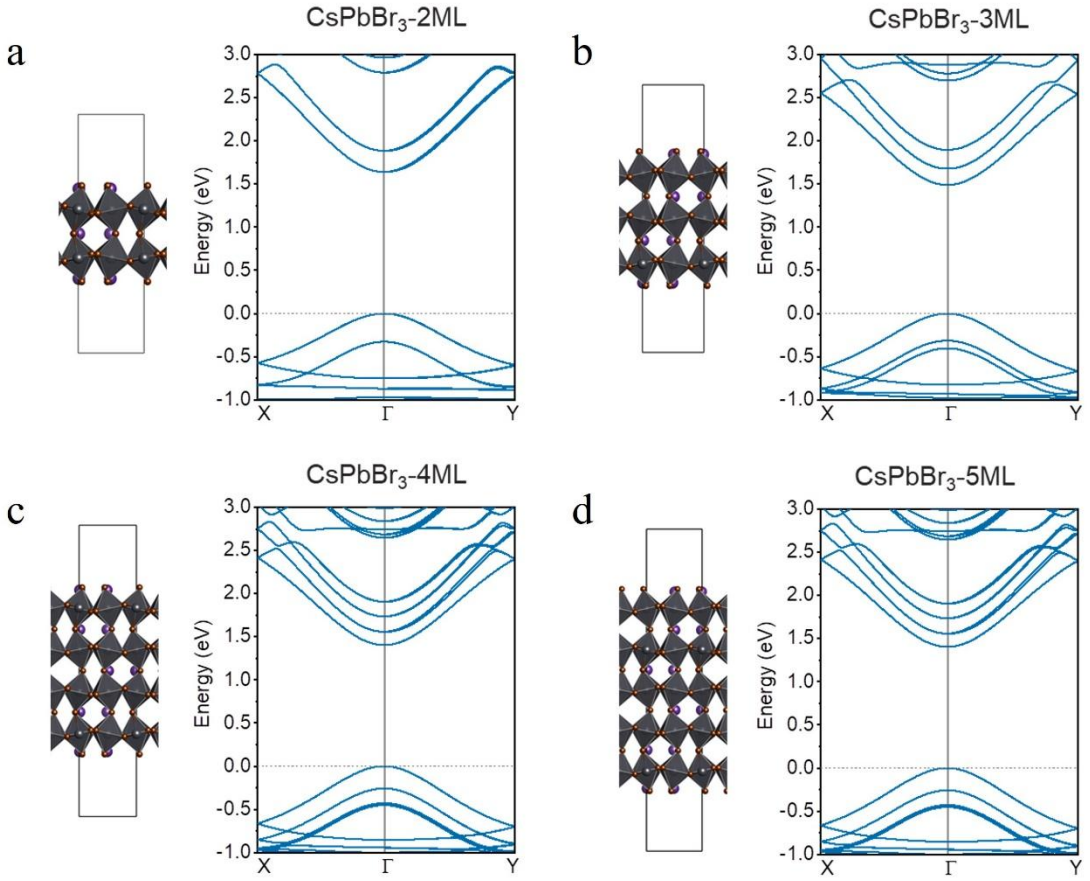

Figure 4.11 Optimized crystal structures and electronic bands for R-$CsPbBr_3$ with (a) 2ML, (b) 3ML, (c) 4ML, and (d) 5ML, as calculated at GGA/PBE+SOC level of theory.

Figure 4.12 illustrates the 2D spin textures of the conduction bands projected on the k_x–k_y plane for the inner (CBM1) and outer (CBM2) branches of chiral $CsPbBr_3$ monolayers with n = 2-5 (a-d). The arrows indicate the in-plane spin components (S_x and S_y), while the blue and red colors represent the degree of spin-up and spin-down of the out-of-plane spin component (S_z). The spin texture exhibits a helical shape in the $k_{x,y}$ plane, which depends on the type of spin splitting and the site symmetry around the high symmetry k point. For Rashba-type splittings, the directions of the corresponding spin texture are perpendicular to the wave vector given by the result of k_x and k_y, whereas for Dresselhaus-type splitting, the spin texture at the k_x and k_y axes are parallel to the axes. The spin texture of the inner (CBM1) and outer (CBM2) branches around the Γ point of the conduction band minimum suggests that both Rashba and Dresselhaus

spin-momentum couplings are simultaneously present in all monolayers, as evidenced by the tangential and radial character of the textures. The chirality transfer from the organic to inorganic sublattices lowers the bulk symmetry of the crystal and introduces combined Rashba-Dresselhaus spin-orbit terms in the relativistic Hamiltonian. This results in bulk in-plane anisotropy in the spin-orbit coupling and gives rise to unusual spin-dependent transport properties.

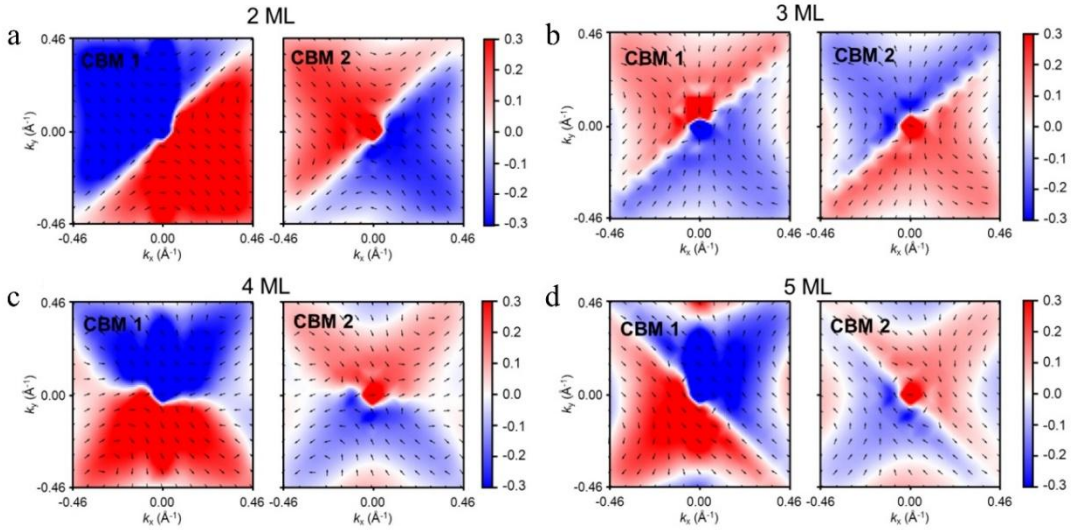

Figure 4.12 2D spin textures of conduction bands projected on the k_x–k_y plane for CBM1 and CBM2 of (a-d) n = 2-5 chiral $CsPbBr_3$ monolayers. The arrows indicate the in-plane spin components (S_x and S_y). The blue and red colors represent the degree of spin-up and spin-down of the out-of-plane spin component (S_z). The DFT calculations were performed at GGA/PBE+vdW with SOC.

4.4 Conclusion

In summary, we focused on investigating the spin relaxation and polarization dynamics in a series of chiral ligand-capped $CsPbBr_3$ nanoplatelets (NPLs). Our findings reveal that the chiral $CsPbBr_3$ monolayers exhibit a remarkably long spin depolarization lifetime, spanning hundreds of picoseconds, and demonstrate high circularly polarized emission with a polarization value of 5.0% at room temperature. Additionally, we estimated a spin diffusion length of up to 33 nm in n = 5 $CsPbBr_3$ monolayers. The chiral $CsPbBr_3$ NPLs show excellent spin-filtering charge transport properties with a high spin transport polarization of approximately 43% due to the CISS effect. The presence of chiral ligands in $CsPbBr_3$ NPLs induces significant Rashba-like splittings of the layers. Our observations of chiral $CsPbBr_3$ NPLs with prolonged exciton spin

depolarization lifetime and impressive spin filtering transport provide valuable insights into the underlying mechanisms and highlight the tremendous potential of chiral perovskite nanostructures for controlling both charge and spin degrees of freedom in next-generation devices based on chiral materials.

Chapter 5 Discovery of Intrinsic Chirality in Lead-free Double Perovskite Nanocrystals

5.1 Introduction

Perovskite materials are a class of compounds that have been the star of keen research in recent years due to their distinct properties and potential applications in optoelectrical devices. The perovskite structure is characterised by a cubic lattice of corner-sharing metal-oxygen octahedra, with a cation occupying the centre of each octahedron.[112] This structure allows for various compositions and properties, making perovskites attractive candidates for various photovoltaic applications. Hybrid organic-inorganic perovskites exhibit superior semiconducting characteristics, such as high absorption coefficients, long carrier diffusion lengths, adjustable band gap, etc.[113] One of the most promising applications of perovskite materials is in photovoltaics, where they have demonstrated high power conversion efficiencies, surpassing 25% in some cases,[114] and can be fabricated using simple, low-cost methods. Additionally, perovskites show potential in other optoelectronic devices, such as light-emitting diodes, field effect transistors, and photodetectors.[115]

Perovskite nanocrystals (NCs), also known as quantum dots, are a subclass of perovskite materials that have attracted significant attention due to their unique properties and potential applications in optoelectronics. The size of perovskite nanocrystals can be precisely controlled, allowing for tunable optical and electronic properties due to the quantum confinement effect, which results in discrete energy levels dependent on the size of the perovskite nanocrystal.[116] Perovskite nanocrystals have demonstrated high photoluminescence quantum yields, making them attractive candidates for light-emitting diodes, displays, and other optoelectronic devices.[117] they also show promise for use in solar cells, which can be used as light absorbers or as components in tandem solar cells.[118] The synthesis of perovskite nanocrystals is typically achieved using solution-based methods, such as hot injection or ligand-assisted reprecipitation.[119] However, there are challenges associated with the synthesis of perovskite nanocrystals, including the need for precise control over the reaction conditions and the potential for instability. Despite these challenges, ongoing research and development of perovskite nanocrystals hold great prospects for developing high-performance optoelectronic devices and other technological applications.

Chirality, the property of a structure not being superimposable on its mirror image, exists in nature, art, architecture, and chemistry.[120] Chiral materials have mirror images called enantiomers, resulting from their non-centrosymmetric structures. These materials exhibit interesting physical properties such as circular dichroism (CD), circular polarization Photoluminescence (CPL), ferroelectricity, photovoltaic effect, and spintronics. Consequently, chiral materials have broad applications in the fields of biology, chemistry, spintronic devices, optics, electronics, and medicine, attracting increasing research attention.[121] Halide perovskites have proven to be a promising candidate for optoelectronic materials for a variety of applications, including solar cells, photonic lasers, photodetectors, and light-emitting diodes (LEDs). Metal hybrid halide perovskite materials possess important properties such as long carrier diffusion lengths, flexible crystal structures, high dielectric constants, high optical absorption coefficients, high tunable band gaps, and strong spin-orbit coupling. However, their chemical structures are typically centrosymmetric,[43] preventing natural chirality and direct application in chirality-related fields. The intentionally introducing chirality forms chiral halide perovskites through chiral molecules. Candidate materials for electronic device applications. Chiral halide perovskite materials were first synthesized in 2003,[122] and the crystal structures of many chiral halide perovskite materials were extensively reported in 2006 and 2013. In 2017, the chiroptical properties of chiral perovskite films were first investigated.[123] Since then, numerous experiments have been carried out to synthesize chiral perovskites, explore their chiral properties, and demonstrated their potential applications in circularly polarized light emission, detection, and spintronics.[124]

Lead-free perovskite materials are emerging as promising alternatives to traditional lead-based perovskites due to their lower toxicity and reduced environmental impact. The shift towards lead-free perovskites is driven by concerns over the harmful effects of lead on human health and the environment. These materials often incorporate elements such as tin, bismuth, or antimony in place of lead within the perovskite crystal structure. They exhibit notable optoelectronic properties, including high photoluminescence quantum yields, high carrier mobility, and excellent stability under ambient conditions.[125] However, the performance of lead-free perovskites generally lags behind that of their lead-based counterparts, and challenges persist in their synthesis and stability. Recent research efforts have focused on addressing these

challenges and improving the performance of lead-free perovskites.[126] Strategies include modifying the crystal structure with dopants or defects to improve charge transport and reduce defect density,[127] as well as developing hybrid perovskites that combine inorganic and organic components to boost stability and performance.[128] Lead-free perovskites have shown possibilities for use in a range of optoelectronic applications, such as solar cells, light-emitting diodes, photodetectors, and sensors.[129] Despite the growing interest in chiral perovskite materials, there is a notable lack of research on the chiral properties of lead-free double perovskite nanocrystals. This gap in the literature has prompted us to focus our research on this area.

5.2 Results and Discussion

Synthesis method

We synthesized Cs2AgIn$_x$Bi$_{1-x}$Cl$_6$ (x=0, 0.3, 0.6, 0.9, and 1) nanocrystals (NCs) using a hot injection method. The process begins with the preparation of a cesium-oleate (Cs-OA) stock solution. Next, silver chloride (AgCl), bismuth chloride (BiCl3), and indium chloride (InCl3) are dissolved in a mixture of octadecene (ODE), oleic acid, and oleylamine (OAm), with hydrochloric acid added to enhance the solubility of the metal salts. Finally, the cesium oleate solution is rapidly injected into the metal salt solution to form perovskite nanocrystals.

Steady-State Absorption and Photoluminescence Properties

The optical properties of the nanocrystals were conducted to analyze the characterization of the synthesized Cs2AgIn$_x$Bi$_{1-x}$Cl$_6$ nanocrystals (NCs). The absorption spectrum of $Cs_2AgBiCl_6$ NCs exhibited an exciton peak at 366 nm and a long absorption tail extending up to 600 nm (Figure 5.1a). The exciton peak is attributed to the direct bismuth s-p transition, while the sub-bandgap absorption tail is primarily associated with trap-state-related transition and indirect band gap transition.[130] Despite the presence of the indirect band gap transition, which is an intrinsic property of the material, $Cs_2AgBiCl_6$ NCs exhibited low photoluminescence quantum efficiency, indicating that they are not suitable for optoelectronic applications. These findings underscore the importance of carefully considering the intrinsic properties of nanocrystals when selecting materials for such optoelectronic applications. It is noteworthy that an increase in indium content leads to significant suppression of the absorption tail. Specifically, absorption spectra of $Cs_2AgIn_{0.9}Bi_{0.1}Cl_6$ NCs exhibit sharp

band edges, suggesting that the $Cs_2AgIn_{0.9}Bi_{0.1}Cl_6$ NCs may possess a direct band gap nature. Further details on this observation will be elaborated upon below.

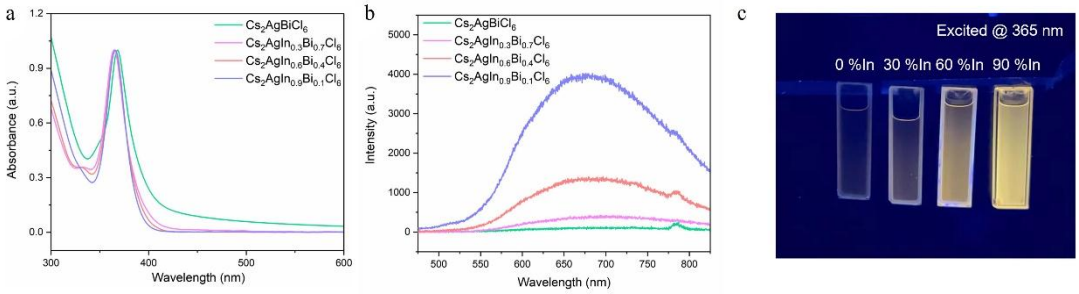

Figure 5. 1 (a) Normalized steady-state absorption spectra of $Cs_2AgIn_xBi_{1-x}Cl_6$ (x = 0, 0.3, 0.6, and 0.9) NCs. (b) PL spectra of $Cs_2AgIn_xBi_{1-x}Cl_6$ (x = 0, 0.3, 0.6, and 0.9) NCs. (c) The brightness image of $Cs_2AgIn_xBi_{1-x}Cl_6$ (x = 0, 0.3, 0.6, and 0.9) NCs under a UV light of 365 nm.

Figure 5.1b presents the steady-state photoluminescence (PL) spectra of synthesized $Cs_2AgIn_xBi_{1-x}Cl_6$ (x = 0, 0.3, 0.6, and 0.9) NCs, accompanied by photographs of the corresponding samples under UV light, as depicted in Figure 5.1c. The undoped $Cs_2AgBiCl_6$ NCs exhibit a weaker broadband around 600 nm, attributed to self-trapped excitons or the recombination of localized carriers within a soft lattice, as previously reported. Upon doping with In^{3+}, the luminescence intensity is significantly increased, with the peak shifting to approximately 650 nm. Notably, when x = 0.9, the PL intensity is the strongest, indicating the potential utility of these nanomaterials for optoelectronic applications.

Morphology and Crystal Structure

Note that Figures 5.2a and 5.2c display scanning transmission electron microscopy (STEM) images of $Cs_2AgBiCl_6$ NCs and $Cs_2AgIn_{0.9}Bi_{0.1}Cl_6$ NCs, both exhibiting a cubic shape. The average diameters are 9.56±0.03 nm for $Cs_2AgIn_{0.9}Bi_{0.1}Cl_6$ NCs and 8.84±0.04 nm for $Cs_2AgBiCl_6$ NCs, respectively. (Figure 5.2b and 5.2d). The STEM images of $Cs_2AgIn_{0.3}Bi_{0.7}Cl_6$ NCs and $Cs_2AgIn_{0.6}Bi_{0.4}Cl_6$ NCs also show a cubic shape, indicating a high degree of crystallinity in the $Cs_2AgIn_xBi_{1-x}Cl_6$ nanocrystals, which is advantageous for various perovskite optoelectronic applications.

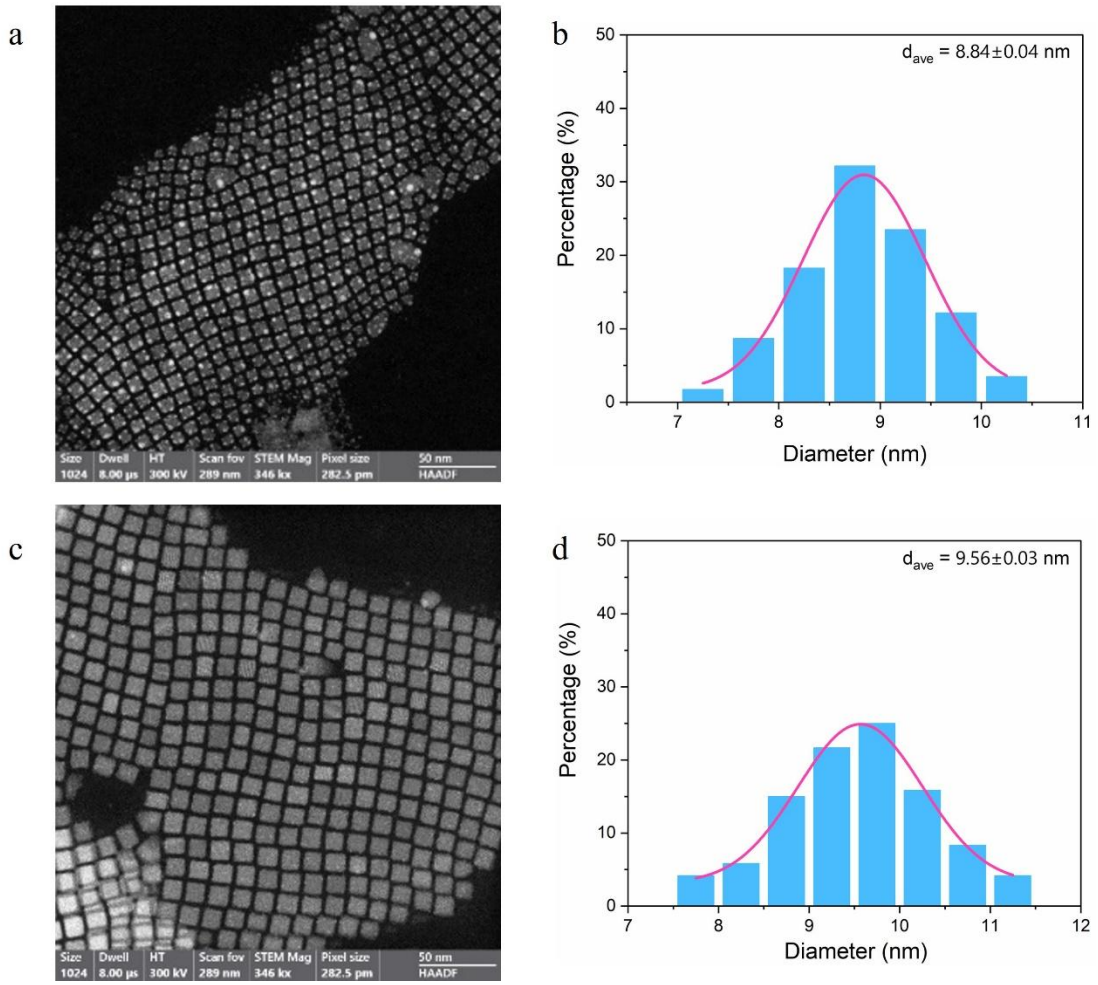

Figure 5. 2 TEM image of (a) $Cs_2AgBiCl_6$ NCs and (c) $Cs_2AgIn_{0.9}Bi_{0.1}Cl_6$ NCs. (b) Size distribution histogram of (b) $Cs_2AgBiCl_6$ NCs and (d) $Cs_2AgIn_{0.9}Bi_{0.1}Cl_6$ NCs.

The X-ray diffraction (XRD) patterns confirm that $Cs_2AgIn_xBi_{1-x}Cl_6$ NCs exhibit high crystallinity and belong to the $Fm\bar{3}m$ cubic space group, similar to $Cs_2AgBiCl_6$ (Figure 5.3a). Magnified XRD images (Figure 2b) show peaks shifting towards higher diffraction angles with increasing indium components, consistent with lattice contraction as Bi^{3+} cations (117 pm) are replaced by smaller In^{3+} cations (94 pm). These results demonstrate the successful synthesis of high-quality, lead-free double perovskite NCs with tunable indium-bismuth compositions.

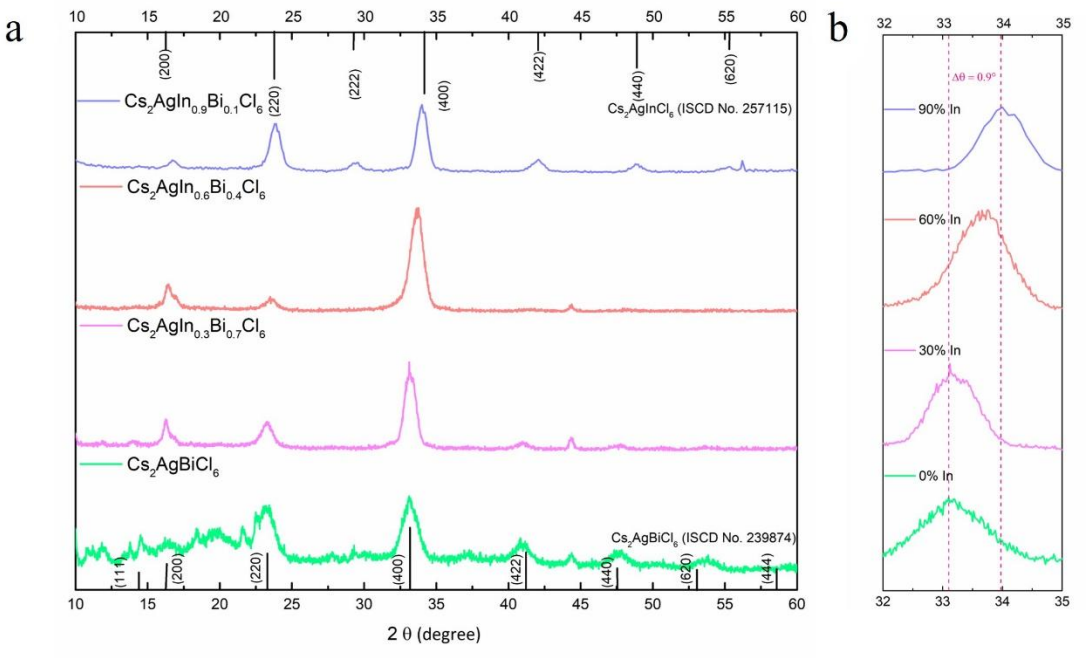

Figure 5. 3 (a) XRD patterns of $Cs_2AgIn_xBi_{1-x}Cl_6$ (x = 0, 0.3, 0.6, and 0.9) NCs (b) and magnified images of XRD patterns (b). The black bars represent the XRD patterns of $Cs_2AgBiCl_6$ and $Cs_2AgInCl_6$.

The high-resolution STEM (HR-STEM) images also reveal a high level of crystallinity in the $Cs_2AgIn_{0.9}Bi_{0.1}Cl_6$ NCs (Figure 5.4a) and $Cs_2AgBiCl_6$ NCs (Figure 5.4b), as evidenced by the lattice spacing values of 0.38 and 0.37 nm, respectively corresponding to the (220) diffraction peaks. The difference in the lattice spacing value between $Cs_2AgIn_{0.9}Bi_{0.1}Cl_6$ NCs and $Cs_2AgBiCl_6$ NCs caused by the doping of indium content.

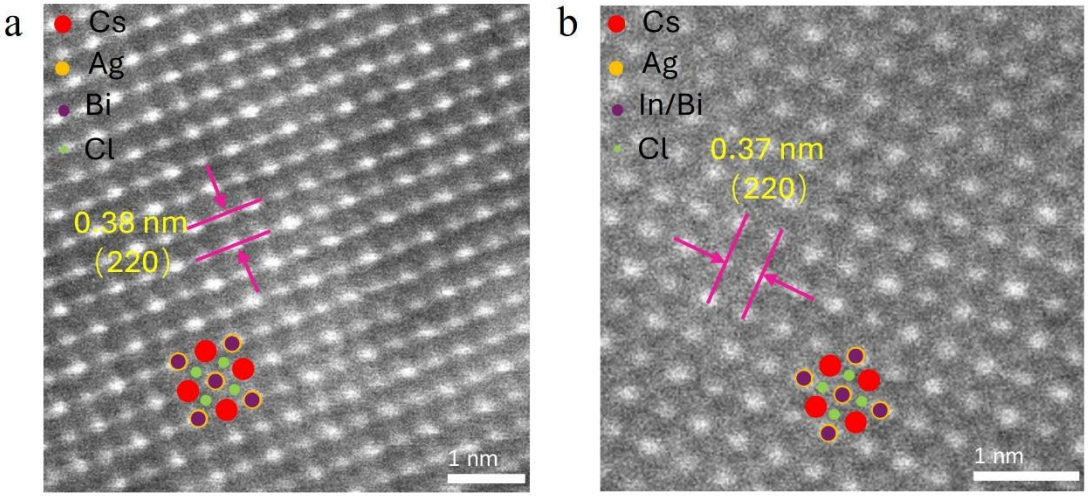

Figure 5. 4 HR-STEM images of (a) $Cs_2AgIn_{0.9}Bi_{0.1}Cl_6$ NCs and (b) $Cs_2AgBiCl_6$ NCs.

Additionally, the energy-dispersed X-ray spectroscopy in STEM (STEM-EDS) measurements of $Cs_2AgBiCl_6$ NCs (Figure 5.5) indicate a uniform elemental distribution. Additionally, we have observed small Ag nanocrystals decorating the cubes, which suggests the degradation process of silver-based double perovskites. Previous research with $Cs_2AgBiBr_6$ NCs has shown that these smaller silver nanocrystals grow during the growth reaction itself and not subsequently during analysis through an interaction with the TEM beam.[131, 132]

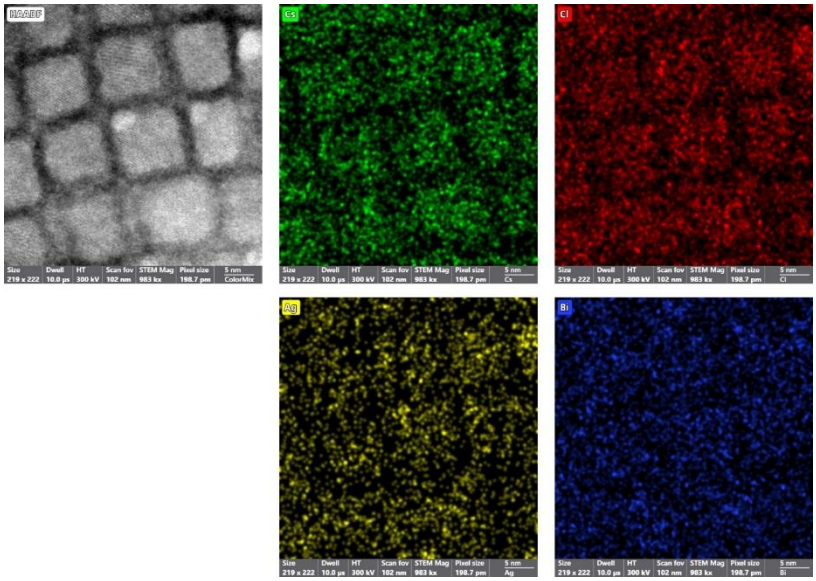

Figure 5. 5 STEM–EDS map of $Cs_2AgBiCl_6$ NCs.

Figure 5.6 shows that all elements in $Cs_2AgIn_{0.9}Bi_{0.1}Cl_6$ NCs are uniformly distributed, indicating an alloyed nature where indium and bismuth are homogeneously mixed within the crystal lattice. This uniform distribution enhances our understanding of the structural and compositional properties of lead-free double perovskite nanocrystals, with significant implications for their use in optoelectronic devices.

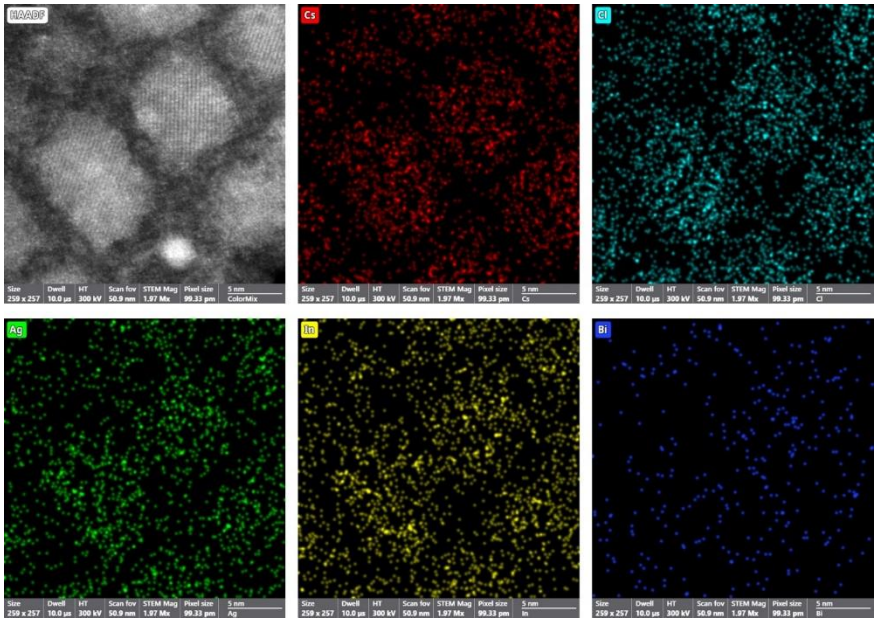

Figure 5. 6 STEM–EDS map of $Cs_2AgIn_{0.9}Bi_{0.1}Cl_6$ NCs.

Transient photoluminescence (TRPL) measurements were conducted to uncover the underlying mechanism responsible for the observed heightened photoluminescence (PL) intensity in In-doped lead-free double perovskite nanocrystals. Figure 5.7a depicts a short-lived component ($\tau_1 \approx 1.48$ ns) and a long-lived component ($\tau_2 \approx 26.08$ ns) in $Cs_2AgBiCl_6$ NCs. The short-lived component is attributed to charge-carrier recombination processes, while the long-lived component is due to the emission from sub-band-gap states.[133] Furthermore, it was observed that the long-lived component accounted for a larger percentage at longer PL wavelengths, which is consistent with the notion that sub-band-gap trap states generally exhibit longer lifetimes (463.06 ns) compared to band edge emission in $Cs_2AgIn_{0.9}Bi_{0.1}Cl_6$ NCs (Table 5.1). The observed phenomenon can be explained by the charge-carrier dynamics model presented in Figure 5.7b and c. In indirect bandgap nanocrystals, absorption and recombination are responsible for photons and phonons. The phonon-assisted absorption and recombination process can induce a strong carrier-phonon coupling effect in indirect bandgap ($Cs_2AgIn_xBi_{1-x}Cl_6$ (x = 0, 0.3, 0.6,)) NCs, leading to the formation of "dark" (non-radiative) self-trapped states that are responsible for undetectable photoluminescence at room temperature. However, in the case of direct bandgap $Cs_2AgIn_xBi_{1-x}Cl_6$ (x = 0.9) NCs, moderate exciton-phonon coupling strength produces radiative self-trapped excitons, which exhibit bright broadband self-trapped exciton photoluminescence.

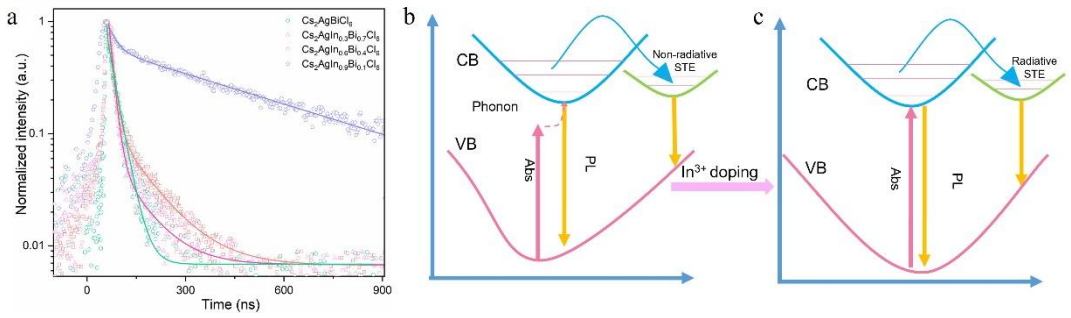

Figure 5. 7 (a) TRPL kinetics of $Cs_2AgIn_xBi_{1-x}Cl_6$ NCs. Charge Carrier Dynamics Model of (b) indirect Band Gap Double Perovskite $Cs_2AgIn_xBi_{1-x}Cl_6$ (x = 0, 0.3, and 0.6) NCs and (c) direct Band Gap Double Perovskite $Cs_2AgIn_xBi_{1-x}Cl_6$ (x = 0.9) NCs.

Table 5.1 Summary of parameters obtained by fitting the dual exponential attenuation equation of TRPL spectrum in $Cs_2AgIn_xBi_{1-x}Cl_6$ (x = 0, 0.3, 0.6, and 0.9) NCs

CONTENT	A_1 (%)	A_2 (%)	τ_1 (ns)	τ_2 (ns)	τ_{ave} (ns)
$Cs_2AgInBiCl_6$	0.17	0.74	1.48	26.08	25.76
$Cs_2AgIn_{0.3}Bi_{0.7}Cl_6$	0.87	0.06	13.24	83.86	34.71
$Cs_2AgIn_{0.6}Bi_{0.4}Cl_6$	0.89	0.11	13.34	99.45	54.63
$Cs_2AgIn_{0.9}Bi_{0.1}Cl_6$	0.39	0.56	25.02	478.99	463.06

The chiral $Cs_2AgIn_xBi_{1-x}Cl_6$ DPNCs were treated through ligand exchange (see experimental method). The rac-$Cs_2AgIn_xBi_{1-x}Cl_6$ DPNCs were initially coated with oleylamine and oleic acid ligands, and then part of the surface ligands was replaced by the chiral molecular (R/S-methyl benzylamine) via post-treatment. The chiral DPNCs have crystal structures and morphology similar to the achiral DPNCs in Figure 5.8.

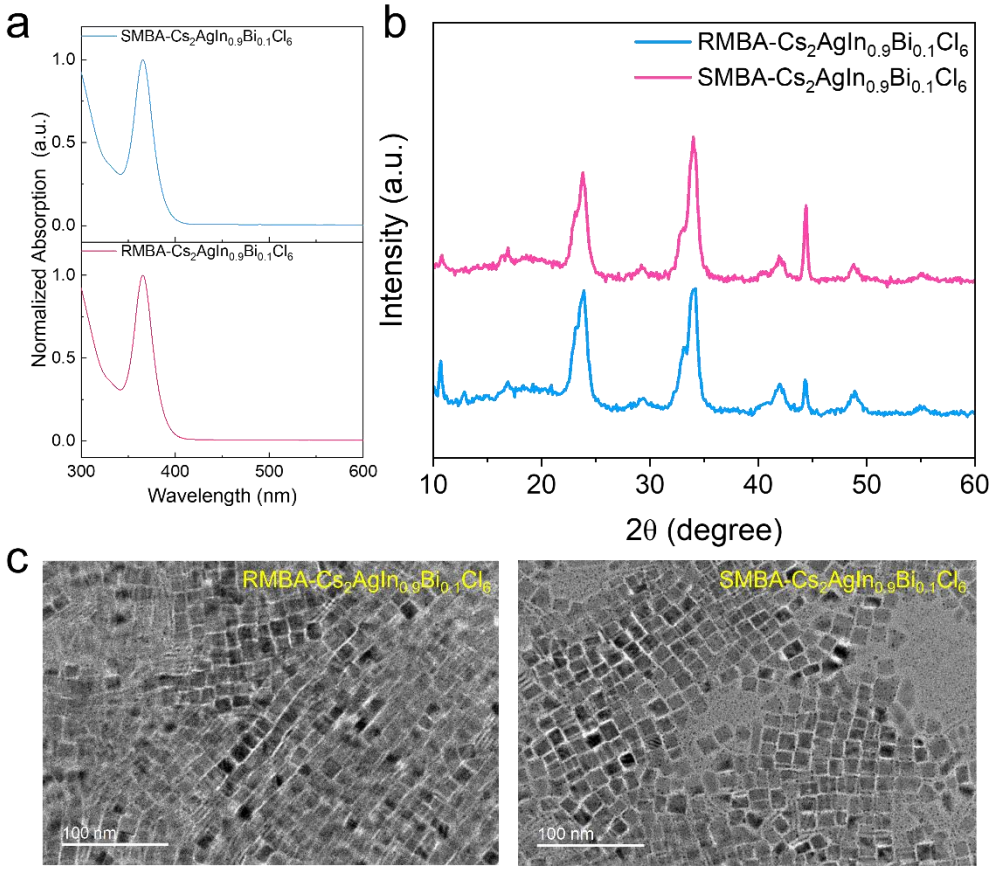

Figure 5. 8 (a) Normalized steady-state absorption spectra of RMBA/SMBA-$Cs_2AgIn_{0.9}Bi_{0.1}Cl_6$ DPNCs. (b) XRD pattern of RMBA/SMBA-$Cs_2AgIn_{0.9}Bi_{0.1}Cl_6$ DPNCs. (c) TEM images RMBA-$Cs_2AgIn_{0.9}Bi_{0.1}Cl_6$ DPNCs and SMBA-$Cs_2AgIn_{0.9}Bi_{0.1}Cl_6$ DPNCs.

Chiral-Optical Properties

The circular dichroism (CD) spectra of untreated and chiral ligand R-/S-MBA-treated $Cs_2AgIn_{0.9}Bi_{0.1}Cl_6$ NCs are shown in Figure 5.8a. The CD spectra of the untreated $Cs_2AgIn_{0.9}Bi_{0.1}Cl_6$ NCs exhibited characteristic features that were indicative of the nanocrystal's intrinsic chiral properties. After treatment with the chiral ligand, the CD spectra of the NCs exhibited a significant enhancement in the intensity of the chiral signal. This observation suggests that the chiral ligand was able to effectively interact with the surface of the NCs and induce a chiral environment that increased the chiral optical activity of the NCs. To provide additional evidence of the intrinsic chiral properties of $Cs_2AgIn_{0.9}Bi_{0.1}Cl_6$ NCs, we conducted circular dichroism (CD) spectral analysis on $Cs_2AgIn_{0.9}Bi_{0.1}Cl_6$ NCs and $Cs_2AgBiCl_6$ NCs (Figure 5.8b). Our findings

revealed that $Cs_2AgIn_{0.9}Bi_{0.1}Cl_6$ NCs exhibited a clear CD signal at 366 nm, while $Cs_2AgBiCl_6$ NCs lacked any discernible CD signal. This observation supports the notion that the intrinsic chiral properties of nanocrystals are highly dependent on their specific composition and crystal structure.

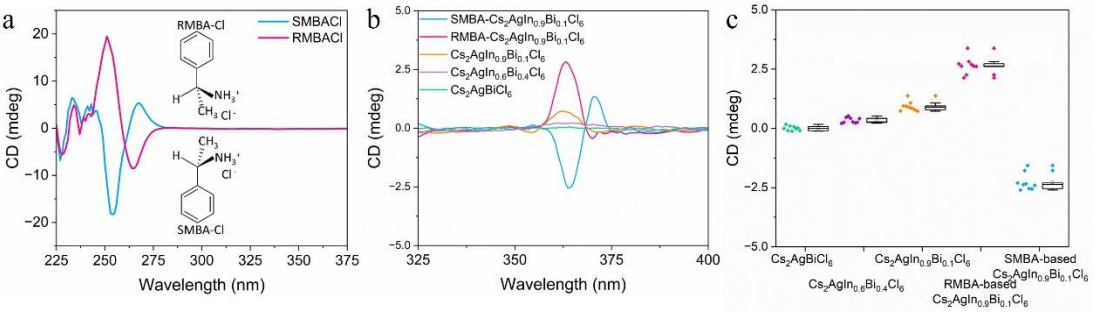

Figure 5. 9 (a) CD spectra of pure chiral ligand. (b) CD spectra of $Cs_2AgIn_xBi_{1-x}Cl_6$ NCs and RMBA/SMBA-$Cs_2AgIn_{0.9}Bi_{0.1}Cl_6$ NCs. (c) Distribution statistics of the CD values for rac-$Cs_2AgIn_xBi_{1-x}Cl_6$ NCs and chiral R/SMBA-$Cs_2AgIn_{0.9}Bi_{0.1}Cl_6$ NCs.

To investigate the underlying mechanism responsible for the chiral signal observed in $Cs_2AgIn_{0.9}Bi_{0.1}Cl_6$ NCs, high-angle ring dark-field scanning transmission electron spectroscopy (HADDF-STEM) tests were performed (Figure 5.9a). In contrast, the atoms of $Cs_2AgBiCl_6$ NCs exhibit a highly organized arrangement without any indication of dislocations.

Analysis of the STEM images revealed that dislocations were detected in only a small fraction of the nanocrystals (i.e., 1 out of 20-30), potentially due to the low probability of screw dislocations occurring in nanocrystals. It should be noted that the identification of screw dislocations in those as mentioned earlier high-angle circular dark-field scanning transmission electron microscopy (HAADF-STEM) tests, as described above, is consistent with previous research conducted by Yurri Gunko on the role of screw-dislocation-induced intrinsic chirality in CdSe/ZnS quantum dots (QDs).[134] These findings support the hypothesis that the intrinsic chirality of the nanocrystals arises from the presence of chiral defects. Figure 5.9c provides schematic diagrams of the non-uniform atomic distribution within the crystal, which may arise as a result of the presence of screw dislocations in $Cs_2AgIn_{0.9}Bi_{0.1}Cl_6$ NCs. The dislocation model (Figure 5.9b) based on the Burgers vector b=1/2 [100] and lattice vectors x, y, and z, shows that most atomic positions in $Cs_2AgIn_{0.9}Bi_{0.1}Cl_6$ NCs with screw dislocation match the simulated atomic module.

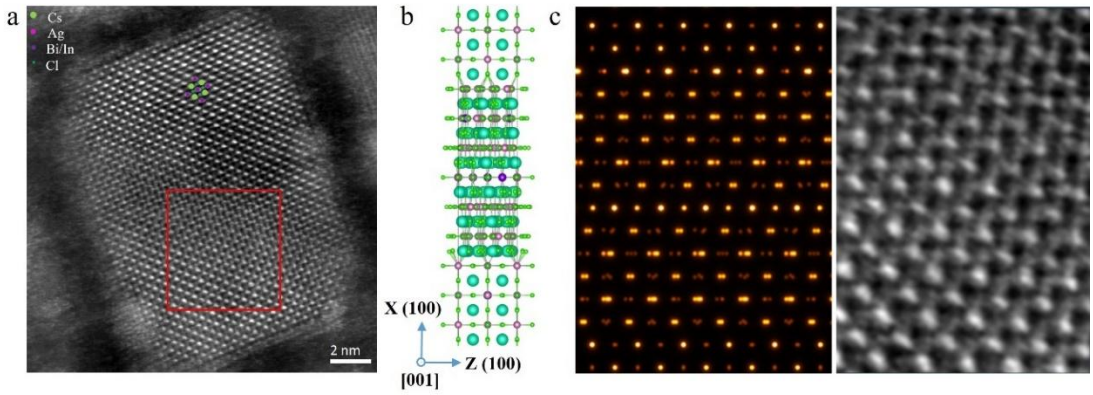

Figure 5. 10 Crystals structure of the screw dislocation in $CsAgIn_{0.9}Bi_{0.1}Cl_6$ NCs. (a) HADDF-STEM images of a 1/2 [100] screw dislocation in cubic $CsAgIn_{0.9}Bi_{0.1}Cl_6$ NCs viewed perpendicular direction to the screw dislocation line, (b) the screw dislocation model of $CsAgIn_{0.9}Bi_{0.1}Cl_6$ NCs based on the Burgers vector b=1/2 [100] and the lattice vector x, y, z, and (c) is an enlarged image of selected region of (a) and simulated atomic model according to the HADDF-STEM images.

To further verify the impact of intrinsic chirality on the optical properties of nanocrystals, we developed specialized equipment for circularly polarized luminescence (CPL) measurements. A distinct change in the CPL intensity was observed in the spectra of the $Cs_2AgIn_{0.9}Bi_{0.1}Cl_6$ NCs (Figure 5.10b), contrasting sharply with the absence of any discernible CPL intensity change in $Cs_2AgBiCl_6$ nanocrystals (Figure 5.10a). The degree of circularly polarized luminescence (CPL) was assessed using the luminescence dissymmetry factor (glum), calculated as $g_{lum} = 2 \times (I_L - I_R)/ (I_L + I_R)$, where I_L and I_R represent the intensity of left- and right-handed CPL, respectively. The calculated value of the g_{lum} of $Cs_2AgIn_{0.9}Bi_{0.1}Cl_6$ NCs is 0.065. As shown in Figure 5.10 c and 5.10d, we obtained a luminescence dissymmetry factor, g_{lum} of 0.11 in RMBA-$Cs_2AgIn_{0.9}Bi_{0.1}Cl_6$ NCs and 0.084 in SMBA-$Cs_2AgIn_{0.9}Bi_{0.1}Cl_6$ NCs which is higher than the g_{lum} in $Cs_2AgIn_{0.9}Bi_{0.1}Cl_6$ NCs. These findings of CPL spectra hold significant implications for the design and development of chiral nanomaterials, with potential applications in fields such as catalysis, sensing, and biomedical engineering.

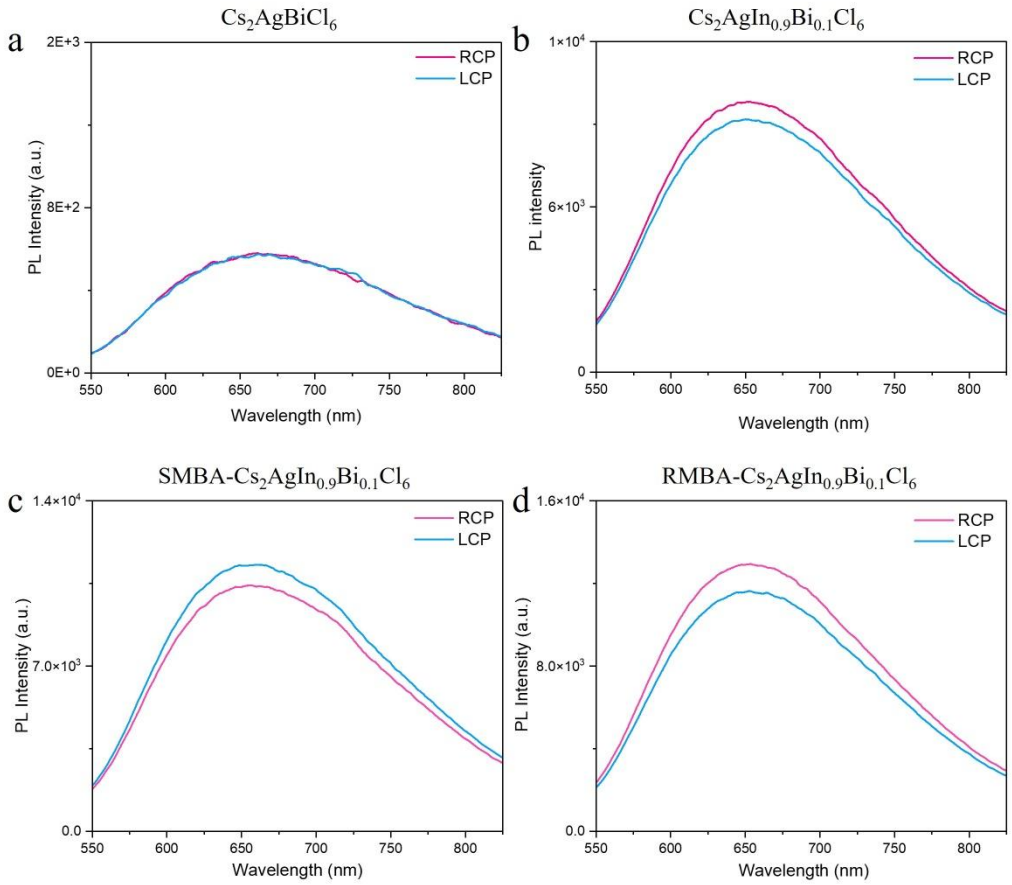

Figure 5. 11 Circularly polarized photoluminescence of (a) $Cs_2AgBiCl_6$ NCs, (b) $Cs_2AgIn_{0.9}Bi_{0.1}Cl_6$ NCs, (c) SMBA-treated $Cs_2AgIn_{0.9}Bi_{0.1}Cl_6$ NCs and (d) RMBA-treated $Cs_2AgIn_{0.9}Bi_{0.1}Cl_6$ NCs.

To characterize the spin-split states of $Cs_2AgIn_xBi_{1-x}Cl_6$ (x = 0.9 and 0) NCs and R/S-MBA treated $Cs_2AgIn_{0.9}Bi_{0.1}Cl_6$ NCs, we conducted the co- and counter-circularly polarized pump-probe configurations, with σ+ excitation light. A clear intensity difference is observed when probing above NCs with σ+ and σ- photons. The polarization can be described by the equation as follows:

$$P_s = \frac{\Delta A_{counter} - \Delta A_{co}}{\Delta A_{counter} + \Delta A_{co}} \times 100\% \qquad \text{Equation 5.1}$$

where ΔA_{co} and $\Delta A_{counter}$ are the TA signals with the same or opposite pump-probe circular polarization, respectively. Figure 5.11a and b show the exciton depolarization dynamics of $Cs_2AgIn_xBi_{1-x}Cl_6$ (x=0.9 and 0.1) NCs. The spin polarization degree of $Cs_2AgBiCl_6$ NCs decays rapidly over the 1.3ps to about 0. However, the P_s of $Cs_2AgIn_{0.9}Bi_{0.1}Cl_6$ NCs experience a fast decay during the first 1 ps, which is limited by the short exciton spin lifetime, and then maintain a P_s of 25% for over 10ns. In turn to the polarization of R/S-MBA treated $Cs_2AgIn_{0.9}Bi_{0.1}Cl_6$ NCs (see Figure 5.11c and

d), when excitation with σ+ photons, the spin polarization degrees of R/SMBA-$Cs_2AgIn_{0.9}Bi_{0.1}Cl_6$ NCs decreases to a maximum value of 40% and 36% respectively. And a long depolarization relaxation lifetime of close to 10 ns can be found in R/SMBA-$Cs_2AgIn_{0.9}Bi_{0.1}Cl_6$ NCs. In the chiral perovskite nanocrystals, it was reported that the chiral crystal structures would first provide an initial polarized state, and the angular momentum orientations of polarized excitons would also be preserved, resulting in a longer spin relaxation time in the nanosecond time range. The introduction of chiral ligands (RMBA and SMBA) would change the environment of spin-orbit coupling, leading to symmetry breaking in NCs. In the previous reports, the origin of the long spin lifetime is the relatively large Rashba splittings.[135] The Rashba splittings in $Cs_2AgIn_{0.9}Bi_{0.1}Cl_6$ NCs and R/SMBA-treated $Cs_2AgIn_{0.9}Bi_{0.1}Cl_6$ NCs require further supporting of density functional theory (DFT) calculations.

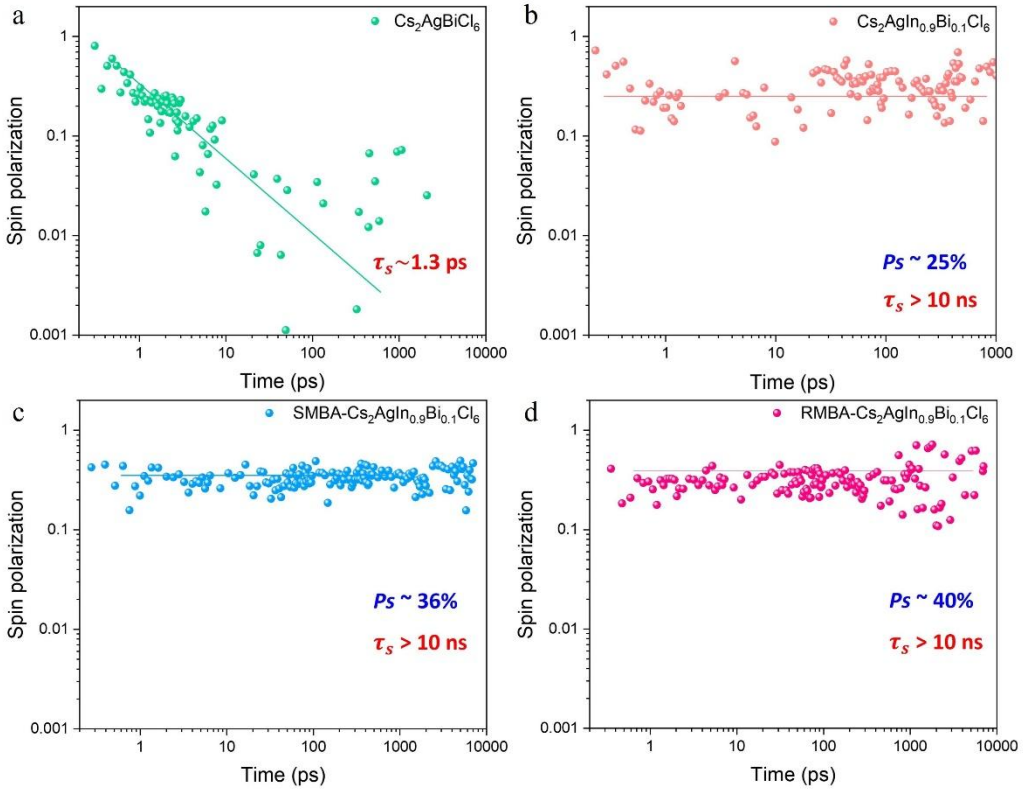

Figure 5. 12 The exciton depolarization dynamic of (a) $Cs_2AgBiCl_6$ NCs, (b) $Cs_2AgIn_{0.9}Bi_{0.1}Cl_6$ NCs, (c) SMBA-treated $Cs_2AgIn_{0.9}Bi_{0.1}Cl_6$ NCs and (d) RMBA-treated $Cs_2AgIn_{0.9}Bi_{0.1}Cl_6$ NCs under the co- and counter-circularly polarized pump-probe configurations.

The CISS effect is assessed by the measurement of the spin-polarized dark current in $Cs_2AgIn_xBi_{1-x}Cl_6$ NCs to characterize the spin filter behaviors of photogenerated

carriers. The CISS device structure based on the $Cs_2AgIn_{0.9}Bi_{0.1}Cl_6$ NCs and chiral ligand-treated $Cs_2AgIn_{0.9}Bi_{0.1}Cl_6$ NCs is shown in Figure 5.12a. The indium tin oxide (ITO) acts as a transparent electrode, and PEDOT: PSS was spin-coated onto it and used as a hole transfer layer (HTL) in the spin device. The $Cs_2AgIn_{0.9}Bi_{0.1}Cl_6$ NCs that were not treated with chiral ligands and those treated with chiral ligands were then spin-coated onto ITO/PEDOT: PSS multiple times. A thin BCP layer is used as a buffer layer to overcome the obstacle of the spin injection in the spin photovoltaic device. The $Ni_{80}Fe_{20}$ electrode acts as the permanent magnet to ensure the injection of carriers along one spin direction after an external magnetic field. The top electrode gold (Au) protects the CISS device from oxidation and decay. Before the measurements of current-voltage (I-V) curves in CISS devices based on $Cs_2AgInxBi_{1-x}Cl_6$ NCs (x = 0.9 and 0) and chiral ligand-treated $Cs_2AgIn_{0.9}Bi_{0.1}Cl_6$ NCs, the $Ni_{80}Fe_{20}$ electrode is magnetized with different magnetization directions （field-up or field-down to the ITO electrode） for about 30 minutes. The CISS devices of $Cs_2AgBi_1Cl_6$ NCs show negligible change of current in different magnetization directions (Figure 5.12c). On the contrary, the CISS device based on the $Cs_2AgIn_{0.9}Bi_{0.1}Cl_6$ NCs showed a higher current in Figure 5.12d when the $Ni_{80}Fe_{20}$ electrode is magnetized up (1.51×10^{-4} A at 2 V) than the current when the $Ni_{80}Fe_{20}$ electrode is magnetized down (5.46×10^{-5} A at 2 V). For the RMBA-treated $Cs_2AgIn_{0.9}Bi_{0.1}Cl_6$ NCs CISS device, a much higher current is shown in Figure 5.12f when the $Ni_{80}Fe_{20}$ electrode is magnetized in the “up” direction versus that in the “down” direction. Carriers with their spin oriented parallel to the $Ni_{80}Fe_{20}$ electrode magnetization direction are preferentially transferred from the ITO electrode to the magnetized $Ni_{80}Fe_{20}$ electrode over those with antiparallel spin orientation. The opposite behaviour is demonstrated for the SMBA-treated $Cs_2AgIn_{0.9}Bi_{0.1}Cl_6$ NCs CISS device, where a lower current is observed when the $Ni_{80}Fe_{20}$ electrode is magnetized in the field-up direction as compared to the field-down direction (Figure 5.12e). To quantify the anisotropy of the spin-polarized currents that we measured, we define the degree of the spin polarization, P_{spin}, as

$$P_{spin} = \frac{I_{up} - I_{down}}{I_{up} + I_{down}} \times 100\% \qquad \text{Equation 5.2}$$

Where I_{up} and I_{down} are the average spin-polarizaed current at 2 V, which measured at room temperature. P_{spin} of the above four NCs CISS devices are summarized in Figure 5.12b. It is seen that the P_{spin} of +30% for $Cs_2AgIn_{0.9}Bi_{0.1}Cl_6$ NCs CISS device, +50%

for RMBA-treated $Cs_2AgIn_{0.9}Bi_{0.1}Cl_6$ NCs CISS device and −47% for SMBA-treated $Cs_2AgIn_{0.9}Bi_{0.1}Cl_6$ NCs CISS device, respectively.

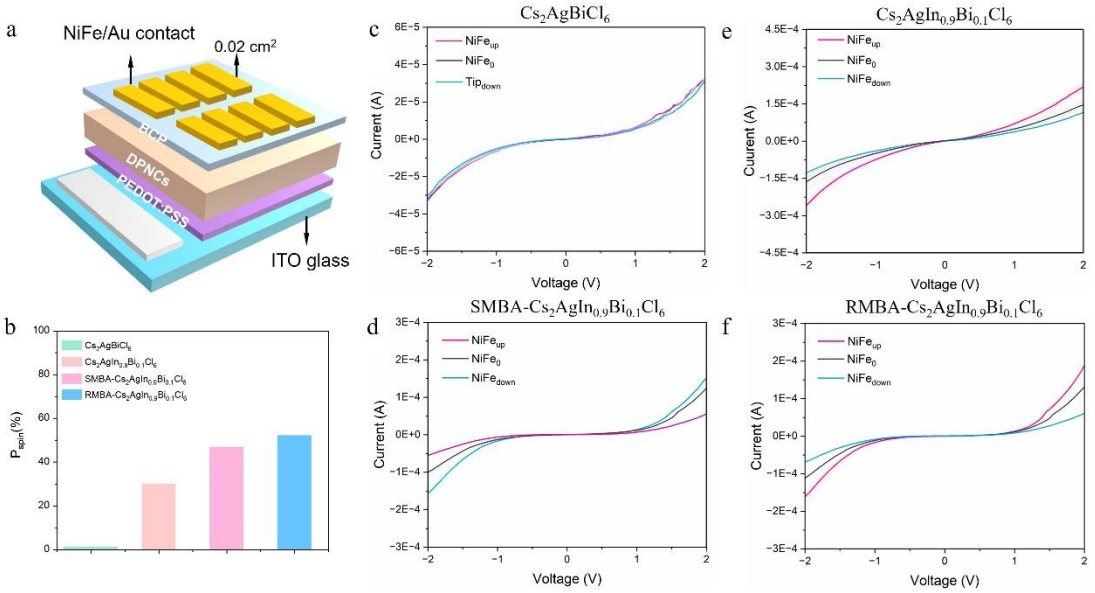

Figure 5. 13 Schematic illustration of CISS devices from the I-V measurements. (a) The diagram of the CISS device structure. (b) The summarized degree of the spin-polarized current in untreated and chiral ligand-treated $Cs_2AgIn_xBi_{1-x}Cl_6$ (x = 0.9 and 0.1) NCs CISS device. The magnetized I-V response measurement based on (c) $Cs_2AgBiCl_6$ NCs, (d) $Cs_2AgIn_{0.9}Bi_{0.1}Cl_6$ NCs, (e) SMBA-treated $Cs_2AgIn_{0.9}Bi_{0.1}Cl_6$ NCs and (f) RMBA-treated $Cs_2AgIn_{0.9}Bi_{0.1}Cl_6$ NCs CISS device. All the measurements are conducted at room temperature.

The photovoltaic response is measured under a 340 nm LED at room temperature. The device structure is illustrated in Figure 5.13. First, the ITO was covered with a hole transport layer (PEDOT: PSS). The untreated and chiral ligand-treated $Cs_2AgIn_xBi_{1-x}Cl_6$ (x = 0.9 and 0.1) NCs were spin-coated on a PEDOT: PSS thin film 6 times. Then an electron transport layer (ETL; $PC_{61}BM$) was spin-coated on the perovskite NCs layers. The 5-nm $Ni_{80}Fe_{20}$ permanent magnet electrode was deposited after the sample was transferred into a vacuum condition. Finally, a 35-nm gold (Au) was coated onto the $Ni_{80}Fe_{20}$ layer for oxidation prevention. The performance of untreated and chiral ligand-treated $Cs_2AgIn_xBi_{1-x}Cl_6$ (x = 0.9 and 0.1) NCs devices was measured at room temperature under different magnet field directions of the permanent magnet. The excitation light is 340 LDE with an intensity of 86 mW/cm^2.

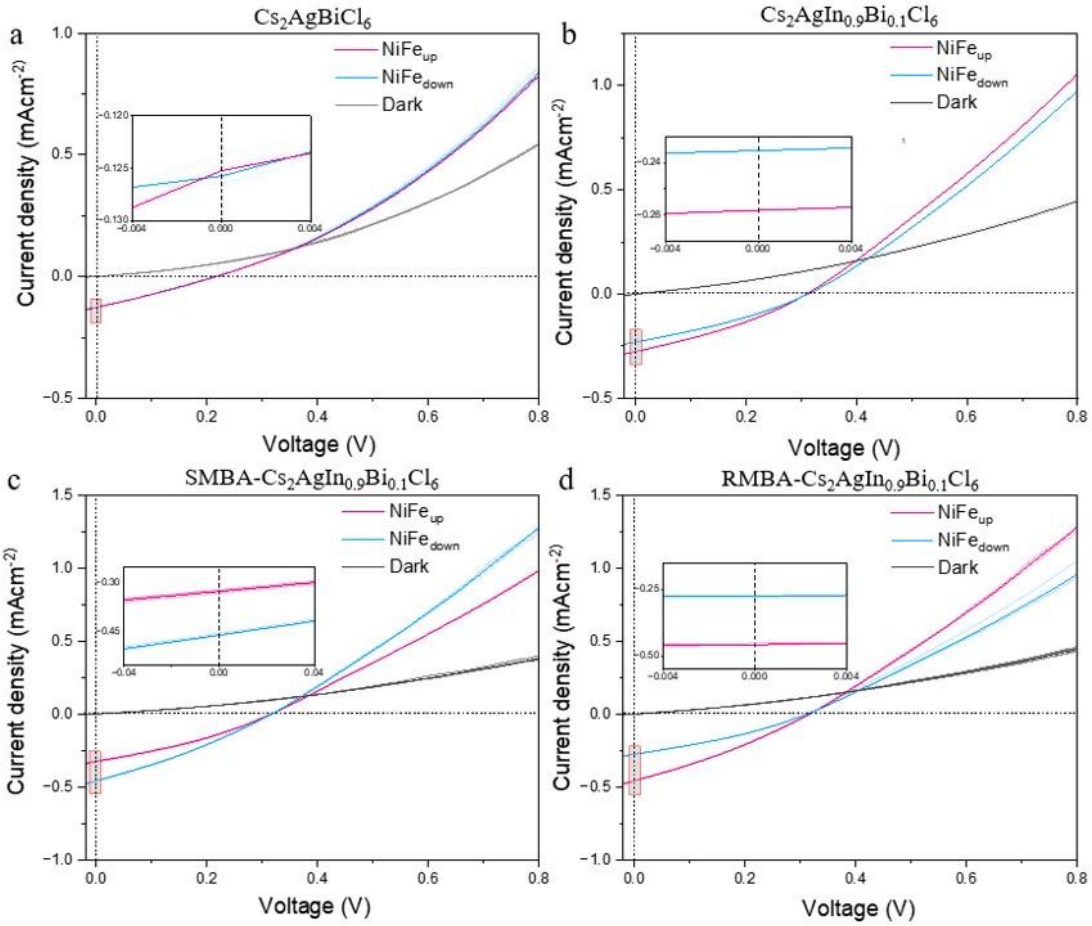

Figure 5. 14 Photovoltaic response of (a) $Cs_2AgBiCl_6$ NCs, (b) $Cs_2AgIn_{0.9}Bi_{0.1}Cl_6$ NCs, (c) RMBA-treated $Cs_2AgIn_{0.9}Bi_{0.1}Cl_6$ NCs and (d) SMBA-treated $Cs_2AgIn_{0.9}Bi_{0.1}Cl_6$ NCs device under a different direction out-of-plane magnet field. The inset is a magnified view of the data around V = 0 V.

First is the J-V response of the $Cs_2AgBiCl_6$ NCs and $Cs_2AgIn_{0.9}Bi_{0.1}Cl_6$ NCs device under 340 nm LED without chiral ligand exchange. In Figure 5.13a, the $Cs_2AgBiCl_6$ NCs devices have no obvious difference in photocurrent at 0V (short-circuit current, J_{sc}) under the opposite magnet direction. By contrast, the corresponding $Cs_2AgIn_{0.9}Bi_{0.1}Cl_6$ NCs devices show an eye-catching difference when excited using 340 nm LED, which is magnetized in the south and north direction, respectively (Figure 5.13b). We also note that the J_{sc} of the SMBA-treated and RMBA-treated $Cs_2AgIn_{0.9}Bi_{0.1}Cl_6$ NCs device also show an outstanding difference, which is magnetized by a permanent magnet with the direction of the north and south (Figure 5.13c and d). To quantify the difference of J_{sc} in the photovoltaic devices under an opposite direction of an out-of-plane magnet field, we define a spin-polarized photocurrent, P_{Jsc},

$$P_{Jsc} = \frac{I_{up} - I_{down}}{I_{up} + I_{down}} \times 100\% \qquad \text{Equation 5.3}$$

Where I_{up} and I_{down} are the average spin-polarizaed photocurrent at 0 V, which is measured under a 340 nm LED with an intensity of 10 mW/cm^2 at room temperature. Our spin-polarised J_{sc} gives a high degree in $Cs_2AgIn_{0.9}Bi_{0.1}Cl_6$ NCs and SMBA-/RMBA-treated $Cs_2AgIn_{0.9}Bi_{0.1}Cl_6$ NCs device. The value of the P_{Jsc} is 10% in untreated $Cs_2AgIn_{0.9}Bi_{0.1}Cl_6$ NCs device (Figure 5.13b). After the treatment of chiral ligands (RMBA/SMBA) in $Cs_2AgIn_{0.9}Bi_{0.1}Cl_6$ NCs, the photovoltaic device achieved an exceptional value of P_{Jsc}, +25% and −17%, respectively (Figure 5.13c and d). The degree of the spin-photocurrent shows a similar phenomenon with the measurement of the I-V curves of the CISS device, which shows that the CISS effect also influenced the photocurrent of the photovoltaic device under the opposite magnetization of the $Ni_{80}Fe_{20}$ permanent magnet electrode.

5.3 Conclusion

In summary, our research has yielded several significant findings. Firstly, we successfully synthesized cubic phase $Cs_2AgIn_xBi_{1-x}Cl_6$ (x = 0, 0.3, 0.6, and 0.9) NCs with regular morphology and uniform size. Secondly, we discovered the intrinsic chirality of $Cs_2AgIn_{0.9}Bi_{0.1}Cl_6$ NCs while studying the chiral signals induced by chiral ligand exchange. Furthermore, we confirmed the intrinsic chirality of $Cs_2AgIn_{0.9}Bi_{0.1}Cl_6$ NCs by atomic structure in HADDF-STEM imaging and simulation which arises from chiral defects, more specifically, screw dislocation. Both $Cs_2AgI_{0.9}Bi_{0.1}Cl_6$ NCs and the R/SMBA-$Cs_2AgI_{0.9}Bi_{0.1}Cl_6$ NCs exhibited remarkably long spin depolarization lifetime, spanning 10 ns. Additionally, we estimated the degree of spin-polarized current to be +50% for RMBA-treated and −47% for SMBA-treated $Cs_2AgIn_{0.9}Bi_{0.1}Cl_6$ NCs in CISS devices. And the untreated $Cs_2AgI_{0.9}Bi_{0.1}Cl_6$ NCs also showed a spin polarization value of P_{spin} +30%. Importantly, we provided further proof of the CISS effect using measurements of spin photocurrent characterization in $Cs_2AgIn_{0.9}Bi_{0.1}Cl_6$ NCs and SMBA-/RMBA-treated $Cs_2AgIn_{0.9}Bi_{0.1}Cl_6$ NCs device. These findings enhance our understanding of the chiral properties and mechanisms of lead-free double perovskite nanocrystals and have important implications for the design and development of optoelectronic devices based on these materials.

Chapter 6 Conclusion and Future Plan

6.1 Conclusions

This dissertation presents the synthesis of the $CsPbBr_3$ nanoplates (NPLs) and $Cs_2AgIn_xBi_{1-x}Cl_6$ (x = 0, 0.3, 0.6 and 0.9) nanocrystals (NCs). We employed the post-ligand exchange to induce the chirality in these perovskite $CsPbBr_3$ NPLs and $Cs_2AgIn_xBi_{1-x}Cl_6$ (x = 0, 0.3, 0.6 and 0.9) NCs. Achieving long-lived spin orientation at room temperature in the absence of a magnetic field is challenging. To address this, we investigated the spin generation, dynamics, and transport properties of newly developed colloidal chiral $CsPbBr_3$ perovskite NPLs with varying wall thicknesses. Additionally, to tackle the instability and toxicity of the lead-based perovskites are also urgent, we utilized the $Cs_2AgIn_xBi_{1-x}Cl_6$ (x = 0, 0.3, 0.6 and 0.9) lead-free double perovskite NCs.

In the first study, we examined the spin generation, dynamics, and transport properties of newly developed colloidal chiral $CsPbBr_3$ perovskite NPLs with varying layer thicknesses. These chiral NPLs exhibit an extended spin depolarization lifetime of approximately 210 ps, which is around one order of magnitude longer than their nanocrystal counterparts. Notably, they also demonstrate high circularly polarized emission (5.0%), spin current polarization up to approximately 43%, and a spin diffusion length of 33 nm. Theoretical calculations suggest that the introduction of chiral ligands induces asymmetry in $CsPbBr_3$ NPLs, creating an additional barrier to spin flipping due to the distinct momentum troughs associated with different spin states. These findings provide valuable insights into the underlying mechanisms and highlight a novel class of materials with great potential for future spintronic applications.

Next, we focused on lead-free double perovskite $Cs_2AgIn_xBi_{1-x}Cl_6$ (x = 0, 0.3, 0.6, and 0.9) NCs to solve the stability and toxicity issues of lead-based $CsPbBr_3$ NPLs. We successfully synthesized cubic phase $Cs_2AgIn_xBi_{1-x}Cl_6$ (x = 0, 0.3, 0.6, and 0.9) NCs with regular morphology and uniform size. We discovered the intrinsic chirality of $Cs_2AgIn_{0.9}Bi_{0.1}Cl_6$ NCs while studying the chiral signals induced by chiral ligand exchange. Most significantly, we confirmed that the intrinsic chirality of nanocrystals arises from chiral defects, more specifically, screw dislocations, with HADDF-STEM imaging and simulation. And then the $Cs_2AgI_{0.9}Bi_{0.1}Cl_6$ NCs and the R/SMBA-$Cs_2AgI_{0.9}Bi_{0.1}Cl_6$ NCs both show a remarkably long spin depolarization lifetime, spanning 10 ns. Additionally, we estimated the degree of spin-polarized current of +50% for RMBA-treated $Cs_2AgIn_{0.9}Bi_{0.1}Cl_6$ NCs CISS device and −47% for SMBA-treated $Cs_2AgIn_{0.9}Bi_{0.1}Cl_6$ NCs CISS device, respectively. Further proof of the CISS effect was obtained in spin photovoltaic devices with $Cs_2AgIn_{0.9}Bi_{0.1}Cl_6$ NCs and SMBA-/RMBA-treated $Cs_2AgIn_{0.9}Bi_{0.1}Cl_6$ NCs devices. These findings enhance our understanding of the chiral properties and mechanisms of lead-free double perovskite nanocrystals and have important implications for the design and development of spintronic devices based on these chiral perovskite materials.

6.2 Future Plan

As a burgeoning and promising candidate for spintronics applications, perovskite nanomaterials have been widely studied owing to their abundant optoelectrical properties combined with unique spintronic behaviours. However, several challenges remain in the spintronics of the perovskite materials, which are influenced by the drawbacks of perovskite materials (toxicity, instability, etc.), difficulties of high-quality device fabrication (e.g., low conductivity, mismatched bands, short spin lifetime, etc.) and limitations of the physics characteristics.

Despite achieving an extended spin depolarization lifetime of approximately 210 ps-significantly longer than their nanocrystal counterparts-along with a high circularly polarized emission (5.0%), spin current polarization up to approximately 43%, and a spin diffusion length reaching 33 nm in $CsPbBr_3$ nanocrystal platelets (NPLs), further optimization is needed. Strategies to enhance the degree of polarization, further explore the possibilities of the spintronics photoelectrical applications (CPL, spin-LEDs, etc.) and improve the stability of $CsPbBr_3$ nanocrystal NPLs are essential.

To address lead-based perovskite nanomaterials' stability and toxicity issues, we utilized $Cs_2AgIn_xBi_{1-x}Cl_6$ (x = 0, 0.3, 0.6, and 0.9) lead-free double perovskite NCs. Both $Cs_2AgI_{0.9}Bi_{0.1}Cl_6$ NCs and the R/SMBA-$Cs_2AgI_{0.9}Bi_{0.1}Cl_6$ NCs demonstrated remarkably long spin depolarization lifetime and a clear CISS effect in dark and photocurrent measurements under opposite magnet field. However, the photovoltaic performance of the $Cs_2AgIn_xBi_{1-x}Cl_6$ NCs was limited by the conductivity of the ligands. To overcome this limitation, we attempt to synthesize perovskite nanomaterials with other conjugated or short-chain ligands that enable stronger interaction with perovskite nanomaterials. Additionally, optimizing device fabrication by achieving a high degree of polarization, passivating defects in the interface, and matching energy bands are feasible strategies to enhance performance.

Reference

(1) Ju, M. G.; Dai, J.; Ma, L.; Zeng, X. C. Perovskite chalcogenides with optimal bandgap and desired optical absorption for photovoltaic devices. *Advanced Energy Materials* **2017**, *7* (18), 1700216.

(2) Noman, M.; Sherwani, T.; Jan, S. T.; Ismail, M. Exploring the impact of kesterite charge transport layers on the photovoltaic properties of $MAPbI_3$ perovskite solar cells. *Physica Scripta* **2023**, *98* (12), 125507.

(3) Huang, L.-y.; Lambrecht, W. R. Electronic band structure, phonons, and exciton binding energies of halide perovskites $CsSnCl_3$, $CsSnBr_3$, and $CsSnI_3$. *Physical Review B—Condensed Matter and Materials Physics* **2013**, *88* (16), 165203. Li, P.; Liang, C.; Liu, X. L.; Li, F.; Zhang, Y.; Liu, X. T.; Gu, H.; Hu, X.; Xing, G.; Tao, X. Low-dimensional perovskites with diammonium and monoammonium alternant cations for high-performance photovoltaics. *Advanced Materials* **2019**, *31* (35), 1901966.

(4) Yang, Z.; Surrente, A.; Galkowski, K.; Bruyant, N.; Maude, D. K.; Haghighirad, A. A.; Snaith, H. J.; Plochocka, P.; Nicholas, R. J. Unraveling the exciton binding energy and the dielectric constant in single-crystal methylammonium lead triiodide perovskite. *The journal of physical chemistry letters* **2017**, *8* (8), 1851-1855.

(5) Li, Y.; Yan, W.; Li, Y.; Wang, S.; Wang, W.; Bian, Z.; Xiao, L.; Gong, Q. Direct observation of long electron-hole diffusion distance in $CH_3NH_3PbI_3$ perovskite thin film. *Scientific Reports* **2015**, *5* (1), 14485.

(6) Ran, C.; Xu, J.; Gao, W.; Huang, C.; Dou, S. Defects in metal triiodide perovskite materials towards high-performance solar cells: origin, impact, characterization, and engineering. *Chemical Society Reviews* **2018**, *47* (12), 4581-4610.

(7) Cavalcante, L.; Marques, V.; Sczancoski, J.; Escote, M.; Joya, M.; Varela, J. A.; Santos, M.; Pizani, P.; Longo, E. Synthesis, structural refinement and optical behavior

of $CaTiO_3$ powders: A comparative study of processing in different furnaces. *Chemical Engineering Journal* **2008**, *143* (1-3), 299-307.

(8) Anaya, M.; Lozano, G.; Calvo, M. E.; Míguez, H. ABX_3 perovskites for tandem solar cells. *Joule* **2017**, *1* (4), 769-793.

(9) Fan, Z.; Sun, K.; Wang, J. Perovskites for photovoltaics: a combined review of organic-inorganic halide perovskites and ferroelectric oxide perovskites. *Journal of Materials Chemistry A* **2015**, *3* (37), 18809-18828.

(10) Steele, J. A.; Jin, H.; Dovgaliuk, I.; Berger, R. F.; Braeckevelt, T.; Yuan, H.; Martin, C.; Solano, E.; Lejaeghere, K.; Rogge, S. M. Thermal unequilibrium of strained black $CsPbI_3$ thin films. *Science* **2019**, *365* (6454), 679-684.

(11) Ha, S.-T.; Su, R.; Xing, J.; Zhang, Q.; Xiong, Q. Metal halide perovskite nanomaterials: synthesis and applications. *Chemical Science* **2017**, *8* (4), 2522-2536.

(12) Kim, Y.-H.; Kim, S.; Kakekhani, A.; Park, J.; Park, J.; Lee, Y.-H.; Xu, H.; Nagane, S.; Wexler, R. B.; Kim, D.-H. Comprehensive defect suppression in perovskite nanocrystals for high-efficiency light-emitting diodes. *Nature Photonics* **2021**, *15* (2), 148-155.

(13) Berestennikov, A.; Li, Y.; Iorsh, I.; Zakhidov, A. A.; Rogach, A.; Makarov, S. Beyond quantum confinement: excitonic nonlocality in halide perovskite nanoparticles with Mie resonances. *Nanoscale* **2019**, *11* (14), 6747-6754.

(14) Baranov, D.; Toso, S.; Imran, M.; Manna, L. Investigation into the photoluminescence red shift in cesium lead bromide nanocrystal superlattices. *The journal of physical chemistry letters* **2019**, *10* (3), 655-660.

(15) Sichert, J. A.; Tong, Y.; Mutz, N.; Vollmer, M.; Fischer, S.; Milowska, K. Z.; García Cortadella, R.; Nickel, B.; Cardenas-Daw, C.; Stolarczyk, J. K. Quantum size effect in organometal halide perovskite nanoplatelets. *Nano Letters* **2015**, *15* (10), 6521-6527.

(16) Kostopoulou, A.; Brintakis, K.; Nasikas, N. K.; Stratakis, E. Perovskite

nanocrystals for energy conversion and storage. *Nanophotonics* **2019**, *8* (10), 1607-1640.

(17) Chen, Z.; Gu, Z.-G.; Fu, W.-Q.; Wang, F.; Zhang, J. A confined fabrication of perovskite quantum dots in oriented MOF thin film. *ACS applied materials & interfaces* **2016**, *8* (42), 28737-28742.

(18) Ashley, M. J.; O'Brien, M. N.; Hedderick, K. R.; Mason, J. A.; Ross, M. B.; Mirkin, C. A. Templated synthesis of uniform perovskite nanowire arrays. *Journal of the American Chemical Society* **2016**, *138* (32), 10096-10099.

(19) Protesescu, L.; Yakunin, S.; Bodnarchuk, M. I.; Krieg, F.; Caputo, R.; Hendon, C. H.; Yang, R. X.; Walsh, A.; Kovalenko, M. V. Nanocrystals of cesium lead halide perovskites ($CsPbX_3$, X= Cl, Br, and I): novel optoelectronic materials showing bright emission with wide color gamut. *Nano Letters* **2015**, *15* (6), 3692-3696.

(20) Wang, A.; Guo, Y.; Muhammad, F.; Deng, Z. Controlled synthesis of lead-free cesium tin halide perovskite cubic nanocages with high stability. *Chemistry of Materials* **2017**, *29* (15), 6493-6501.

(21) Zhang, F.; Zhong, H.; Chen, C.; Wu, X.-g.; Hu, X.; Huang, H.; Han, J.; Zou, B.; Dong, Y. Brightly luminescent and color-tunable colloidal $CH_3NH_3PbX_3$ (X= Br, I, Cl) quantum dots: potential alternatives for display technology. *ACS nano* **2015**, *9* (4), 4533-4542.

(22) Bohn, B. J.; Tong, Y.; Gramlich, M.; Lai, M. L.; Döblinger, M.; Wang, K.; Hoye, R. L.; Müller-Buschbaum, P.; Stranks, S. D.; Urban, A. S. Boosting tunable blue luminescence of halide perovskite nanoplatelets through postsynthetic surface trap repair. *Nano Letters* **2018**, *18* (8), 5231-5238.

(23) Jang, D. M.; Kim, D. H.; Park, K.; Park, J.; Lee, J. W.; Song, J. K. Ultrasound synthesis of lead halide perovskite nanocrystals. *Journal of Materials Chemistry C* **2016**, *4* (45), 10625-10629.

(24) Zhang, A.; Lv, Q. Organic-Inorganic Hybrid Perovskite Nanomaterials: Synthesis and Application. *ChemistrySelect* **2020**, *5* (41), 12641-12659.

(25) Cao, M.; Xu, Y.; Li, P.; Zhong, Q.; Yang, D.; Zhang, Q. Recent advances and perspectives on light emitting diodes fabricated from halide metal perovskite nanocrystals. *Journal of Materials Chemistry C* **2019**, *7* (46), 14412-14440.

(26) Zeng, Z.; Xu, Y.; Zhang, Z.; Gao, Z.; Luo, M.; Yin, Z.; Zhang, C.; Xu, J.; Huang, B.; Luo, F. Rare-earth-containing perovskite nanomaterials: design, synthesis, properties and applications. *Chemical Society Reviews* **2020**, *49* (4), 1109-1143.

(27) Akkerman, Q. A.; Gandini, M.; Di Stasio, F.; Rastogi, P.; Palazon, F.; Bertoni, G.; Ball, J. M.; Prato, M.; Petrozza, A.; Manna, L. Strongly emissive perovskite nanocrystal inks for high-voltage solar cells. *Nature Energy* **2016**, *2* (2), 1-7.

(28) Sahli, F.; Kamino, B. A.; Werner, J.; Bräuninger, M.; Paviet-Salomon, B.; Barraud, L.; Monnard, R.; Seif, J. P.; Tomasi, A.; Jeangros, Q. Improved optics in monolithic perovskite/silicon tandem solar cells with a nanocrystalline silicon recombination junction. *Advanced Energy Materials* **2018**, *8* (6), 1701609.

(29) Liang, T.; Liu, W.; Liu, X.; Li, Y.; Fan, J. Fabry–Perot Mode-Limited High-Purcell-Enhanced Spontaneous Emission from In Situ Laser-Induced $CsPbBr_3$ Quantum Dots in CsPb2Br5 Microcavities. *Nano Letters* **2021**, *22* (1), 355-365.

(30) Wang, K.; Du, Y.; Liang, J.; Zhao, J.; Xu, F. F.; Liu, X.; Zhang, C.; Yan, Y.; Zhao, Y. S. Wettability-guided screen printing of perovskite microlaser arrays for current-driven displays. *Advanced Materials* **2020**, *32* (29), 2001999.

(31) Ramasamy, P.; Lim, D.-H.; Kim, B.; Lee, S.-H.; Lee, M.-S.; Lee, J.-S. All-inorganic cesium lead halide perovskite nanocrystals for photodetector applications. *Chemical Communications* **2016**, *52* (10), 2067-2070.

(32) Gong, M.; Sakidja, R.; Goul, R.; Ewing, D.; Casper, M.; Stramel, A.; Elliot, A.; Wu, J. Z. High-performance all-inorganic $CsPbCl_3$ perovskite nanocrystal

photodetectors with superior stability. *ACS nano* **2019**, *13* (2), 1772-1783.

(33) Zheng, W.; Lin, R.; Zhang, Z.; Liao, Q.; Liu, J.; Huang, F. An ultrafast-temporally-responsive flexible photodetector with high sensitivity based on high-crystallinity organic-inorganic perovskite nanoflake. *Nanoscale* **2017**, *9* (34), 12718-12726.

(34) Dang, Y.; Liu, X.; Cao, B.; Tao, X. Chiral halide perovskite crystals for optoelectronic applications. *Matter* **2021**, *4* (3), 794-820.

(35) Billing, D. G.; Lemmerer, A. Synthesis and crystal structures of inorganic-organic hybrids incorporating an aromatic amine with a chiral functional group. *CrystEngComm* **2006**, *8* (9), 686-695.

(36) del Villar-Guerra, R.; Gray, R. D.; Chaires, J. B. Quadruplex DNA structure characterization by circular dichroism. *Current protocols in nucleic acid chemistry* **2017**, *68*, 17.18. 11.

(37) Tanaka, H.; Inoue, Y.; Mori, T. Circularly polarized luminescence and circular dichroisms in small organic molecules: correlation between excitation and emission dissymmetry factors. *ChemPhotoChem* **2018**, *2* (5), 386-402.

(38) Ma, S.; Ahn, J.; Moon, J. Chiral perovskites for next-generation photonics: from chirality transfer to chiroptical activity. *Advanced Materials* **2021**, *33* (47), 2005760.

(39) Ma, J.; Wang, H.; Li, D. Recent progress of chiral perovskites: materials, synthesis, and properties. *Advanced Materials* **2021**, *33* (26), 2008785.

(40) Ahn, J.; Lee, E.; Tan, J.; Yang, W.; Kim, B.; Moon, J. A new class of chiral semiconductors: chiral-organic-molecule-incorporating organic-inorganic hybrid perovskites. *Materials Horizons* **2017**, *4* (5), 851-856.

(41) Ren, H.; Wu, Y.; Wang, C.; Yan, Y. 2D perovskite nanosheets with intrinsic chirality. *The Journal of Physical Chemistry Letters* **2021**, *12* (10), 2676-2681.

(42) Kang, W.; Gao, X.; Li, H.; Wei, Y.; Wang, C.; Tian, Z. Hierarchical Chiral Self-Assembly of Lead Halide Perovskite Nanocrystals by Oriented Phase Transition.

Advanced Functional Materials **2023**, *33* (30), 2300388.

(43) Long, G.; Sabatini, R.; Saidaminov, M. I.; Lakhwani, G.; Rasmita, A.; Liu, X.; Sargent, E. H.; Gao, W. Chiral-perovskite optoelectronics. *Nature Reviews Materials* **2020**, *5* (6), 423-439.

(44) He, T.; Li, J.; Li, X.; Ren, C.; Luo, Y.; Zhao, F.; Chen, R.; Lin, X.; Zhang, J. Spectroscopic studies of chiral perovskite nanocrystals. *Applied Physics Letters* **2017**, *111* (15).

(45) Jiang, S.; Song, Y.; Kang, H.; Li, B.; Yang, K.; Xing, G.; Yu, Y.; Li, S.; Zhao, P.; Zhang, T. Ligand exchange strategy to achieve chiral perovskite nanocrystals with a high photoluminescence quantum yield and regulation of the chiroptical property. *ACS Applied Materials & Interfaces* **2021**, *14* (2), 3385-3394.

(46) Chen, W.; Zhang, S.; Zhou, M.; Zhao, T.; Qin, X.; Liu, X.; Liu, M.; Duan, P. Two-photon absorption-based upconverted circularly polarized luminescence generated in chiral perovskite nanocrystals. *The journal of physical chemistry letters* **2019**, *10* (12), 3290-3295.

(47) Georgieva, Z. N.; Bloom, B. P.; Ghosh, S.; Waldeck, D. H. Imprinting chirality onto the electronic states of colloidal perovskite nanoplatelets. *Advanced Materials* **2018**, *30* (23), 1800097.

(48) Shi, Y.; Duan, P.; Huo, S.; Li, Y.; Liu, M. Endowing perovskite nanocrystals with circularly polarized luminescence. *Advanced Materials* **2018**, *30* (12), 1705011.

(49) Zhao, B.; Gao, X.; Pan, K.; Deng, J. Chiral helical polymer/perovskite hybrid nanofibers with intense circularly polarized luminescence. *ACS nano* **2021**, *15* (4), 7463-7471.

(50) Liu, S.; Liu, X.; Wu, Y.; Zhang, D.; Wu, Y.; Tian, H.; Zheng, Z.; Zhu, W.-H. Circularly polarized perovskite luminescence with dissymmetry factor up to 1.9 by soft helix bilayer device. *Matter* **2022**, *5* (7), 2319-2333.

(51) Ru, Y.; Zhang, B.; Yong, X.; Sui, L.; Yu, J.; Song, H.; Lu, S. Full-color circularly polarized luminescence of CsPbX3 nanocrystals triggered by chiral carbon dots. *Advanced Materials* **2023**, *35* (5), 2207265.

(52) Schulz, M.; Balzer, F.; Scheunemann, D.; Arteaga, O.; Lützen, A.; Meskers, S. C.; Schiek, M. Chiral excitonic organic photodiodes for direct detection of circular polarized light. *Advanced Functional Materials* **2019**, *29* (16), 1900684.

(53) Wang, L.; Xue, Y.; Cui, M.; Huang, Y.; Xu, H.; Qin, C.; Yang, J.; Dai, H.; Yuan, M. A chiral reduced-dimension perovskite for an efficient flexible circularly polarized light photodetector. *Angewandte Chemie* **2020**, *132* (16), 6504-6512.

(54) Kim, Y.-H.; Zhai, Y.; Lu, H.; Pan, X.; Xiao, C.; Gaulding, E. A.; Harvey, S. P.; Berry, J. J.; Vardeny, Z. V.; Luther, J. M. Chiral-induced spin selectivity enables a room-temperature spin light-emitting diode. *Science* **2021**, *371* (6534), 1129-1133.

(55) Ye, C.; Jiang, J.; Zou, S.; Mi, W.; Xiao, Y. Core-Shell Three-Dimensional Perovskite Nanocrystals with Chiral-Induced Spin Selectivity for Room-Temperature Spin Light-Emitting Diodes. *Journal of the American Chemical Society* **2022**, *144* (22), 9707-9714.

(56) Wei, Q.; Ning, Z. Chiral perovskite spin-optoelectronics and spintronics: toward judicious design and application. *ACS Materials Letters* **2021**, *3* (9), 1266-1275.

(57) Lu, H.; Wang, J.; Xiao, C.; Pan, X.; Chen, X.; Brunecky, R.; Berry, J. J.; Zhu, K.; Beard, M. C.; Vardeny, Z. V. Spin-dependent charge transport through 2D chiral hybrid lead-iodide perovskites. *Science Advances* **2019**, *5* (12), eaay0571.

(58) Wang, J.; Lu, H.; Pan, X.; Xu, J.; Liu, H.; Liu, X.; Khanal, D. R.; Toney, M. F.; Beard, M. C.; Vardeny, Z. V. Spin-dependent photovoltaic and photogalvanic responses of optoelectronic devices based on chiral two-dimensional hybrid organic-inorganic perovskites. *ACS nano* **2020**, *15* (1), 588-595.

(59) Yang, S.-H.; Naaman, R.; Paltiel, Y.; Parkin, S. S. Chiral spintronics. *Nature*

Reviews Physics **2021**, *3* (5), 328-343.

(60) Hirohata, A.; Takanashi, K. Future perspectives for spintronic devices. *Journal of Physics D: Applied Physics* **2014**, *47* (19), 193001.

(61) Lu, Y.; Wang, Q.; Han, L.; Zhao, Y.; He, Z.; Song, W.; Song, C.; Miao, Z. Spintronic Phenomena and Applications in Hybrid Organic-Inorganic Perovskites. *Advanced Functional Materials* **2024**, 2314427.

(62) Niesner, D.; Wilhelm, M.; Levchuk, I.; Osvet, A.; Shrestha, S.; Batentschuk, M.; Brabec, C.; Fauster, T. Giant Rashba splitting in $CH_3NH_3PbBr_3$ organic-inorganic perovskite. *Physical Review Letters* **2016**, *117* (12), 126401.

(63) Park, I.-H.; Zhang, Q.; Kwon, K. C.; Zhu, Z.; Yu, W.; Leng, K.; Giovanni, D.; Choi, H. S.; Abdelwahab, I.; Xu, Q.-H. Ferroelectricity and Rashba effect in a two-dimensional Dion-Jacobson hybrid organic-inorganic perovskite. *Journal of the American Chemical Society* **2019**, *141* (40), 15972-15976.

(64) Xie, Z.; Markus, T. Z.; Cohen, S. R.; Vager, Z.; Gutierrez, R.; Naaman, R. Spin specific electron conduction through DNA oligomers. *Nano letters* **2011**, *11* (11), 4652-4655.

(65) Huang, Z.; Bloom, B. P.; Ni, X.; Georgieva, Z. N.; Marciesky, M.; Vetter, E.; Liu, F.; Waldeck, D. H.; Sun, D. Magneto-optical detection of photoinduced magnetism via chirality-induced spin selectivity in 2D chiral hybrid organic-inorganic perovskites. *ACS nano* **2020**, *14* (8), 10370-10375.

(66) Wang, Q.; Zhu, H.; Tan, Y.; Hao, J.; Ye, T.; Tang, H.; Wang, Z.; Ma, J.; Sun, J.; Zhang, T. Spin Quantum Dot Light-Emitting Diodes Enabled by 2D Chiral Perovskite with Spin-Dependent Carrier Transport. *Advanced Materials* **2024**, *36* (5), 2305604.

(67) Hao, J.; Lu, H.; Mao, L.; Chen, X.; Beard, M. C.; Blackburn, J. L. Direct detection of circularly polarized light using chiral copper chloride-carbon nanotube heterostructures. *ACS nano* **2021**, *15* (4), 7608-7617.

(68) Giovanni, D.; Ma, H.; Chua, J.; Grätzel, M.; Ramesh, R.; Mhaisalkar, S.; Mathews, N.; Sum, T. C. Highly spin-polarized carrier dynamics and ultralarge photoinduced magnetization in $CH_3NH_3PbI_3$ perovskite thin films. *Nano Letters* **2015**, *15* (3), 1553-1558.

(69) Wang, M.; Zou, H.; Zhang, J.; Wu, T.; Xu, H.; Haacke, S.; Hu, B. Extremely long spin lifetime of light-emitting states in quasi-2D perovskites through orbit–orbit interaction. *The journal of physical chemistry letters* **2020**, *11* (9), 3647-3652.

(70) Zhang, Y.; Zhang, B.; Wang, J.; Fu, Y.; Han, Y.; Guo, J.; Zhang, X. Spin Preserved Exciton Funneling through a Polaronic Intermediate State in Layered Perovskite Single Crystals. *Advanced Optical Materials* **2023**, *11* (6), 2202444.

(71) Yao, J.; Wang, Z.; Huang, Y.; Xue, J.; Zhang, D.; Chen, J.; Chen, X.; Dong, S.-C.; Lu, H. Efficient Green Spin Light-Emitting Diodes Enabled by Ultrafast Energy-and Spin-Funneling in Chiral Perovskites. *Journal of the American Chemical Society* **2024**.

(72) Lyu, M.; Yun, J. H.; Chen, P.; Hao, M.; Wang, L. Addressing toxicity of lead: progress and applications of low-toxic metal halide perovskites and their derivatives. *Advanced Energy Materials* **2017**, *7* (15), 1602512.

(73) Zhao, L.; Han, X.; Zheng, Y.; Yu, M.-H.; Xu, J. Tin-based chiral perovskites with second-order nonlinear optical properties. *Advanced Photonics Research* **2021**, *2* (11), 2100056.

(74) Rajput, P. K.; Poonia, A. K.; Mukherjee, S.; Sheikh, T.; Shrivastava, M.; Adarsh, K.; Nag, A. Chiral methylbenzylammonium bismuth iodide with zero-dimensional perovskite derivative structure. *The Journal of Physical Chemistry C* **2022**, *126* (23), 9889-9897.

(75) Sun, B.; Liu, X.-F.; Li, X.-Y.; Zhang, Y.; Shao, X.; Yang, D.; Zhang, H.-L. Two-dimensional perovskite chiral ferromagnets. *Chemistry of Materials* **2020**, *32* (20), 8914-8920.

(76) Dehnhardt, N.; Axt, M.; Zimmermann, J.; Yang, M.; Mette, G.; Heine, J. Band gap-tunable, chiral hybrid metal halides displaying second-harmonic generation. *Chemistry of Materials* **2020**, *32* (11), 4801-4807.

(77) Yang, C.-H.; Xiao, S.-B.; Xiao, H.; Xu, L.-J.; Chen, Z.-N. Efficient red-emissive circularly polarized electroluminescence enabled by quasi-2D perovskite with chiral spacer cation. *ACS nano* **2023**, *17* (8), 7830-7836.

(78) Wang, C.; Li, G.; Dai, Z.; Tian, W.; Li, L. Patterned Chiral Perovskite Film for Self-Driven Stokes Photodetectors. *Advanced Functional Materials* **2024**, 2316265.

(79) Tao, L.; Tang, W.; Yan, M.; Ding, L.; Wei, J.; Wang, L.; Li, L.; Li, L.; Yang, D.; Fang, Y. Construction of chiral-2D/3D perovskite heterojunction films for efficient circularly polarized light detection. *Journal of Materials Chemistry C* **2023**, *11* (36), 12392-12399.

(80) Ren, L.; Zhai, P.; Wang, S.; Tian, Y.; Jin, K.; Liu, S. F. First observation of magnon transport in organic-inorganic hybrid perovskite. *Matter* **2022**, *5* (10), 3391-3401.

(81) Sugawara, T.; Matsushita, M. M. Spintronics in organic π-electronic systems. *Journal of Materials Chemistry* **2009**, *19* (12), 1738-1753.

(82) Malajovich, I.; Berry, J.; Samarth, N.; Awschalom, D. Persistent sourcing of coherent spins for multifunctional semiconductor spintronics. *Nature* **2001**, *411* (6839), 770-772. Jansen, R. Silicon spintronics. *Nature Materials* **2012**, *11* (5), 400-408. Rocha, A. R.; Garcia-Suarez, V. M.; Bailey, S. W.; Lambert, C. J.; Ferrer, J.; Sanvito, S. Towards molecular spintronics. *Nature Materials* **2005**, *4* (4), 335-339.

(83) Žutić, I.; Fabian, J.; Sarma, S. D. Spintronics: Fundamentals and applications. *Reviews of modern physics* **2004**, *76* (2), 323.

(84) Li, Y.; Luo, X.; Liu, Y.; Lu, X.; Wu, K. Size-and composition-dependent exciton spin relaxation in lead halide perovskite quantum dots. *ACS Energy Lett.* **2020**, *5* (5), 1701-1708.

(85) Chen, X.; Lu, H.; Wang, K.; Zhai, Y.; Lunin, V.; Sercel, P. C.; Beard, M. C. Tuning spin-polarized lifetime in two-dimensional metal-halide perovskite through exciton binding energy. *J. Am. Chem. Soc.* **2021**, *143* (46), 19438-19445.

(86) Zhou, M.; Sarmiento, J. S.; Fei, C.; Zhang, X.; Wang, H. Effect of composition on the spin relaxation of lead halide perovskites. *J. Phys. Chem. Lett.* **2020**, *11* (4), 1502-1507.

(87) Odenthal, P.; Talmadge, W.; Gundlach, N.; Wang, R.; Zhang, C.; Sun, D.; Yu, Z.-G.; Valy Vardeny, Z.; Li, Y. S. Spin-polarized exciton quantum beating in hybrid organic-inorganic perovskites. *Nat. Phys.* **2017**, *13* (9), 894-899.

(88) Chen, X.; Lu, H.; Li, Z.; Zhai, Y.; Ndione, P. F.; Berry, J. J.; Zhu, K.; Yang, Y.; Beard, M. C. Impact of layer thickness on the charge carrier and spin coherence lifetime in two-dimensional layered perovskite single crystals. *ACS Energy Lett.* **2018**, *3* (9), 2273-2279.

(89) Xue, J.; Huang, Y.; Liu, Y.; Chen, Z.; Sung, H. H.; Williams, I. D.; Zhu, Z.; Mao, L.; Chen, X.; Lu, H. Rashba Band Splitting and Bulk Photovoltaic Effect Induced by Halogen Bonds in Hybrid Layered Perovskites. *Angewandte Chemie*, e202304486.

(90) Döhrmann, S.; Hägele, D.; Rudolph, J.; Bichler, M.; Schuh, D.; Oestreich, M. Anomalous spin dephasing in (110) GaAs quantum wells: Anisotropy and intersubband effects. *Phys. Rev. Lett.* **2004**, *93* (14), 147405. Balocchi, A.; Duong, Q.; Renucci, P.; Liu, B.; Fontaine, C.; Amand, T.; Lagarde, D.; Marie, X. Full electrical control of the electron spin relaxation in GaAs quantum wells. *Phys. Rev. Lett.* **2011**, *107* (13), 136604. Dzhioev, R.; Korenev, V.; Zakharchenya, B.; Gammon, D.; Bracker, A.; Tischler, J.; Katzer, D. Optical orientation and the Hanle effect of neutral and negatively charged excitons in GaAs/$Al_xGa_{1-x}As$ quantum wells. *Physical Review B* **2002**, *66* (15), 153409.

(91) Tackeuchi, A.; Nishikawa, Y.; Wada, O. Room-temperature electron spin dynamics in GaAs/AlGaAs quantum wells. *Appl. Phys. Lett.* **1996**, *68* (6), 797-799.

(92) Jang, G.; Jo, D. Y.; Ma, S.; Lee, J.; Son, J.; Lee, C. U.; Jeong, W.; Yang, S.; Park, J. H.; Yang, H. Core-Shell Perovskite Quantum Dots for Highly Selective Room-Temperature Spin Light-Emitting Diodes. *Adv. Mater.* **2024**, 2309335.

(93) Lu, H.; Xiao, C.; Song, R.; Li, T.; Maughan, A. E.; Levin, A.; Brunecky, R.; Berry, J. J.; Mitzi, D. B.; Blum, V. Highly distorted chiral two-dimensional tin iodide perovskites for spin polarized charge transport. *J. Am. Chem. Soc.* **2020**, *142* (30), 13030-13040.

(94) Chen, C.; Gao, L.; Gao, W.; Ge, C.; Du, X.; Li, Z.; Yang, Y.; Niu, G.; Tang, J. Circularly polarized light detection using chiral hybrid perovskite. *Nat. Commun.* **2019**, *10* (1), 1927.

(95) Lu, H.; Vardeny, Z. V.; Beard, M. C. Control of light, spin and charge with chiral metal halide semiconductors. *Nature Reviews Chemistry* **2022**, *6* (7), 470-485.

(96) Huang, P. J.; Taniguchi, K.; Shigefuji, M.; Kobayashi, T.; Matsubara, M.; Sasagawa, T.; Sato, H.; Miyasaka, H. Chirality-Dependent Circular Photogalvanic Effect in Enantiomorphic 2D Organic-Inorganic Hybrid Perovskites. *Adv. Mater.* **2021**, *33* (17), 2008611.

(97) Liu, X.; Wang, K.; Zhang, T.; Liu, H.; Ren, A.; Ren, S.; Li, P.; Zhang, C.; Yao, J.; Zhao, Y. S. Exciton Chirality Transfer Empowers Self-Triggered Spin-Polarized Amplified Spontaneous Emission from 1D-Anchoring-3D Perovskites. *Adv. Mater.* **2023**, *35* (52), 2305260.

(98) He, C.; Qiu, J.; Mu, Z.; Chen, J.; Wu, Y.; Jiang, Z.; Zhang, P.; Qin, X.; Xing, G.; Liu, X. Room temperature circularly polarized emission in perovskite nanocrystals through bichiral-molecule-induced lattice reconstruction. *Matter* **2024**, *7* (2), 475-484.

(99) Todd, S. B.; Riley, D. B.; Binai-Motlagh, A.; Clegg, C.; Ramachandran, A.; March, S. A.; Hoffman, J. M.; Hill, I. G.; Stoumpos, C. C.; Kanatzidis, M. G. Detection of Rashba spin splitting in 2D organic-inorganic perovskite via precessional carrier spin

relaxation. *APL Materials* **2019**, *7* (8). Bourelle, S. A.; Shivanna, R.; Camargo, F. V.; Ghosh, S.; Gillett, A. J.; Senanayak, S. P.; Feldmann, S.; Eyre, L.; Ashoka, A.; van de Goor, T. W. How exciton interactions control spin-depolarization in layered hybrid perovskites. *Nano Lett.* **2020**, *20* (8), 5678-5685.

(100) Wu, M.; Jiang, J.; Weng, M. Spin dynamics in semiconductors. *Physics Reports* **2010**, *493* (2-4), 61-236.

(101) Delaire, O.; Ma, J.; Marty, K.; May, A. F.; McGuire, M. A.; Du, M.-H.; Singh, D. J.; Podlesnyak, A.; Ehlers, G.; Lumsden, M. Giant anharmonic phonon scattering in PbTe. *Nature Materials* **2011**, *10* (8), 614-619.

(102) Martin, P. I.; Panuganti, S.; Portner, J. C.; Watkins, N. E.; Kanatzidis, M. G.; Talapin, D. V.; Schaller, R. D. Excitonic Spin-Coherence Lifetimes in CdSe Nanoplatelets Increase Significantly with Core/Shell Morphology. *Nano Lett.* **2023**, *23* (4), 1467-1473.

(103) Tang, B.; Wang, S.; Liu, H.; Mou, N.; Portniagin, A. S.; Chen, P.; Wu, Y.; Gao, X.; Lei, D.; Rogach, A. L. Chiral Ligand-Induced Inversion and Tuning of Excitonic Optical Activity in Intrinsically Chiral CsPbBr3 Perovskite Nanoplatelets. *Advanced Optical Materials* **2023**, 2301524.

(104) Ben-Moshe, A.; Teitelboim, A.; Oron, D.; Markovich, G. Probing the interaction of quantum dots with chiral capping molecules using circular dichroism spectroscopy. *Nano Lett.* **2016**, *16* (12), 7467-7473.

(105) Liu, S.; Heindl, M. W.; Fehn, N.; Caicedo-Dávila, S.; Eyre, L.; Kronawitter, S. M.; Zerhoch, J.; Bodnar, S.; Shcherbakov, A.; Stadlbauer, A. Optically Induced Long-Lived Chirality Memory in the Color-Tunable Chiral Lead-Free Semiconductor (R)/(S)-$CHEA_4Bi_2Br_xI_{10-x}$ (x= 0–10). *J. Am. Chem. Soc.* **2022**, *144* (31), 14079-14089.

(106) Li, J.; Guo, Z.; Qin, Y.; Liu, R.; He, Y.; Zhu, X.; Xu, F.; He, T. Rashba Effect and Spin-Dependent Excitonic Properties in Chiral Two-Dimensional/Three-Dimensional

Composite Perovskite Films. *J. Phys. Chem. Lett.* **2023**, *14* (51), 11697-11703. DOI: 10.1021/acs.jpclett.3c03247.

(107) Cadiz, F.; Notot, V.; Filipovic, J.; Paget, D.; Weber, C.; Martinelli, L.; Rowe, A.; Arscott, S. Ambipolar spin diffusion in p-type GaAs: A case where spin diffuses more than charge. *J. Appl. Phys.* **2017**, *122* (9). Yu, Z.-G. Spin-orbit coupling, spin relaxation, and spin diffusion in organic solids. *Phys. Rev. Lett.* **2011**, *106* (10), 106602.

(108) Kim, Y. H.; Song, R.; Hao, J.; Zhai, Y.; Yan, L.; Moot, T.; Palmstrom, A. F.; Brunecky, R.; You, W.; Berry, J. J. The structural origin of chiroptical properties in perovskite nanocrystals with chiral organic ligands. *Advanced Functional Materials* **2022**, *32* (25), 2200454.

(109) Ren, W.; Xu, A.; Chan, K.; Hu, X. A cation concentration gradient approach to tune the selectivity and activity of CO2 electroreduction. *Angew. Chem. Int. Ed.* **2022**, *61* (49), e202214173.

(110) Maiti, A.; Pal, A. J. Spin-Selective Charge Transport in Lead-Free Chiral Perovskites: The Key towards High-Anisotropy in Circularly-Polarized Light Detection. *Angew. Chem. Int. Ed.* **2022**, *61* (52), e202214161.

(111) Abhervé, A.; Mercier, N.; Kumar, A.; Das, T. K.; Even, J.; Katan, C.; Kepenekian, M. Chirality Versus Symmetry: Electron's Spin Selectivity in Nonpolar Chiral Lead-Bromide Perovskites. *Adv. Mater.* **2023**, 2305784.

(112) Wang, J.; Luo, S.; Lin, Y.; Chen, Y.; Deng, Y.; Li, Z.; Meng, K.; Chen, G.; Huang, T.; Xiao, S. Templated growth of oriented layered hybrid perovskites on 3D-like perovskites. *Nature Communications* **2020**, *11* (1), 582.

(113) Yang, Z.; Yu, Z.; Wei, H.; Xiao, X.; Ni, Z.; Chen, B.; Deng, Y.; Habisreutinger, S. N.; Chen, X.; Wang, K. Enhancing electron diffusion length in narrow-bandgap perovskites for efficient monolithic perovskite tandem solar cells. *Nature Communications* **2019**, *10* (1), 4498.

(114) Kim, M.; Jeong, J.; Lu, H.; Lee, T. K.; Eickemeyer, F. T.; Liu, Y.; Choi, I. W.; Choi, S. J.; Jo, Y.; Kim, H.-B. Conformal quantum dot-SnO_2 layers as electron transporters for efficient perovskite solar cells. *Science* **2022**, *375* (6578), 302-306.

(115) Mo, X.; Li, T.; Huang, F.; Li, Z.; Zhou, Y.; Lin, T.; Ouyang, Y.; Tao, X.; Pan, C. Highly-efficient all-inorganic lead-free 1D $CsCu_2I_3$ single crystal for white-light emitting diodes and UV photodetection. *Nano Energy* **2021**, *81*, 105570.

(116) Shamsi, J.; Urban, A. S.; Imran, M.; De Trizio, L.; Manna, L. Metal halide perovskite nanocrystals: synthesis, post-synthesis modifications, and their optical properties. *Chemical Reviews* **2019**, *119* (5), 3296-3348.

(117) Wu, Y.; Li, X.; Zeng, H. Highly luminescent and stable halide perovskite nanocrystals. *ACS Energy Letters* **2019**, *4* (3), 673-681.

(118) Ye, J.; Byranvand, M. M.; Martínez, C. O.; Hoye, R. L.; Saliba, M.; Polavarapu, L. Defect passivation in lead-halide perovskite nanocrystals and thin films: toward efficient LEDs and solar cells. *Angewandte Chemie* **2021**, *133* (40), 21804-21828.

(119) Huang, H.; Li, Y.; Tong, Y.; Yao, E. P.; Feil, M. W.; Richter, A. F.; Döblinger, M.; Rogach, A. L.; Feldmann, J.; Polavarapu, L. Spontaneous Crystallization of Perovskite Nanocrystals in Nonpolar Organic Solvents: A Versatile Approach for their Shape-Controlled Synthesis. *Angewandte Chemie International Edition* **2019**, *58* (46), 16558-16562.

(120) Wang, Y.; Xu, J.; Wang, Y.; Chen, H. Emerging chirality in nanoscience. *Chemical Society Reviews* **2013**, *42* (7), 2930-2962.

(121) Lee, H.; Huttunen, M. J.; Hsu, K.-J.; Partanen, M.; Zhuo, G.-Y.; Kauranen, M.; Chu, S.-W. Chiral imaging of collagen by second-harmonic generation circular dichroism. *Biomedical Optics Express* **2013**, *4* (6), 909-916.

(122) Billing, D. G.; Lemmerer, A. Bis [(S)-β-phenethylammonium] tribromoplumbate (II). *Acta Crystallographica Section E: Structure Reports Online* **2003**, *59* (6), m381-

m383.

(123) He, T.; Li, J.; Li, X.; Ren, C.; Luo, Y.; Zhao, F.; Chen, R.; Lin, X.; Zhang, J. Spectroscopic studies of chiral perovskite nanocrystals. *Applied Physics Letters* **2017**, *111* (15), 151102.

(124) Mustaqeem, M.; Chou, P. T.; Kamal, S.; Ahmad, N.; Lin, J. Y.; Lu, Y. J.; Lee, X. H.; Lin, K. H.; Lu, K. L.; Chen, Y. F. Solution-Processed and Room-Temperature Spin Light-Emitting Diode Based on Quantum Dots/Chiral Metal-Organic Framework Heterostructure. *Advanced Functional Materials* **2023**, 2213587.

(125) Schileo, G.; Grancini, G. Lead or no lead? Availability, toxicity, sustainability and environmental impact of lead-free perovskite solar cells. *Journal of Materials Chemistry C* **2021**, *9* (1), 67-76.

(126) Abate, A. Perovskite solar cells go lead free. *Joule* **2017**, *1* (4), 659-664.

(127) Dave, K.; Fang, M. H.; Bao, Z.; Fu, H. T.; Liu, R. S. Recent developments in lead-free double perovskites: structure, doping, and applications. *Chemistry–An Asian Journal* **2020**, *15* (2), 242-252.

(128) Shi, Z.; Guo, J.; Chen, Y.; Li, Q.; Pan, Y.; Zhang, H.; Xia, Y.; Huang, W. Lead-free organic-inorganic hybrid perovskites for photovoltaic applications: recent advances and perspectives. *Advanced Materials* **2017**, *29* (16), 1605005.

(129) Hoefler, S. F.; Trimmel, G.; Rath, T. Progress on lead-free metal halide perovskites for photovoltaic applications: a review. *Monatshefte für Chemie-Chemical Monthly* **2017**, *148*, 795-826.

(130) Igbari, F.; Wang, R.; Wang, Z.-K.; Ma, X.-J.; Wang, Q.; Wang, K.-L.; Zhang, Y.; Liao, L.-S.; Yang, Y. Composition stoichiometry of $Cs_2AgBiBr_6$ films for highly efficient lead-free perovskite solar cells. *Nano letters* **2019**, *19* (3), 2066-2073.

(131) Levy, S.; Khalfin, S.; Pavlopoulos, N. G.; Kauffmann, Y.; Atiya, G.; Shaek, S.; Dror, S.; Shechter, R.; Bekenstein, Y. The role silver nanoparticles plays in silver-based

double-perovskite nanocrystals. *Chemistry of Materials* **2021**, *33* (7), 2370-2377.

(132) Akkerman, Q. A.; Nguyen, T. P.; Boehme, S. C.; Montanarella, F.; Dirin, D. N.; Wechsler, P.; Beiglböck, F.; Rainò, G.; Erni, R.; Katan, C. Controlling the nucleation and growth kinetics of lead halide perovskite quantum dots. *Science* **2022**, *377* (6613), 1406-1412.

(133) Cong, M.; Yang, B.; Hong, F.; Zheng, T.; Sang, Y.; Guo, J.; Yang, S.; Han, K. Self-trapped exciton engineering for white-light emission in colloidal lead-free double perovskite nanocrystals. *Science Bulletin* **2020**, *65* (13), 1078-1084.

(134) Mukhina, M. V.; Maslov, V. G.; Baranov, A. V.; Fedorov, A. V.; Orlova, A. O.; Purcell-Milton, F.; Govan, J.; Gun'ko, Y. K. Intrinsic chirality of CdSe/ZnS quantum dots and quantum rods. *Nano Letters* **2015**, *15* (5), 2844-2851.

(135) Zheng, F.; Tan, L. Z.; Liu, S.; Rappe, A. M. Rashba spin-orbit coupling enhanced carrier lifetime in $CH_3NH_3PbI_3$. *Nano Letters* **2015**, *15* (12), 7794-7800.